MASTER

Model-based design of test-setup for impact-aware manipulation

de Wildt, R.H.G.W.

Award date:
2020

Department of Mechanical Engineering
Dynamics and Control Research Group

Model-based Design Of Test-Setup For Impact-Aware Manipulation

MSc. Thesis

R.H.G.W. de Wildt

DC2020-029

Project coaches:

Assist. Prof. Dr. Alessandro Saccon
Ir. Remon Damen

Project supervisor:

Prof. Dr. Nathan van de Wouw

Committee:

Prof. Dr. Nathan van de Wouw
Assist. Prof. Dr. Alessandro Saccon
Ir. Remon Damen
Ir. Paul J.E.M. Vrancken

Eindhoven, May 2020

Abstract

This study aims to develop a test-setup for educational purposes in the evaluation and demonstration of impact-aware robotic manipulation. The result of this dissertation is a planar Cartesian manipulator that supports demonstrations involving dexterous and dynamic tasks such as throwing, grabbing, and catching of objects. Through the development of a high-level mechanical design, the report discusses the selection and implementation of actuators, guides, structural parts, and materials. Herein, the high-level design provides a tool for a more detailed design allowing physical realization. With the use of rigid- multi-body simulations in the software package Algoryx Momentum, the report evaluates the high-level mechanical design by combining the simulations with simple control routines, to virtually demonstrate tasks involving throwing, catching, and grabbing of objects. This simulation-based evaluation proves that the setup is capable of demonstrating these tasks and provides insight into the validity of design choices. The report presents a virtually validated high-level mechanical design with suggestions for further development and improvement.

keywords: Impact-aware manipulation, test-bed, planar Cartesian manipulator, direct drive.

Contents

List of Tables

List of Figures

Acronyms

AM	Algoryx Momentum
CAD	computer aided design
DOF	degree of freedom
DS	Discovery SpaceClaim
FEM	finite element method
MBS	multi-body simulation
PMMA	Poly(methyl methacrylate)
PC	Polycarbonate
RMBS	rigid multi-body simulation

Symbols

α_n	Polynomial coefficient
β	Coefficient for panel stiffness
γ	Coefficient for restitution
τ	Torque
τ_{mot}	Motor torque
a	Acceleration
a_x	Horizontal acceleration
a_y	Vertical acceleration
$a_{x,min}$	Minimum required horizontal acceleration
$a_{y,min}$	Minimum required vertical acceleration
$a_{x,max}$	Maximum horizontal acceleration
$a_{y,max}$	Maximum vertical acceleration
B	Magnetic flux
C_{dyn}	Dynamic load rating of bearing
C_{stat}	Static load rating of bearing
$d_{f,max}$	Maximum depth of footprint
d_p	Deflection of panel
d_b	Depth of beam
d_{min}	Minimum distance

E_{kin}	Kinetic energy
E_{pot}	Potential energy
f_h	Hardness factor
f_t	Temperature factor
f_w	Load factor
F	Force
F_{avg}	Average penetration force over distance
F_{peak}	Peak impact force
F_{bn}	Force on bearing
F_A	Force applied by actuator
F_W	Friction force of bearings
F_g	Gravitational force
F_o	Force applied to object
F_c	Force applied at center of plate
F_{tip}	Force applied at center of tip
F_{ref}	Reference force
g	Gravitational acceleration
G	Gravity matrix
h	Height
$h_{w,min}$	Minimum height of workspace
$h_{f,max}$	Maximum height of footprint
h_p	Height of panel
h_{obj}	Projected object height
I	Current
J	Second moment of inertia
k_d	Stiffness of spring representing impacted structure
k_{max}	Maximum stiffness of spring representing impacted structure
k_{xx}	Stiffness in x-direction
k_{tot}	Total stiffness in x-direction

l	Length
l_b	Length of bracket
L_u	Minimal lifetime expectancy
$L_{l,b}$	Load-based lifetime expectancy, ball bearings
$L_{l,r}$	Load-based lifetime expectancy, roller bearings
m_i	Mass of impacting object
m_x	Moving mass of x-stage
m_y	Moving mass of y-stage
m_o	Mass of object
m_l	Mass of segment
m_j	Mass of joint
M	Mass matrix
n	Degree of polynomial
p	Position
p_x	Horizontal position
p_y	Vertical position
p_o	Position of object
p_{ee}	Position of end-effector
P	Polynomial
R	Max deviation percentage
s	Panel thickness
t	Time
t_a	Constant acceleration time
t_c	Constant velocity time
t_f	Falling time
T	Impact-time
v	Velocity
v_x	Horizontal velocity

v_y	Vertical velocity
v_i	Pre-impact velocity
v_o	Post-impact velocity
v_{ref}	Reference velocity
$v_{z,o}$	Object vertical velocity
$v_{ee,max}$	Maximum end-effector velocity
v_j	Velocity prediction
v_{meas}	Measured velocity
$v_{x,corr}$	Correction velocity
V	Centrifugal and Coriolis matrix

w	Width
$w_{w,min}$	Minimum width of workspace
$w_{f,max}$	Maximum width of footprint
w_p	Width of panel
w_b	Width of beam

x_d	Impact penetration depth

Y	Young's modulus

z	Time-step

Chapter 1

Introduction

1.1 Background and motivation

Robotic systems are used for a variety of purposes. One of these purposes is logistics, which is defined as the process of managing resource acquisition, storage, and transport. Using the robots to automate the processes involved with logistics [1]. Examples of logistic processes include freight transport, product packaging, and goods sorting.

The use of robotics in logistics process automation has the potential to improve aspects that involve product throughput, product load capacity, process safety, and process quality. Performance criteria for such robots include footprint usage and product throughput [2]. The footprint should be as small as possible, defined as the area used by a robot that can not be used by other applications. The product throughput should be as high as possible, defined as the number of products handled by one device per time unit.

Conventionally, robots displace goods by picking and placing the goods in a smoothly controlled way [3]. Picking objects with the use of position control, by moving the end-effector over the target, and closing the gripper at a predefined velocity and maximum force. The absence of an exact model of the robot and its surroundings causes collisions, and thus impacts, during object manipulation. The effects of such collisions range from elastic to plastic deformation of the robot or object, combined with short vibrations. In practice, these effects are coped with by either neglecting them or by using negligible velocities to minimize the effects [4].

Although this method is efficient in enabling a repetitive procedure to be predictably automated for any object, not all cases require this approach. In the case of lightweight, non-fragile objects, (e.g., packaged items and postal packages), where the moving mass of the robot is considerably higher than the mass of the object, the approach could be considered conservative. In such scenarios, the constant process of accelerating and decelerating to reduce velocity jumps at contact, consumes a significant part of the task execution time, while it may not be necessary, considering robots performing dexterous manipulation of objects with impacts [5][6].

1.2 State-of-the-art

A technology currently under review considers the development of an effective and efficient control strategy for the control of mechanical systems involving impacts [7][8]. Rijnen et al. have built a setup that allows a demonstration through the use of a rotary actuator coupled to a hammer that impacts a fixed base [9]. To allow for more complicated scenarios and demonstrations, without the use of an expensive robot that is not designed for impact, a test-bed would have to be designed. Preferably a system that has similar capabilities to robotics used in logistics operations. The control technique should be tested on a system that is low-cost, stable, and enables multiple degrees of freedom for object manipulation.

1.3 Goal and contribution

This study aims to develop a setup for the development and demonstration of robotic impact-aware manipulation. Challenges involved in developing the setup can be perceived both at a mechanical, as well as control level. On a mechanical level, measures need to be taken to avoid the impacts from undermining the robot's performance. From a control point of view, the system developed in this thesis is required to enable manipulation of objects at a kinematic level in several degrees of freedom, but still in such a way that it is controllable. The system is controllable if it allows predictable and reliable manipulation of objects.

In the development of the setup, different concept designs are introduced and evaluated. By evaluating the concepts based on functionality and mechanical feasibility, the most promising concept was adopted and developed into a high-level mechanical design, a design offering a foundation for creating a detailed design. Here, a detailed design is considered to be a design that enables manufacturing. The test-bed is built to execute tasks related to tossing, grabbing, and picking of items. These activities are associated with inevitable impacts. A mechanical design is introduced with these unavoidable impacts in mind and takes into account the peak forces that may occur during task-execution.

The second part of this development includes the functional validation through multi-body simulations of this setup design. The multi-body simulations are conducted to test and demonstrate the setup performance, including mechanical layout and control. Test routines are developed for the validation of different manipulation scenarios inspired by logistic processes.

1.4 Organization

This thesis starts by defining high-level goals for the development of the test-bed in Chapter 2. The report discusses Cartesian and revolute-based concepts considered for the development of the setup in Chapter 3. By comparing these concepts concerning the requirements, one concept is chosen for further development. The chosen concept is developed into a mechanical design in Chapter 4. Chapter 5 validates the mechanical design using multi-body simulations. In the end, conclusions and recommendations are presented in Chapter 6.

Chapter 2

Design requirements

Designing a system that can demonstrate impact-aware manipulation in a way that is exciting and educational, requires an understanding of what such a demonstration would require. As a start, this chapter defines high-level demands to achieve such a demonstration. Also, by taking inspiration from logistics, two challenging tasks are formulated for demonstrating with the setup. Translating these tasks into requirements, in combination with general requirements, leads to a requirements list to be used for the design of the test-bed.

2.1 High-level demands

High-level demands form a basis for the design of the setup. The demands are qualitative and must translate into quantitative requirements. In designing the setup, the aim is to design a setup which:

- is practical sized,
- impact resilient,
- offers exciting demonstrations,
- is designed for educational purpose, and
- allows tangible demonstrations.

The following paragraphs translate these qualitative demands into quantitative demands.

Practical sized. The setup needs to be of an acceptable size. An acceptable size would allow the setup to fit on top of a typical office desk. Requiring the robot to fit on a surface of $l = 2.0\,\mathrm{m} \times w = 0.8\,\mathrm{m}$. To still allow the setup to be transportable, the height of the structure must not surpass 1.5 m.

Impact resilient. Designing the setup for demonstration of impact-aware robotic manipulation requires it to cope with impacts on a control level, as well as a mechanical level. On a control level, the robot must be able to detect impacts as fast as possible. On a mechanical level, the robot must be able to withstand the effects of impacts between the end-effector and the object.

The peak force of an impact is related to the mass and velocity of the colliding bodies. Both the mass and velocity of the robot depend on variables that have yet to be determined—basing the velocity on the foreseen tasks of the robot, where the maximum velocity must at least be higher than the maximum expected collision velocity during task execution.

During the mechanical design of the test-bed, the maximum peak force the end-effector must be able to withstand, is based on the magnitude of the impacting mass. Impact resilience is achieved through a maximum impact velocity of the end-effector with a fixed object, which does not damage the robot. This maximum velocity is determined by the executed tasks discussed in Section 2.2.

Exciting demonstrations. Performing exciting demonstrations involves demonstrations that are dynamic and dexterous. Humans manipulate objects with dynamic and dexterous movements. By using this as a reference in terms of motion characteristics, the robot must be able to move at higher velocities than an average healthy human subject would be able to, assuming that high velocities and accelerations are impressive for demonstration. Following Bonkovic et al. (2009), a minimum velocity of $2\,\mathrm{m/s}$ and a minimum acceleration of $6\,\mathrm{m/s^2}$ meets this requirement [10].

Educational purpose. The setup is designed for educational purposes, demonstrating general robotic object manipulation as well as showing the value of impact-aware manipulation. As the setup is designed for educational purposes, the setup must allow a clear view for spectating demonstrations performed by the setup.

For the setup to allow a clear view, demonstrations performed with the setup must be observable by a broad audience. For this reason, a horizontal viewing angle of 120 degrees is required at the front of the setup. Within this viewing angle, there must be no obstructions for a spectator observing a demonstration.

Tangible demonstrations. The demonstrations performed by the setup must be applicable in real-world scenarios. Requiring the object to be of realistic size and weight. A cubical object with the size of $0.1\,\mathrm{m} \times 0.1\,\mathrm{m} \times 0.1\,\mathrm{m}$, is perceived as realistic. The setup is designed to handle cubicles made out of plastic. With an allowable object weight of up-to 1.5 kg, most types of plastic are accommodated [11].

2.2 Task-related requirements

This segment addresses the planned demonstrations and which criteria the test-bed must fulfill to enable such demonstrations to take place.

For the setup to allow tangible demonstrations, the demonstrations performed must cohere with real-world scenarios. In this case, a scenario involving object manipulation as part of logistics. The setup shall demonstrate that impact-aware manipulation has the potential to improve a robot's productivity and decreases a robot's footprint. A relatively small robot utilizing impact-aware manipulation may have the same performance as a big robot using conventional object manipulation.

The following section first addresses two standard logistic processes, forming an inspiration for the performed demonstrations with the setup. Consequently, this section is followed by the suggestion of two challenging tasks for demonstrating impact-aware manipulation.

2.2.1 Logistical processes

Palletizing and handling of luggage are typical instances of logistical procedures. Covering these two processes allows forming an idea on what these processes consist of, and how they might translate into tangible demonstrations.

Palletizing. Palletizing involves moving items from a queue to a pallet. The items often consist of containers of cardboard disclosing various goods. By positioning the boxes in a particular layout, the robot creates a safe and stable stack of items. This process is depicted in Figure 2.1 [1]. Cardboard boxes frequently enclose products that can withstand bumps, and shocks, without degrading the functionality of the product. Two examples of such products are clothes and food products. Stacking boxes is not an activity that involves extraordinary precision. Handling robust items without extraordinary precision renders it a job that is successfully performed by humans, providing the weight is within capable limits of the human. A human grabs the object, whereas the robot picks it, but the process is similar for both. The major disparity, as shown in Figure 2.1, is the robot's footprint and weight relative to the object's mass and size.

It provides a possibly useful application for impact-aware manipulation and an appropriate motivation for developing a task to be performed by the test-setup.

Luggage handling. Luggage management is often carried out as part of a logistic process at airports; it requires the placement of pieces of luggage inside a container for transportation. The process is seen in Figure 2.2 [2]. As with palletizing, the displaced items are typically items that can withstand an impact or shock. By applying an impact-aware manipulation strategy, the time it takes to pick pieces of luggage from a belt and to position them in a container may likely be reduced.

Several more examples exist. If the handled object is resilient to the effects of impact, and the conveyed motion is not required to be precise in the order of millimeters, then an impact-aware manipulation technique may give a reduction in task execution-time compared to traditional methods.

Figure 2.1: Example of a Cartesian (3PR) palletizing robot [1].

---

[1] Delta Industrial robot for palatalizing, retrieved from `https://www.youtube.com/watch?v=XSiHLHvn2M&list=PLopUrYtSBnSOGxv7dFNFpPXBUuY37Ns&index=8` on 25-04-2019

[2] DGWorld: BagBot, retrieved from `https://www.dgworld.com/` on 22-05-2019

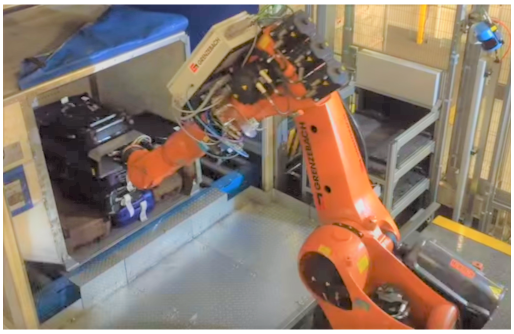

Figure 2.2: Example of an articulated (6R) luggage handling robot [2].

2.2.2 Task descriptions

By choosing two challenging tasks that are inspired by the processes discussed in the previous section, and defining requirements based on these tasks, the resulting requirements allow for a wide range of use-cases. The following two sections discuss these tasks.

Throwing and catching. Both palletizing and luggage handling require the transportation of items. The transportation step requires a robot large enough to be able to pick objects from a source and move them to the destination. The transportation step may also be possible using two smaller robots throwing the objects from one robot to the other. This activity includes simultaneous impacts, particularly during item catching. By throwing and catching objects within the enclosure of the robot, the aim is to mimic this way of inter-robot transportation. Figure 2.3 explains this activity by depicting a series of time-frames. Table 2.1 lists every time-step depicted in this chart together with a description.

At t_0, the robot starts by clamping the object between the end-effectors. The clamping force is proportional to the friction between the target and the end-effector. At t_1, the robot accelerates the object, and at t_2, the object has attained a specific upward velocity. While releasing the objects at t_3, the arms decelerate to allow capturing the object as it returns. At t_4, the object moves up, approaches a vertical velocity of zero, and proceeds to drop to the floor. The end-effectors approach the object at t_5 and catch it at t_6. In establishing contact, the robot's arms do not slow down until the arms hit the object, causing an impact between the end-effectors and the target.

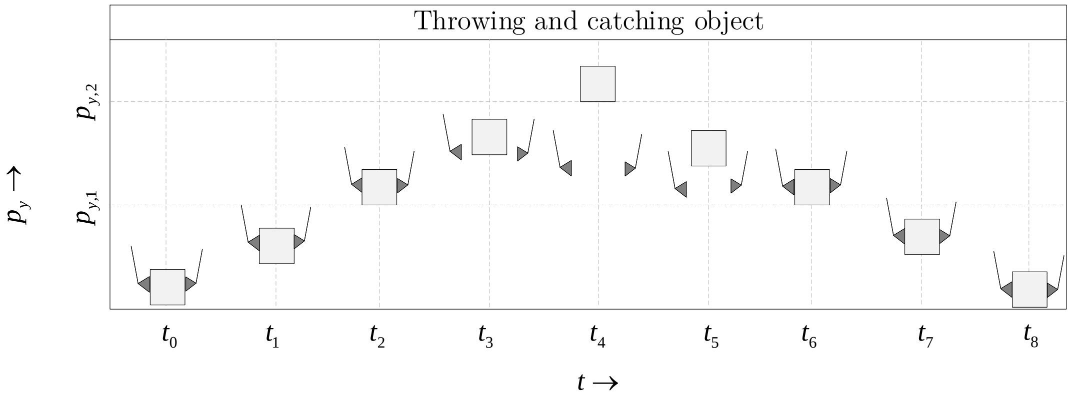

Figure 2.3: Parametric timeline of object state in throwing and catching of object, showing the vertical position of the end-effector and object over time.

Table 2.1: Description parameters used in Figure 2.3, describing throwing and catching of object.

time-step	description
t_0	The robot establishes contact with the object.
t_1	The object is vertically accelerated with an acceleration of a_y.
t_2	The object is released at height $p_{y,1}$ with an upward velocity of v_y.
t_3	The object is decelerating with gravitational acceleration g; the robot's end-effector is decelerating at a higher rate.
t_4	The object reaches a height of $p_{y,2}$, where vertical velocity is zero.
t_5	The object is accelerating with g; the robot is in a position to catch the object.
t_6	The robot catches the object, which is moving at a velocity of $-v_y$.
t_7	The object is decelerated at a_y.
t_8	The object is positioned back on the ground.

Throwing the object to a height of $p_{y,2} = 0.8\,\mathrm{m}$ allows for an exciting demonstration, visible to the audience. Such a height roughly corresponds to an eye-level of sight when placing the robot on top of a table. The flying distance must be higher than the acceleration distance, requiring the acceleration distance of the object to stay below $p_{y,1} = 0.3\,\mathrm{m}$, making the task more interesting.

Figure 2.4 depicts a motion profile that corresponds with the requirements on object throwing height, and acceleration distance, by showing the vertical position of the object, p_y, over time. The profile does not show the horizontal position of the object; this position should not change. However, the object has a size of 0.1 m×0.1 m×0.1 m, and might show horizontal drift while flying, due to imperfections in throwing the object. For this reason, a slack of 0.15 m is added on either side of the object. This slack, in combination with the object size, requires a workspace width of at least 0.4 m.

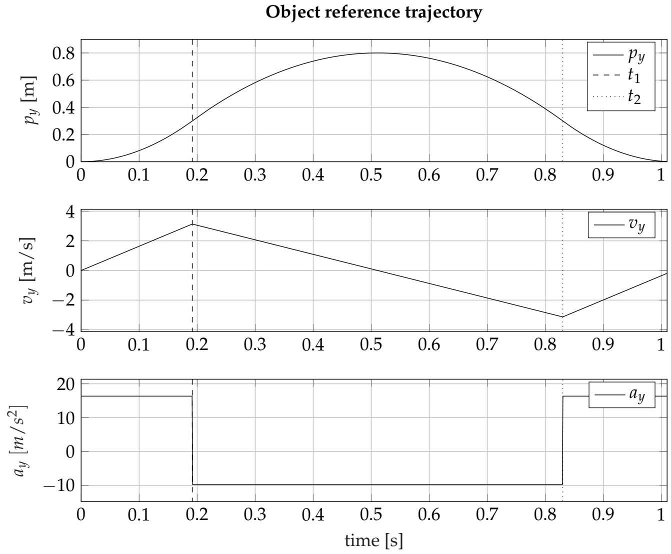

Figure 2.4: Object state trajectory during throwing and catching, showing the vertical position, velocity, and acceleration of the object, and the moment of release (t_1) and catch (t_2).

Extracting the requirements on position, velocity and acceleration from Figure 2.4, and taking into account the extra slack for horizontal drift while flying, leads to the following requirements:

- a maximum vertical acceleration of $a_{y,min}$ =17 m/s^2,
- a maximum horizontal velocity of $v_{y,min}$ =3.2 m/s,
- a horizontal impact resilience for velocities up to 2 m/s,
- a workspace height of $h_{w,min}$ =0.8 m, and
- a workspace width of $w_{w,min}$ =0.4 m.

Grabbing and placing. The previous task related to transportation, this task relates to the procedure which comes before and after transportation. Both palletizing and luggage handling involve picking and placing of objects. Conventionally, a robot positions its gripper over an object, establishes contact, and then moves the object to a predetermined location. Contacts between robot and object, or robot and surroundings, are formed at a minimal velocity relative to the robot's overall motion. Impact-aware manipulation could minimize the time spent accelerating and decelerating by grabbing and placing the object. Figure 2.5 presents an example of grabbing and placing an item. Depicting each time-step with a position p_x, for which each step is listed in Table 2.2.

At t_0, the end-effectors, or fingers of the end-effector, start at a distance of 0.15 m away from the object. At t_1, the end-effectors grab the object, and transport the object across the workspace, t_1-t_5. At t_6 and t_7, the object is positioned by hitting the ground with both arms and object.

This task consists of a horizontal, as well as a vertical movement. The dimensions are chosen similar to the capabilities of a human, to make the demonstration exciting and tangible. The robot moves an object over a horizontal distance of 0.5 m. This distance roughly corresponds with the length of an arm without the hand. The object moves at an average horizontal velocity of $v_x = 1$ m/s, making it comparable with human capabilities [10]. Picking and placing often involve avoiding objects; for this reason, the arms have to virtually move over an object placed at the center of the workspace.

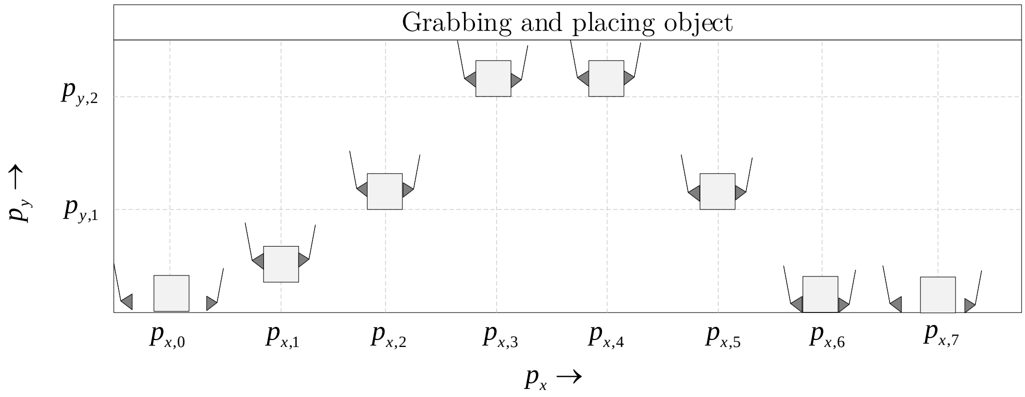

Figure 2.5: Parametric description of object state in grabbing and placing an object, showing the vertical and horizontal position of the end-effector and object over different time-steps.

Table 2.2: Description parameters used in Figure 2.5, describing grabbing and placing of an object.

time-step	position	description
t_0	$p_{x,0}$	The end-effector accelerates towards the object with a horizontal acceleration a_x, and vertical acceleration a_y.
t_1	$p_{x,1}$	The end-effector establishes contact with the object at a horizontal velocity of v_x, and vertical velocity v_y.
t_2	$p_{x,2}$	The object is horizontally accelerated with a_x to $v_x = v_{x,max}$, and decelerated vertically with $-a_y$.
t_3	$p_{x,3}$	The object reaches a height of $p_{y,2}$, and continues horizontal movement.
t_4	$p_{x,4}$	The object reaches position $p_{x,4}$, and the end-effector starts a downward motion.
t_5	$p_{x,5}$	The object is moving down towards the destination.
t_6	$p_{x,6}$	The object is placed on the floor at position $p_{x,6}$.

Figure 2.6 depicts a motion profile that corresponds with the requirements to grab and place an object. The profile does show the horizontal position of the object, but it does not show the room required for approaching the object. For this reason, a slack of 0.15 m is added on either side of the profile. This slack, in combination with the motion profile, requires a workspace width of at least 0.8 m.

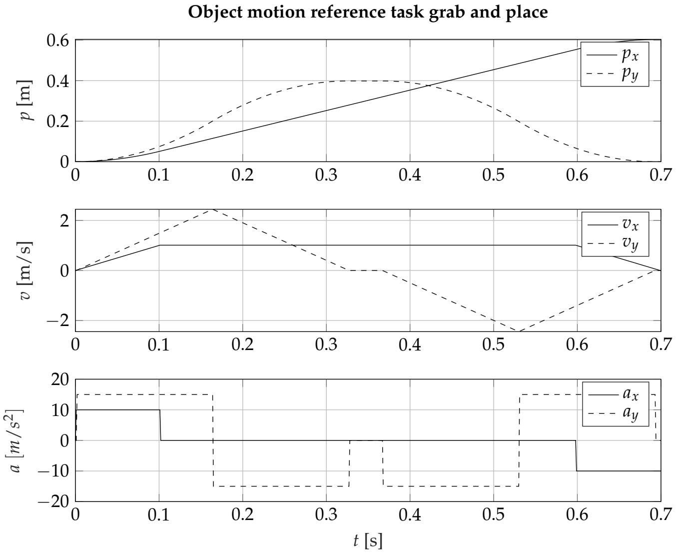

Figure 2.6: Object state trajectory during grabbing and placing, showing the horizontal and vertical position, velocity, and acceleration of the object.

Extracting the requirements from the motion profile in Figure 2.4 in combination with the added slack leads to the following requirements:

- a vertical acceleration of $a_{y,min} = 15\,\mathrm{m/s^2}$,
- a horizontal acceleration of $a_{x,min} = 10\,\mathrm{m/s^2}$,
- a horizontal velocity of $v_{x,min} = 1.2\,\mathrm{m/s}$,
- a vertical velocity of $v_{y,min} = 2.2\,\mathrm{m/s}$,
- a vertical impact resilience for velocities up to 2.5 m/s,
- a workspace width of $w_{w,min} = 0.8\,\mathrm{m}$, and
- a workspace height of $h_{w,min} = 0.3\,\mathrm{m}$.

2.3 Requirements list

The requirements determined in the previous sections are summarized in the following overview. Table 2.3 lists all requirements for the setup. These requirements are used to develop concepts, and to design the robot.

Table 2.3: Requirements for test-bed for impact-aware robotic manipulation.

Requirements	**Required value**	**Description**
Dimensions		
Footprint	2 × 1 × 1.5 m *($l \times w \times h$)*	Maximum footprint of setup
Object size	0.1 × 0.1 × 0.1 m	Minimum object size
Object weight	*at least up to* 1.5 kg	Maximum object weight
Object shape	*Box*	Object shape
Throw and catch scenario		
Cooperative bi-manual workspace	*min* 0.4 × 0.4 m *($l \times h$)*	Unobstructed space within reach of both arms
Vertical acceleration	*min* $17\,\mathrm{m/s^2}$	Minimum vertical acceleration for task
Vertical velocity	*min* $3.2\,\mathrm{m/s}$	Minimum vertical velocity for task
Workspace	*min* $0.4\,\mathrm{m} \times 0.8\,\mathrm{m}$ *($l \times h$)*	Required workspace size
Grab and place scenario		
Vertical acceleration	*min* $15\,\mathrm{m/s^2}$	Minimum vertical acceleration for task
Horizontal acceleration	*min* $10\,\mathrm{m/s^2}$	Minimum horizontal acceleration for task
Horizontal velocity	*min* $1.2\,\mathrm{m/s}$	Minimum horizontal velocity for task
Workspace (co-)man. objects	*min* $0.8\,\mathrm{m} \times 0.3\,\mathrm{m}$ *($l \times h$)*	Minimum object size for specific task
General		
Impact resilience	*at least up to* $2\,\mathrm{m/s}$	Maximum impact velocity between end-effector and a fixed object.
Viewing angle	*at least up to* 120°	Minimum viewing angle from front

Chapter 3

Design conceptualization

The requirements, as described in Chapter 2, enable the search for a functional design concept. This chapter discusses several concepts and provides an analysis of these concepts. The chapter begins with some considerations in creating valid concepts, after which it discusses the concepts considered to be valid. The two most viable concepts are discussed in this chapter, Appendix A discusses the remainder of the concepts. The chapter elaborates on the properties of each of the considered concepts and compares the concepts based on the criteria set out in the previous chapter. As a consequence, this chapter concludes with a decision on the concept used for the design of the test-bed.

3.1 Design considerations

A requirement-satisfying setup is a broad notion. It leaves room for many different concepts. As a guideline, we formulate design guidelines supporting the conceptualization process. The following sections address these considerations.

3.1.1 Dual-arm manipulation

To enable a meaningful and exciting demonstration as described in Chapter 2, we consider two-arms concepts. Using a two-arm setup to manipulate items, parallels the way that humans handle objects. Two manipulators form a closed kinematic chain, with an object as part of the chain. The closed kinematic chain offers a parallel manipulator's stiffness and strength, coupled with the dexterity and freedom of movement, of a serial manipulator. Both properties are useful for this particular system, as the tasks involve impacts, and demand strong dexterity and motion flexibility.

Definition dual-arm robotic manipulation. Dual-arm robotic manipulation can be either uncoordinated manipulation, where two arms perform two separate tasks, or coordinated manipulation, where two arms perform part of the same task [12]. The latter is sub-divided into goal-oriented and bi-manual manipulation. Herein, goal-oriented manipulation does not indicate simultaneous physical contact with an object, where bi-manual manipulation does. The design of the test-bed accommodates coordinated manipulation, focussing on bi-manual manipulation.

Defining the workspace of a robot, as the collection of points within reach of the robot's end-effector, is generally valid. However, in the case of a two-armed robot, this notion is not functional. Each arm can reach a separate set of points using the end-effector, and both arms are part of the same robot. As a solution, the workspace is divided into a bi-manual manipulation workspace and a goal-oriented manipulation workspace. This devision is defining the workspace for bi-manual manipulation, as the collection of points that can be reached by both end-effectors, and defines the workspace for goal-oriented manipulation, as the sum of points that can be reached by the individual end-effectors.

3.1.2 Dimension of setup

The considered concepts for the test-setup offer planar or full degree of freedom (DOF) object manipulation. The following two paragraphs discuss the difference between these two.

Planar manipulator. A planar manipulator involves manipulating an object, translating, and rotating in a single plane. The enclosure of the robot restricts the object from moving in other directions. For example [13] restricts the object with a glass panel in the front, and behind the manipulated object. Grease lubricates the surface; to reduce friction between the objects and the panels. The planar concept for this setup adopts the same approach, constraining the object between two transparent plates. Using grease may not be necessary. If the object can move freely through the entire enclosure, this idea is feasible. It does require the plates to be even. In this requirement, even means that the plates are flat, without interruption. Figure 3.1 illustrates a situation in which an uneven rear plane traps an object at the location of a gap.

Full DOF manipulator. A three-dimensional concept involves an unconstrained object moving and rotating in any direction. The workspace has a box-like structure, residing the object and robot in a predominantly transparent enclosure.

3.1.3 Direct-drive actuator

Chapter 2 states that the design of the setup requires to be resilient to impact. The design involves the selection of actuators, and the implementation method of the actuator influences its impact resilience. Two methods of implementing an electric actuator are direct-drive and geared-drive. A direct-drive does not use a gearbox, where a geared drive does. A gearbox allows altering the torque or speed of the actuator, applied to the load, through a train of gears. When designing for impact resilience, a gearbox introduces an extra layer of complexity. A direct-drive implementation reduces the complexity of the design, as it reduces the number of components in each joint, and does not require a gearing which may be susceptible to impact-related failure [14].

Figure 3.2 depicts an example of a direct-drive motor. In combination with an iron core, both linear and revolute motors utilize both permanent magnets and electromagnetic coils.

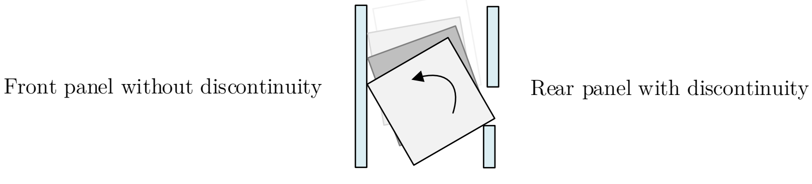

Figure 3.1: Side-view of planar manipulator showing a stuck object between front and rear panel due to a gap in the rear panel.

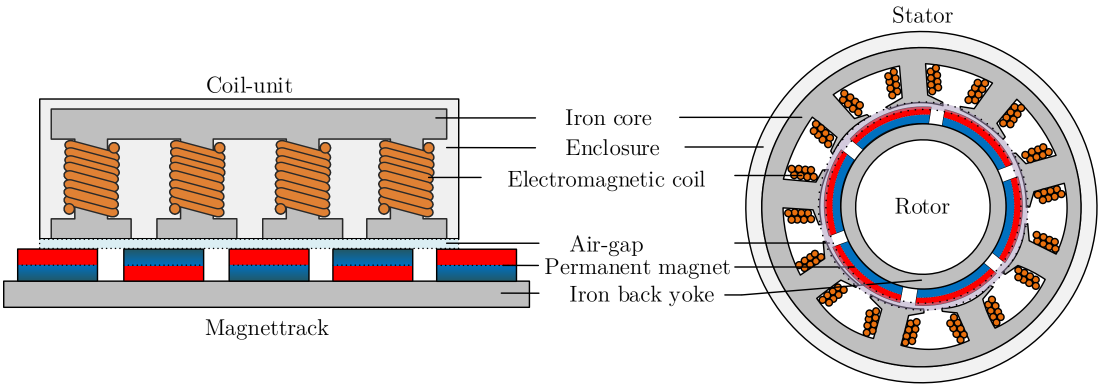

Figure 3.2: Illustration of a cross-section of a direct-drive permanent-magnet linear- and rotary motor.

Both the linear- and the revolute motor work with a moving and a static component, divided by an air gap smaller than a millimeter [15][16]. Bearings are used to maintain this air-gap. The bearings must be adequately stiff to avoid the elimination of the air-gap to harm the actuator. Notice that the air-gap can be raised in the case of linear motors to boost robot robustness at the cost of a reduction in actuator efficiency and maximum thrust.

3.2 Planar manipulator concepts

Throughout the conceptualization of this project, a two-dimensional concept was found more realistic than a full DOF manipulator. The planar concept provides a balance between sophistication and cost of the system, and the opportunity to show impact-aware manipulation. The following section explores feasible two-dimensional concepts. The remainder of the concepts not discussed in this chapter are found in Appendix A.

Cartesian planar manipulator. Figure 3.3 shows a sketch of a Cartesian planar manipulator. The concept implements two linear motion actuators, connected in series, in a two-arm configuration. Actuating both arms in the x-direction, stage x (C13), and y-direction, stage y (C14). Herein defining the x-axis to be horizontal, and the y-axis to be vertical. The x-axes of these two arms coincide spatially. In this way, both arms can function within a single enclosure (C11 C12 C15), in a single plane, analogous to the object's motion plane. The concept allows object manipulation through the end-effector (C16) mounted to the bottom of the y-stage.

This concept allows an object to be bi-manually displaced. It enables the translation of the object by simultaneously moving both arms in the same direction while clamping the object between the end-effectors. It enables rotation of a clamped object by altering the height of both end-effectors in the opposite direction, as depicted in figure 3.4. It does require sufficient friction from the interface between the object and the end-effectors to keep the object from slipping.

Concerns in the realization of this concept are:

- The considerations at the start of this chapter mention that a two-dimensional configuration includes two geometrically continuous planes in the front of, and behind the robot's arms. In this case, the x-stage disrupts the rear plane, creating a gap for attachment of the y-stage. The created gap must be minimal or covered.

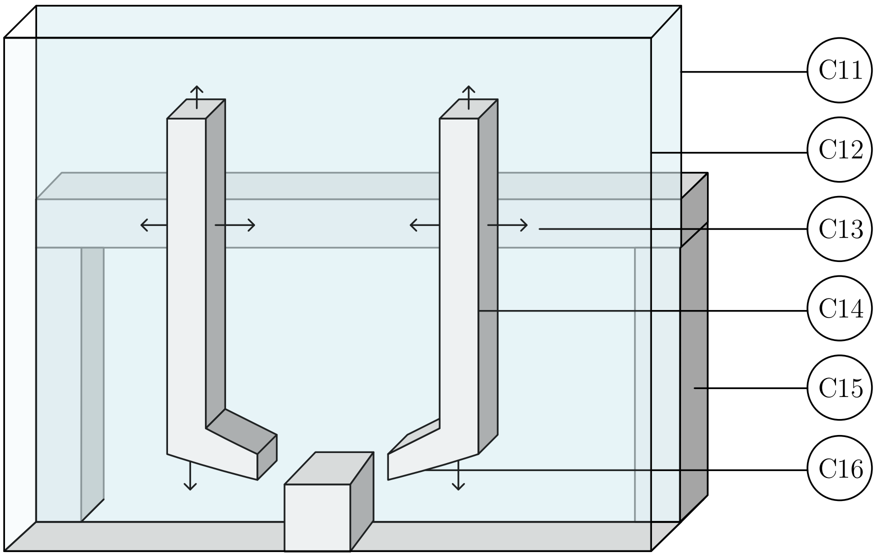

Figure 3.3: Concept Cartesian planar manipulator with: enclosure rear-panel (C11), enclosure front-panel (C12), horizontally moving stage (C13), vertically moving stage (C14), supporting structure (C15), and end-effector (C16).

- While this concept claims to allow rotation of an object in coordinated bi-manual manipulation, it demands a careful combination of end-effector design and setup control to make it functional.
- Forces applied in a horizontal direction to the end-effector have a significant arm, which results in a significant moment applied to the x-stage. This significant moment involves the careful design of the x- and y-stage bearings and structure.

Advantages in the realization of this concept are:

- The design includes four actuators, of which two of the four use the same magnet-track. Compared with other two-arm concepts, this is perceived to be a minimal number.
- This design allows the use of direct-drive actuators, and possibly, modification of the air gap between the moving and the non-moving part of the actuator. Considering this possible modification to be beneficial when designing for impact resilience, as it permits greater deformations without causing problems in the actuator.

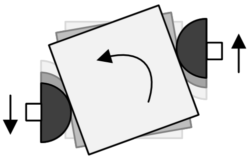

Figure 3.4: Illustration of object counter-clockwise rotation through translation of the end-effectors using the planar Cartesian manipulator.

- A two-arm Cartesian concept allows for a large workspace to bi-manually manipulate objects. It offers versatility in terms of potential movement activities that can be accomplished with this configuration.

Planar revolute joint based manipulator. Figure 3.5 depicts a planar manipulator based on revolute joints. The concept consolidates two arms, which both comprise of three rotary actuators (C21) in series. The actuators link three arm-segments to a common base (C24) for both arms. The first and second arm-segments are of the same length; the last arm-segment is the end-effector (C25). Similar to the previous planar concept, the arms move in the same plane of motion as the object, with a front- and rear plane (C22 C23) constraining the object. Variations to this design are discussed in Appendix A.

Using two arms, this concept can translate, and rotate, an object inside the cooperative bi-manual workspace. The arms also allow goal-oriented object manipulation, such as separating two objects located next to each other, by moving the objects apart.

The concerns in the realization of this concept are:

- The arms are connected to the workspace's outermost corners. Allowing the task of grabbing and placing objects as described in Chapter 2, requires the arms to be quite long compared to the setup's overall measurements. Long arms imply significant weights and moments, requiring considerable torque. Delivering the torque needed for this principle is not ideal for direct-drive motors.
- Direct-drive joint actuators have a predetermined air gap, with a typical value of 5×10^{-4} m [15]. This property can not be customer-influenced. It requires the bearings to be sufficiently rigid when designing for impact, to maintain this air-gap.

Advantages of choosing this setup are:

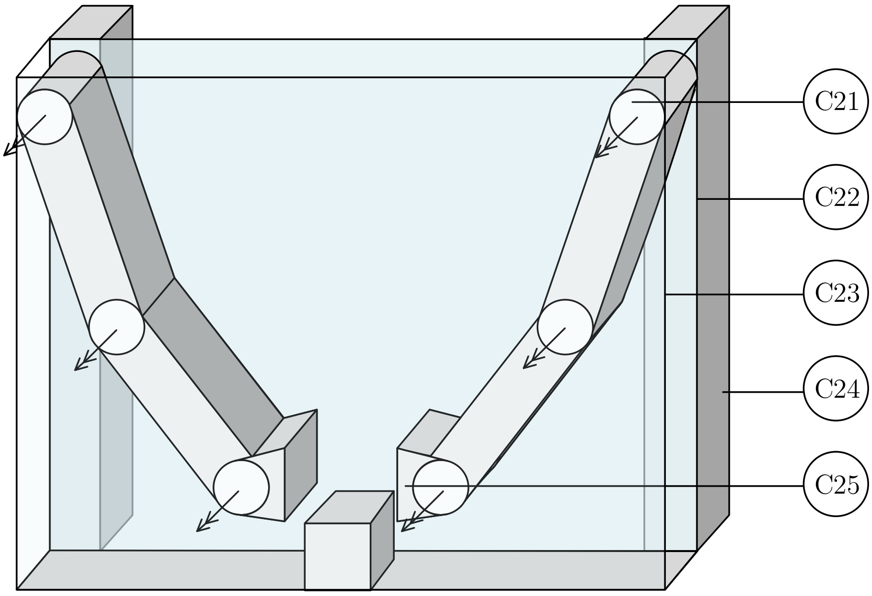

Figure 3.5: Revolute-joint based planar manipulator concept design with: revolute joints (C21), rear-panel enclosure (C22), front-panel enclosure (C23), supporting frame (C24), and end-effector (C25).

- The ability to manipulate objects is more sophisticated than that of the Cartesian planar manipulator, enabling one, or two, arms to translate and rotate objects.
- With the arms connected to either side of the workspace, the front and rear panels are not interrupted. Implying that there is no need for a special mechanism, as is the case for the Cartesian concept.
- A long arm does not intensify forces introduced at the end-effector, the actuator defines the maximum force applied to the end-effector. Forces higher than this maximum force cause rotation of an arm-segment instead of deformation.

3.3 Comparison of design concepts

The concepts addressed here are compared based on the requirements described in Chapter 2. Table 3.1 shows this comparison. Note that some of these definitions are only addressed in Appendix A.

Dimensions. Each concept allows a system configuration that suits the defined footprint specifications.

Throw and catch. Throwing and catching objects is spatially possible for each of the concepts. However, the vertical acceleration requires substantial force or torque from actuators. Such a large amount of torque is difficult for revolute joint based actuators, as mentioned in Appendix A. Throwing and catching with the Cartesian 3D manipulator is challenging in terms of stiffness criteria, demanding a robust support framework that raises the robot's expense and weight disproportionately to the limited amount of advantages it offers.

Grab and place. The Cartesian manipulators can spatially grab and place, but this is not the case for Revolute joint-based manipulators. Due to the required width of the workspace for bimanual manipulation of objects, and the maximum permitted footprint of the system, grabbing and placing is not possible for the revolute planar concept.

General. The cost of a three-dimensional setup makes it a concept that is too expensive and complicated for a test-bed.

Table 3.1: Comparison table of different concepts.

Concepts / **Requirements**	Revolute 2D variation 1	Revolute 2D variation 2	Cartesian 2D variation 1	Cartesian 2D variation 2	Cartesian 3D	
Dimensions						
Footprint	●	●	●	●	●	*max* $2 \times 1 \times 1.5$ *m (L×W×H)*
Object sizes	●	●	●	●	●	$0.1 \times 0.1 \times 0.1\mathrm{m}$
Object weight	●	●	●	●	●	*up to* 1.5 *kg*
Throw and catch						
Workspace (co-)manipulation	●	●	●	●	●	*min* 0.4×0.4 *m (L×H)*
Vertical acceleration	●	❍	●	●	❍	*min* $17\,\mathrm{m/s^2}$
Vertical velocity	●	●	●	●	●	*min* $3.2\,\mathrm{m/s}$
Workspace clearance	●	●	●	●	●	*min* 0.3×0.9 *m (L×H)*
Grab and place						
Vertical acceleration	●	❍	●	●	❍	*min* $15\,\mathrm{m/s^2}$
Horizontal acceleration	●	●	●	●	❍	*min* $10\,\mathrm{m/s^2}$
Horizontal velocity	●	●	●	●	●	*min* $2\,\mathrm{m/s}$
Workspace (co-)man. object	▲	▲	●	●	●	*min* 0.8×0.3 *m (L×H)*
General						
Impact resilience	●	●	●	●	❍	Allow impacts up-to $2\,\mathrm{m/s}$
Viewing angle	●	●	●	●	●	Allow a viewing angle of at least 120°
Cost	●	●	●	❍	▲	Comparing costs with design complexity

▲ Req. not met ❍ Challenging req. ● Req. met

3.4 Discussion

The Cartesian planar manipulator, and the revolute-joint planar manipulator, are the two main concepts explored in this chapter. Both concepts show benefits and drawbacks.

The Cartesian planar manipulator is capable of performing the mentioned tasks, with a limited amount of actuators, while providing a comprehensive bi-manual manipulation workspace. The Cartesian planar manipulator is also feasible in terms of the required force, and the available actuators to allow a direct-drive approach. However, designing this concept does require taking into account the effect of the long arm of forces applied to the end-effector.

The revolute-joint planar manipulator enables the throwing and catching of objects, providing the actuators can provide the necessary torque. The concept does not enable object grabbing and placing according to the motion profile discussed in 2.

Since a planar Cartesian architecture enables the execution of all projected tasks in conjunction with the necessary power, the following chapter pursues this concept and develops it into a mechanical design.

Chapter 4

Mechanical design of the test-setup

Chapter 2 addresses requirements for the test-setup, which are based on the tasks to be performed by the test-setup. Following the requirements, Chapter 3 compared different design concepts, leading to a final concept at the end of the comparison: the planar Cartesian manipulator.

Now, given the test-setup requirements, the concept is developed into an embodiment design—a design comprising of mechanical layout, dimensions, and specifications for actuators, guides, and materials. Before addressing the specific system configuration, this chapter addresses the effects of mechanical impacts during manipulation, and the required measures to minimize the harming effects of an impact.

This chapter has two sections. The first section of this chapter addresses the role of mechanical impacts in a mechanical system and how to enhance the mechanical design, given such impacts. The second section discusses the mechanical design of the setup.

4.1 Mechanical design coping with inevitable impacts

Impact-aware manipulation involves the impact between the robot and the handled items. While this manipulation technique may reduce task-execution time, it introduces rapid events with a high contact force, characteristic for impacts. It requires a setup that can withstand such impacts on a mechanical level.

The following section addresses the order of magnitude of peak forces arising during impact. After a general understanding of mechanical impacts, this section concludes with specific measures addressed to design with potentially harming effects of impacts in mind.

4.1.1 Impact analysis

Impacts occur when two bodies establish contact at a significant relative velocity, considering the time and spatial scale of the motion of both bodies. Both bodies accelerate or decelerate to a post-collision velocity, based on the mass ratio between the bodies. A peak force causes an abrupt increase in velocity, originating from the point of contact. These impacts are inevitable during task-execution and require the robot to withstand the potentially harming effects.

Withstanding the effects of impact requires absorbing the kinetic energy of the colliding bodies. The energy is either stored as potential energy or dissipated. The following analysis assumes

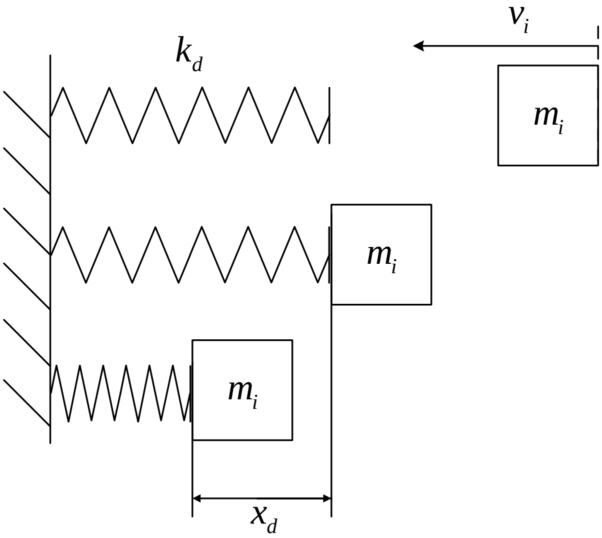

Figure 4.1: Model to visualize an impacting mass m_i with a pre-impact velocity v_i colliding with a spring representing the structural stiffness of the robot k_d, penetrating to a distance of x_d.

that all kinetic energy involved with the impact is stored as potential energy in the structure of the colliding bodies. Herein, analyzing the required stiffness of the entire impacting structure on the ability to store all kinetic energy as potential energy, while allowing strictly elastic deformation. Figure 4.1 represents a one-dimensional representation of this, where a single mass, in conjunction with a spring, is used to assess the peak-forces involved with the impact. The spring represents the stiffness of the entire impacting structure in an impact with a fixed object or surface.

Figure 4.1 depicts a mass, m_i, with an initial velocity of v_i. The mass moves towards a mechanical spring of stiffness k_d, which it penetrates to a depth of x_d. The mass has a kinetic energy of E_{kin}, where:

$$E_{kin} = \frac{1}{2} m_i v_i^2. \tag{4.1}$$

In considering the moving mass to be rigid, the spring absorbs all kinetic energy by compressing the spring to a depth of x_d and storing it as the potential energy of E_{pot}:

$$E_{pot} = \frac{1}{2} k_d x_d^2. \tag{4.2}$$

Equation (4.1) in combination with (4.2) leads to the following total impact penetration distance:

$$x_d = \sqrt{\frac{m_i}{k_d}} v_i, \tag{4.3}$$

for which the average impact force over the penetration distance is given by:

$$F_{avg} = \frac{1}{2} k_d x_d = \frac{1}{2} v_i \sqrt{m_i k_d}. \tag{4.4}$$

As the impact force causes an indentation of the spring k, the time consumed by the impact is based on the natural frequency of the undamped mass-spring system:

$$T = \frac{1}{2\pi} \sqrt{\frac{m_i}{k_d}}. \tag{4.5}$$

Rewriting (4.3), since the peak-force is determined by the stiffness of the spring in combination with the total penetration:

$$F_{peak} = \sqrt{m_i k_d} v_i. \tag{4.6}$$

Equation (4.6) shows that the impact velocity has a linear relation with the peak-force while mass and stiffness have a quadratic relationship with the peak force. The following equation provides an insight into the required maximum stiffness of the spring depicted in Figure 4.1, where:

$$k_{max} = \left(\frac{F_{peak}}{v_i \sqrt{m_i}} \right)^2 . \tag{4.7}$$

Note that having a large indentation might be beneficial to reduce peak-force, a low arm-distal stiffness could pose implications for the ability of the robot to manipulate objects. The mass of the arm is preferred to be as low as possible to minimize peak-force, and to minimize requirements on actuators and guides.

Example. To provide an order of magnitude, in case of a mass of $m_i = 10\,\text{kg}$, a velocity of $v_i = 2\,\text{m/s}$, and a spring of $k_d = 1\,\text{MN/m}$, the average impact-force over penetration distance $F_{avg} = 3.2\,\text{kN}$, and the peak-force is $F_{peak} = 6.3\,\text{kN}$. The corresponding time for this collision to reach peak-force is equal to $t = 5\,\text{ms}$.

4.1.2 Critical components

As mentioned in the previous section, impacts are unavoidable and initiate peak forces. This section discusses the critical components in this setup's mechanical design, considering critical components to be components that functionally degrade due to the effect of peak-forces. As a consequence, critical components define the magnitude of tolerable forces.

The two critical components in this design, are the guides and the actuator; the guides have a maximum load-bearing capacity, the actuator requires maintaining an air gap between the coil-unit and the magnet-track.

In the design of the test-setup, the aim is to use the peak force involved with an impact, as determined in section 4.1.1, and perform a static force analysis to determine the load on the bearings corresponding with a peak-force exerted on the end-effector. Through the design of a compliant end-effector structure, we aim to reduce the peak-force involved with the impact, and as a consequence, the peak-force exerted on the guides.

4.1.3 Robotic systems coping with impact

The previous section showed that the peak force exerted on the end-effector must be below an acceptable limit. Aside from introducing peak-forces, impacts cause vibrations within the robot to occur. These vibrations should be dampened as it could decrease the performance of the robot, and could functionally degrade the mechanical structure of the robot. The following analysis discusses the methods used for handling impacts throughout literature.

Humanoid or quadruped robots deal with impacts as part of their locomotion. Since this resembles the test-setup application, it provides an appropriate source of inspiration.

Compliance. Different ways exist to introduce compliance to a robot or structure. Compliance could be active or passive. Considering active compliance to be achieved through control of the actuators and passive compliance through mechanical structure design. Due to the rapid nature of impacts, it is not feasible to limit compliance to an active approach only [17]. It is thus required to implement a form of passive compliance to reduce peak impact forces. Introducing passive mechanical compliance is possible through compliant joint actuators [18]; through compliant structures such as spring elements, compliant mechanisms, and enclosed granular matter [19, 20, 21, 22, 23, 18]; and compliant materials such as visco-elastic materials and meta-materials [24, 25, 19, 20, 26].

The simplest compliance mechanism is implementing arm-distal compliance, considering the method to be simple, as it allows designing a stand-alone part instead of an integrated part. The arm-distal compliance forms an interface between the tip of the end-effector and the arm of the robot. The arm-distal compliance, as part of the end-effector, creates a tool for limiting the peak-force exerted on the guides. If designed correctly, it creates a cost-effective mechanism that limits the peak-force exerted on the guides or breaks if the exerted peak-forces are too high.

Damping. Damping, as part of a robot or structure, is also achieved through active control or passive mechanical damping. As discussed in the previous paragraph, it is not feasible to solely rely on active damping due to the rapid nature of the impacts. Options to introduce damping through passive mechanisms are through the passively regulated displacement of gasses or liquids [19]; through the usage of visco-elastic materials or meta-materials [24, 25, 19, 20, 26]; or through the usage of granular matter [22, 23, 27].

Chapter 3 states a method to allow both rotation and translation of the object, using a spherical tip on the end-effector. It requires a tip that offers sufficient friction in interacting with an object. To incorporate this tip, and introduce sufficient damping to the end-effector, a rubber tip is used. Rubber offers a suitable friction coefficient, which is generally higher than $\mu = 1$ [28], and is available in various sizes and shapes, making it a suitable material for the tip of the end-effector.

4.1.4 Guidelines to design for impact

Concluding from the previous sections, using the following guidelines benefits the mechanical design of a robot in handling impacts:

- the design of the structure of the robot must protect the critical components of the robot;
- the structure must be as lightweight as possible;
- contact points that are susceptible to significant impact loads must be equipped with enough compliance and damping to protect the critical components.

4.2 Mechanical design of the test-setup

The scope of this project is to provide a blueprint showing a mechanical layout with advice on the required components and specifications. The mechanical layout includes both the placement of actuators, bearings, a supporting structure, and the surrounding structure of the setup. The advice on the required components and specifications provides a basis for a detailed mechanical design. Figure 4.2 shows the discussed subsystems in this chapter.

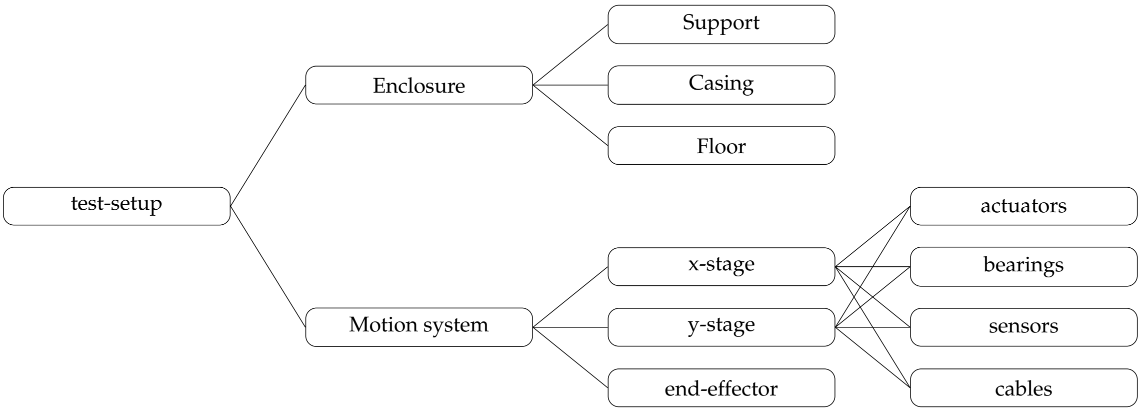

Figure 4.2: Function tree schematic showing the different sub-systems that are part of the test-bed.

Figure 4.3 depicts an illustration of the setup with balloon-labels indicating specific parts of the setup. The rest of this chapter refers to these components with the shown names. This chapter first discusses the design of the motion-system and ends with the design of the enclosure.

4.2.1 Foundation of motion system

This section discusses the layout of guides and actuators. These form the critical basis of the design.

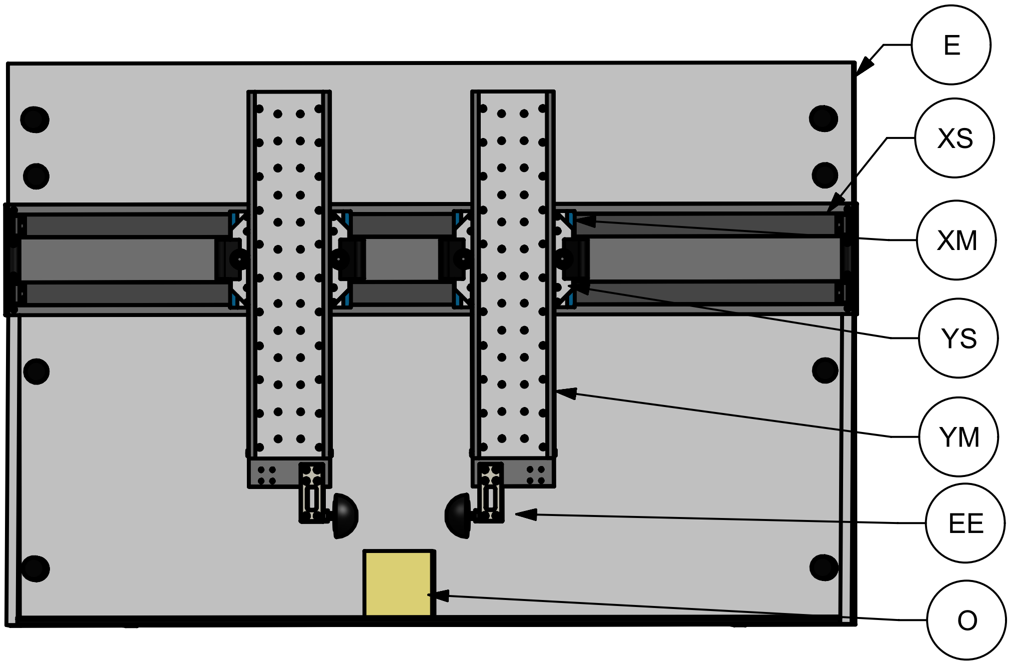

Figure 4.3: Overview of sub-systems and components of the test-setup with: the enclosure (E), fixed part of x-stage (XF), moving part of x-stage (XM), static part of y-stage (YS), moving part of y-stage (YM), end-effector (EE), and object (O).

Actuation. As discussed in Chapter 3, this setup uses direct-drive actuators. The setup is designed to use iron-core motors. A type of direct-drive linear motors driven using coils in combination with permanent magnets. This type of linear motor is efficient, offers a high thrust density, and allows varying the air-gap to design for robustness [29]. More information on the selection, properties, and an illustration, is found in Appendix D.

Guides. In selecting the guides, there are several considerations. Designing the arms to be as lightweight as possible, requires selecting the guides accordingly. To position the iron-core motors, and to allow a desired conversion of force to motion, the setup is designed with the use of linear motion guides. Information on the selection, properties, and an illustration is found in Appendix C.

Layout y-stage. In considering the mechanical layout with the use of iron-core motors, there are two options. Both options are depicted in Figure 4.4. The options are a vertical stage with a moving coil-unit (y4, left), or a vertical stage with a moving magnet-track (y1, right).

The main difference between one option or the other is that having a moving magnet-track requires a higher motor force compared to having a moving coil unit. The increase in required force is due to the weight difference of a magnet-track plus bearings (y3) and construction, as opposed to a coil-unit plus construction. In considering the moving mass of the x-stage, the total mass would be higher for the first option; it requires an extra part to house the magnet-track and guides.

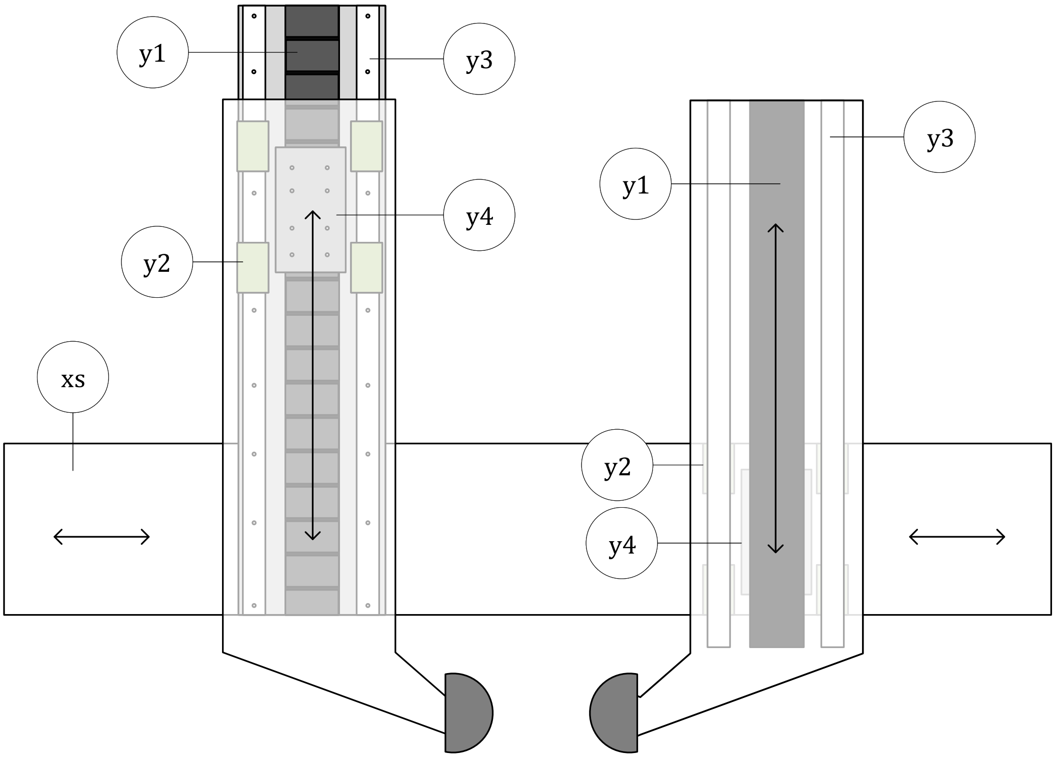

Figure 4.4: Two concepts for the y-stage layout to compare a moving coil-unit (left) to a moving magnet-track (right) with: the x-stage (xs), magnet-track (y1), carriage (y2), rail (y3), and coil-unit (y4).

Using the moving-magnet option does not require moving cables inside the arm, and the lever of forces applied to the end-effector is not always worst-case. Worst-case implies the maximum transfer ratio from forces applied to the end-effector to the guides, due to the lever of these forces. For the moving-coil option, the lever of these forces does not change.

The mechanical design of the setup adopts a moving magnet-track, minimizing the total moving mass of the system and reducing the loads on the guides as much as possible.

Strip-seal system. While the object is moving through the enclosure, it is undesirable if the front- or rear plane interferes with the object's motion. Although friction between the object and the enclosure is inevitable, hindrance from discontinuities within the front- or rear-plane should be averted.

The horizontal stage moves the vertical stage through a mechanical connection. This connection mechanically interrupts the rear-plane of the enclosure through an opening. This opening forms a discontinuity of the rear-plane of the enclosure, but if the hindrance is not substantial, it has a minimal influence on the movement of the object. Even a minimal opening allows the object to jam, as is discussed in Section 3.1.

The opening is covered completely using a liftable cover strip. The strip allows connecting the x- and y-stage, and prevents jamming of the object. Actuators meant for clean-room applications use this mechanism; it serves as a seal that prevents debris and dust from entering or leaving the actuators. The mechanism is illustrated in Figure 4.5. To reduce friction, unlike the depicted mechanism, it is best integrated with the use of rollers to guide the strip.

Layout of x-stage. The horizontal stage, also named x-stage, is designed according to the concept depicted in Figure 4.6, showing a static and a moving part.

The static part includes the sealing strip (xs1), guides (xs2), the magnet-track (xs3), and a set of magnets (xs4) to align the sealing strip. The moving part consists of a mounting for the y-stage (xm1), carriages (xm2), and a coil-unit (xm3).

The x-stage uses a single magnet-track to allow the actuation of both arms through moving coil-units. Using linear guides over the entire stroke of the x-stage separates the coil-unit from the magnet-track. The sealing-strip sticks to the x-stage with the use of magnetic strips, as the y-stage moves horizontally, it lifts the cover-strip from the magnetic strips.

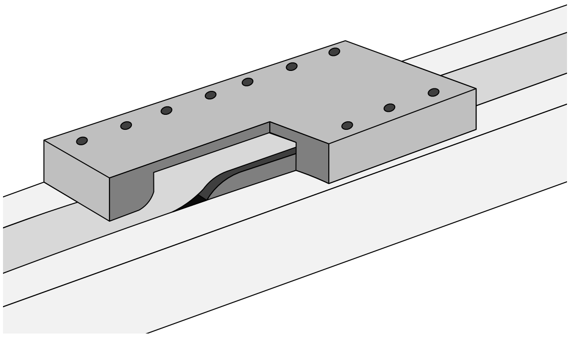

Figure 4.5: Illustration of a mechanism to implement x-stage drive in the rear plane, showing a metal strip that is lifted by a carriage to create a structural connection between the interior and exterior of the drive.

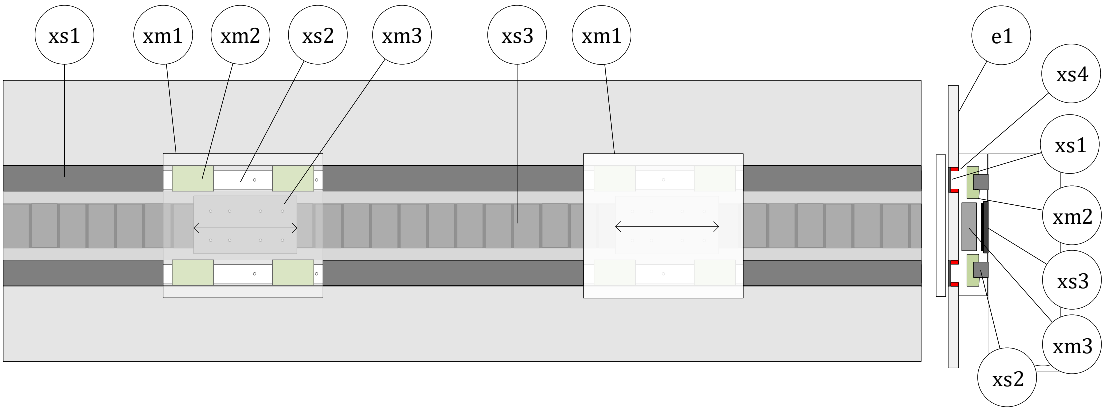

Figure 4.6: Concept for layout of x-stage, showing front (left) and side-view (right) with: a metal strip (xs1), rail (xs2), magnet-track (xs3), (xs4), xy-stage mover (xm1), x-stage carriage (xm2), coil-unit (xm3), and enclosure (e1).

4.2.2 Design of y-stage

The y-stage combines a structural part, an actuator part, and a guiding part. It consists of two different sub-systems: a static part (YS), mounted to the moving part of the x-stage (XM), and a moving part (YM). Figure 4.7 depicts the static part, and Figure 4.8 depicts the moving part.

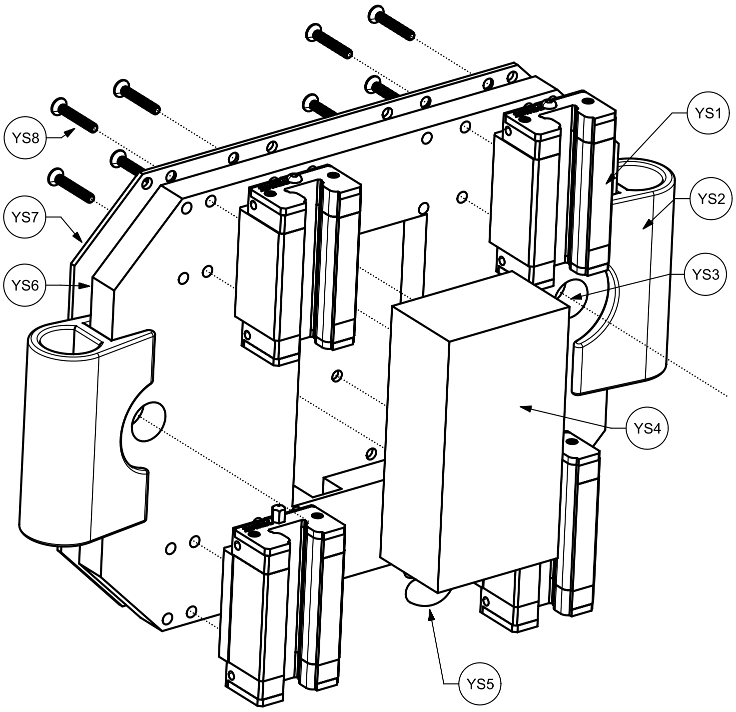

Figure 4.7: Exploded view of the front of the non-moving part of the y-stage (YS) with: linear carriage (YS1), bumper (YS2), weight-compensation mechanism mounting hole (YS3), coil-unit (YS4), cable of coil-unit (YS5), honeycomb panel (YS6), actuator mounting sheet (YS7), and machine screw (YS8).

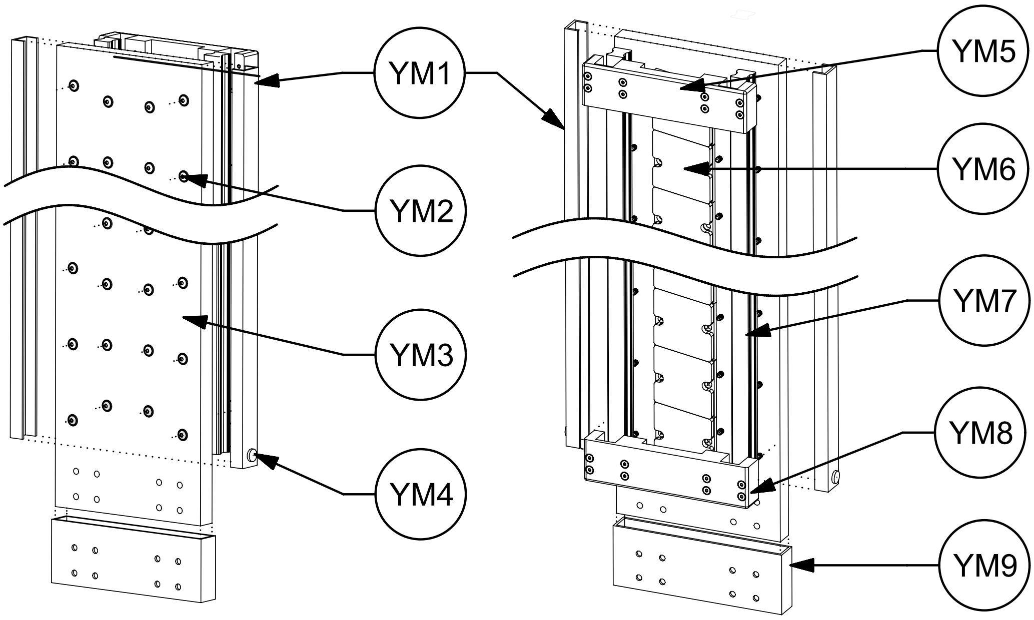

Figure 4.8: Exploded view of the front (left) and rear (right) of the moving part of the y-stage (YM) with: side u-profile (YM1), machine screw (YM2), honeycomb panel (YM3), spring mounting nipple (YM4), top-bumper (YM5), magnet-track (YM6), rail (YM7), bottom-bumper (YM8), and bottom profile (YM9).

Static part of y-stage (YS). The static part of the y-stage combines a structural basis of an aluminum honeycomb panel (YS8), and a sheet of aluminum (YS7) to mount the coil-unit (YS4) to the honeycomb panel. Using the honeycomb panel offers a high strength to weight ratio compared to using solid material [30].

Machine screws, (YS8), mount the carriages to guide the vertical rails of the y-stage, (YS1), to the honeycomb panel. Since aluminum honeycomb panels are manufactured according to tight tolerances, the carriages are placed on a sufficiently flat and rigid surface to prevent forces due to misalignment.

Figure 4.7 also shows two holes, (YS3), to be occupied by a weight compensation mechanism, and the left and right side of the y-stage are equipped with a rubber bumper, (YS2). The bumper protects the arms in case of a collision or an object getting trapped between the arms.

Moving part of y-stage (YM). As depicted in Figure 4.8, the moving part of the y-stage is built in a similar way to the static part. An aluminum sandwich panel, (YM3), functions as a basis to mount a magnet-track (YM6), rails (YM7), and two bumpers (YM5, YM8). The bumpers stop the linear rails from running out of the carriages. The hole pattern drilled to fixate the guides must be accurately machined such that there are no misalignment forces due to the guides not being parallel according to specifications.

Gluing, or bolting, a u-profile (YM1) on either side of the honeycomb panel prevents objects from damaging the core, and adds stiffness to the arm. Similarly, the bottom of the arm is equipped with an aluminum tube-like profile, (YM9), to create a mounting point for the end-effector. The profile also adds a layer of protection.

Weight-compensation mechanism. By designing the arms to be as lightweight as possible, the setup requires less powerful actuators. Both arms weigh 5 kg each, and an unsupported weight of

5 kg requires roughly 50 N to compensate for gravity. Only using an actuator to keep this weight in position would require a continuous force of 50 N to be applied by the actuators. Constantly applying this force, and thus the corresponding power consumption is inefficient.

Introducing a weight-compensating mechanism relieves the actuators when there is no vertical movement of the arms. The mechanism uses a constant-force spring to provide a constant force bias [31].

By equipping each arm with two constant-force springs (S0), which individually apply a force of 25 N in an upward direction. Figure 4.9 shows the actual mechanism. Positioning the springs in a back-to-back like configuration prevents unwanted torsional loads on the arm. Mounting the spring on a spool, (S2), with a bearing inside, (S3), allows unrolling the spring with little friction. The spool is mounted on a pipe, (S4), mounted to the non-moving part of the y-stage (YS3). By positioning the springs close to the arm, the arm prevents the springs from twisting or bending. As the spring unrolls, the outer-radius of the spring-roll decreases forming a gap between the spring and the arm. As the spring tends to move outward (towards the arm), this should not cause a problem. More information on the use of constant-force springs is found in [32].

4.2.3 Design of x-stage

Similar to the construction of the y-stage, the x-stage consists of two main assemblies: a non-moving part, (XS), and a moving part, (XM). The non-moving part is depicted in Figure 4.10. The moving part, (XM), to which the non-moving part of the y-stage is mounted, (YS), is depicted in Figure 4.11.

Static part of x-stage (XS). A panel of aluminum honeycomb, (XS1), forms the basis of the static part of the x-stage. The panel allows mounting the rails, (XS2), magnet-track, (XS3), and two u-profiles, (XS9), on a flat surface. Two aluminum end-plates (XS5) are mounted, with the use of screws (XS7), to either side of the x-stage. The end-plates also fix a center plate, (XS11), in line with the top of the u-profiles. The u-profiles, and the center plate, have a specific edge cut-out on the front-side to allow for a strip (XS12) to lay inside a shallow raceway. A tension mechanism, (XS6), fixates the strip on either side of the stage with the use of screws (XS8), and tensions it by

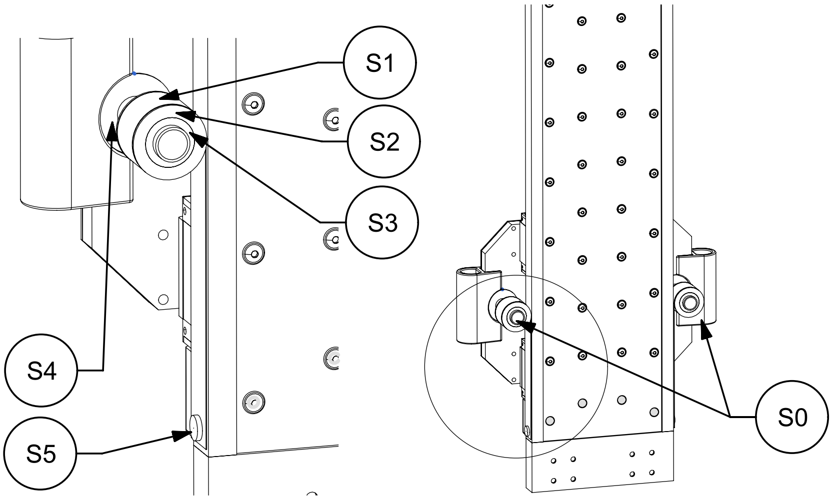

Figure 4.9: Constant-force spring mechanism (S) with: spring assembly (S0), spring (S1), spool (S2), bearing (S3), spool-mount (S4), and spring-mount (S5).

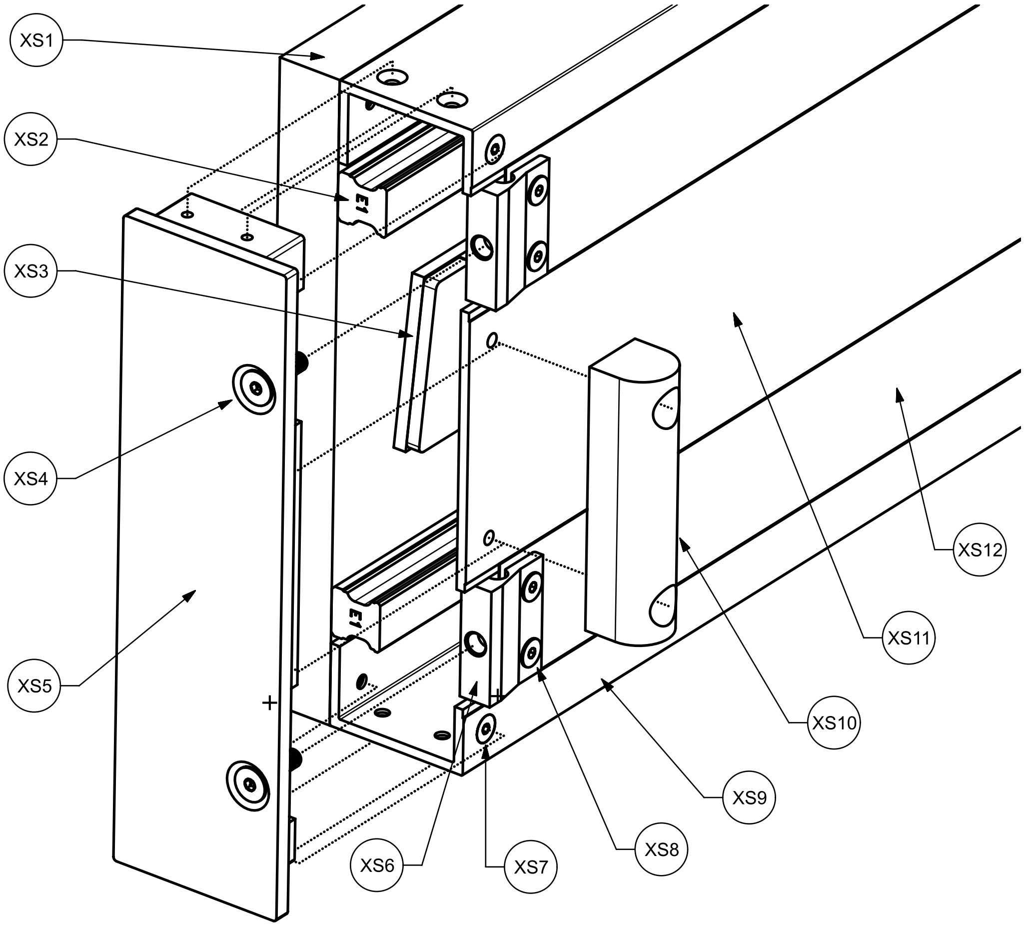

Figure 4.10: Partially exploded view of the fixed part of the horizontal stage (XS) with: honeycomb rear panel (XS1), rail (XS2), magnet track (XS3), strip tension adjustment screw (XS4), end-plate (XS5), strip-clamp (XS6), end-plate mounting screw (XS7), strip mounting screw (XS8), side profile (XS9), bumper (XS10), center plate (XS11), and strip (XS12).

twisting a screw (XS4), pulling the strip outward. Finally, to stop the moving-part of the x-stage when nearing end-of-stroke conditions, a bumper (XS10) is mounted to the end of the stage.

Moving part of x-stage (XM). The moving part of the x-stage uses a solid aluminum frame (XM3) to which four carriages (XM1) are mounted. Fixating the carriages implies five times over-constrained fixation per carriage as one carriage already fixates five degrees of freedom, requiring the intermediate part to be accurately machined to avoid parasitic forces due to misalignment.

A sheet of aluminum, (XM6), mounts the coil-unit, (XM2), to the frame (XM3). Two covers (XM5), placed on top of the aluminum frame, allow mounting the static part of the y-stage, and provide an entry point through which cables enter the static part of the x-stage (XM8). A strip moves through these covers, being lifted by a wedge (XM4) and pushed back down with an end-cap (XM7).

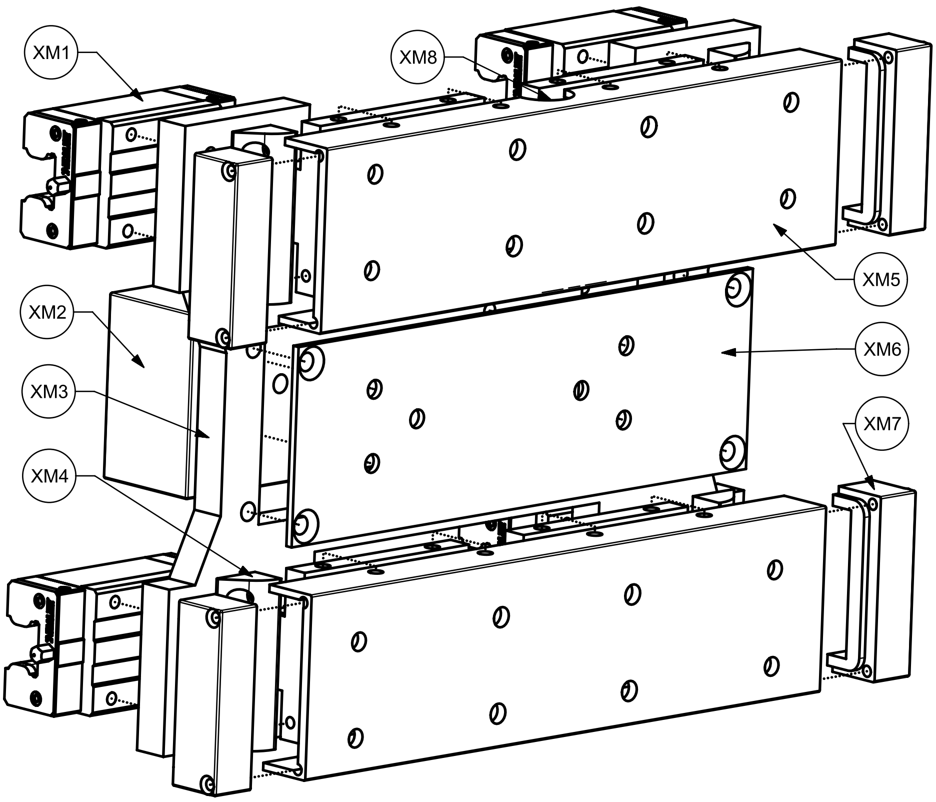

Figure 4.11: Overview of the moving part of the x-stage (XM), as seen from the front of the enclosure, with: linear carriage (XM1), coil-unit (XM2), frame (XM3), strip-lifting wedge (XM4), top-cover (XM5), coil-unit mounting plate (XM6), strip-pushing end-cap (XM7), and cable entry point (XM8).

4.2.4 Design of the end-effector

The end-effector forms an interface between the robot-arm and the environment. The interface allows sophisticated object manipulation and protects the arms. The design of the end-effector must comprehend compliance and damping, and offer sufficient friction.

Maximum allowable impact force. Appendix B discusses the maximum transfer ratio between forces exerted to the end-effector, and forces exerted on the linear guides. It shows that that the maximum transfer ratio is equal to 1:2.6, 1 N exerted on the end-effector resulting in 2.6 N exerted on the guides. Appendix C discusses the guides selected for the setup. The listed maximum static load-rating of the selected guides is approximately equal to 20 kN. Requiring the end-effector, having a transfer ratio of 1:2.6, to be designed to limit the peak-force to a maximum of 7.7 kN. As discussed in Section 4.1.1, a maximum impact velocity of 2 m/s, with a moving mass of 10 kg, requires an impact penetration of 5.4 mm. A maximum stiffness of the end-effector of 1370 N/mm meets this requirement. Note that the arms of the robot do also have a finite stiffness, which is not taken into account here; this is conservative but creates a safety margin.

Figure 4.12 depicts an exploded view of the end-effector, showing two brackets (EE2), fixed to the bottom of the y-stage using screws (EE1). The brackets fixate the tip through an intermediate mount (EE3). The tip consists of a support-ring (EE4) and a rubber tip (EE5), both mounted to the intermediate part through a mounting bolt (EE6).

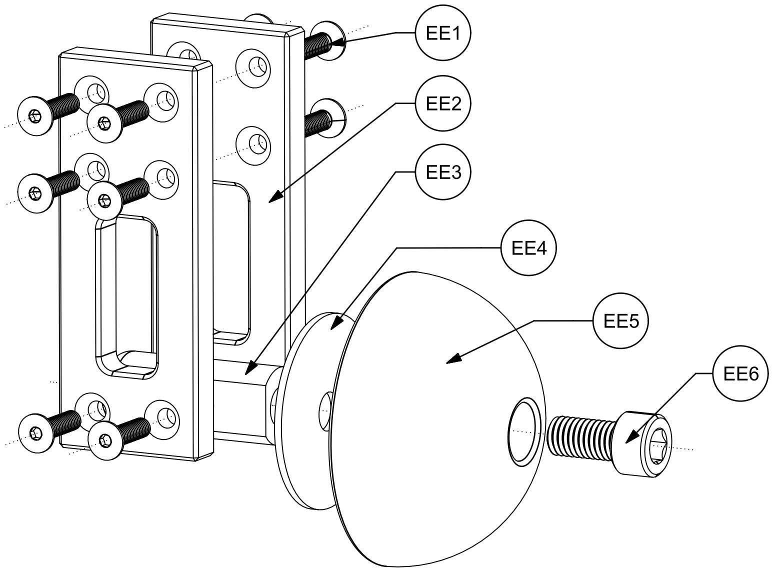

Figure 4.12: Exploded view of end-effector (EE) with: machine screw (EE1), bracket (EE2), tip-mount (EE3), support-ring (EE4), tip (EE5), and mounting bolt (EE6).

Design of bracket. The end-effector bracket must reduce impact forces with the use of compliance. The compliance must be high enough to protect the arm from impact velocities of up to 2 m/s. A way to achieve this is to design the bracket and verify the stiffness through a FEM model. Although this does provide proper insight into the stiffness of the end-effector, it is time-consuming to iterate through this process. Hence, the end-effector is first analyzed through simple analysis, and once the design meets the specifications according to these simple equations, the design is confirmed using a finite element method (FEM) analysis. Figure 4.13 depicts a model of the end-effector bracket used for the analysis.

The relevant stiffness of this design is computed through [33]:

$$k_{xx} = 3\frac{YJ}{l_b^3}, \text{ and} \tag{4.8}$$

$$J = 2\frac{d_b w_b^3}{12}. \tag{4.9}$$

In which Y is the Young's Modulus, J is the second moment of inertia with w_b and d_b being the width and height of the cross-section of the parallel beams, and l_b is the length of the two beams. Figure 4.12 shows a design, established through iteration, with $Y = 3 \times 10^9$ MPa, $l_b = 4 \times 10^{-2}$ m, $d_b = 10 \times 10^{-3}$ m and $w_b = 12 \times 10^{-3}$ m. The relevant stiffness of the design depicted in this Figure 4.12 being $k_{xx} = 5.4 \times 10^2$ N/mm. Implemented with two of these brackets in parallel, makes the total stiffness $k_{tot} = 1.1 \times 10^6$ N/m.

The material used in this bracket is nylon; a lightweight material with average strength, that allows printing using a conventional 3D printer [34]. The design of the bracket entirely depends on the used material and the method of fabrication. Using other materials, for example, due to the availability of materials, requires adopting the design.

A FEM model is used to verify the design. The details on setting up this model are discussed in Appendix E. Since horizontal collisions with end-effector cause the most significant peak-forces, only this direction of deformation is analyzed. According to the FEM analysis, the stiffness of the

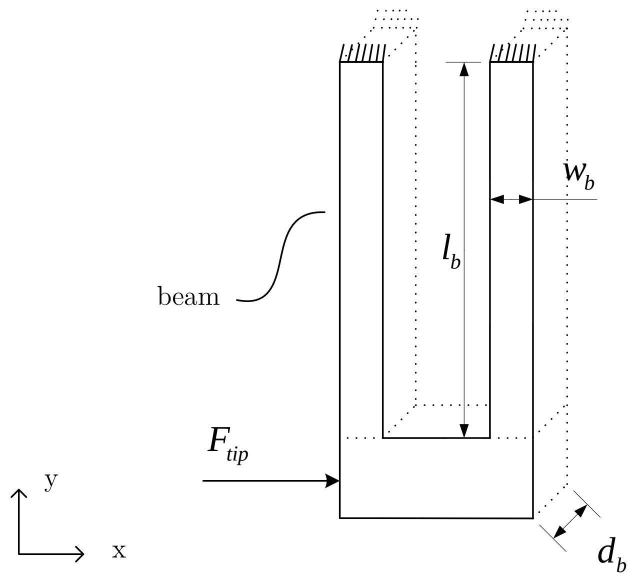

Figure 4.13: Model of the bracket with: two beams of width w_b, depth d_b and length l_b, and force F_{tip} applied to the end of both beams.

end-effector in the horizontal direction is equal to 0.7×10^6 N/m, making the total stiffness with two brackets in parallel equal to 1.4×10^6 N/m. This stiffness exceeds the maximum allowed stiffness but would be suitable being combined with a rubber tip.

Design of dampening tip. The tip of the end-effector, attached to the designed bracket, increases the dampening of the end-effector compared to the sole use of a plastic bracket. A suggested option for the material of the tip is Sorbothane, a rubber-like material that offers both damping and compliance [27]

A screw fixes the tip, through an intermediate part, to the brackets of the end-effector. An aluminum ring prevents the tip from getting damaged due to the intermediate part cutting into the rubber. Note that this combination is designed in such a way to allow quick and straightforward replacement of the tip or the whole end-effector mechanism.

4.2.5 Design of enclosure

Figure 4.14 depicts a sketch of the enclosure. The enclosure allows a clear view for spectators by mainly using transparent panels, (E1, E5, E6), manufactured from Poly(methyl methacrylate) (PMMA). Considering glass as unsafe for a test-bed, PMMA and Polycarbonate (PC) are common materials for enclosures, PMMA is preferred based on stiffness, scratch resistance, and light transmissibility [35][36]. The thickness of the panels is based on the required stiffness at the center of the panels.

The horizontal stage is mounted flat with the rear plane and kept in position with two main legs (E4), two rear legs (E8), and two front legs (E9). Honeycomb sandwich panels make sure that the legs are stiff and lightweight. By fixing the setup to a table, and fixing the table to the floor, it does not fall over.

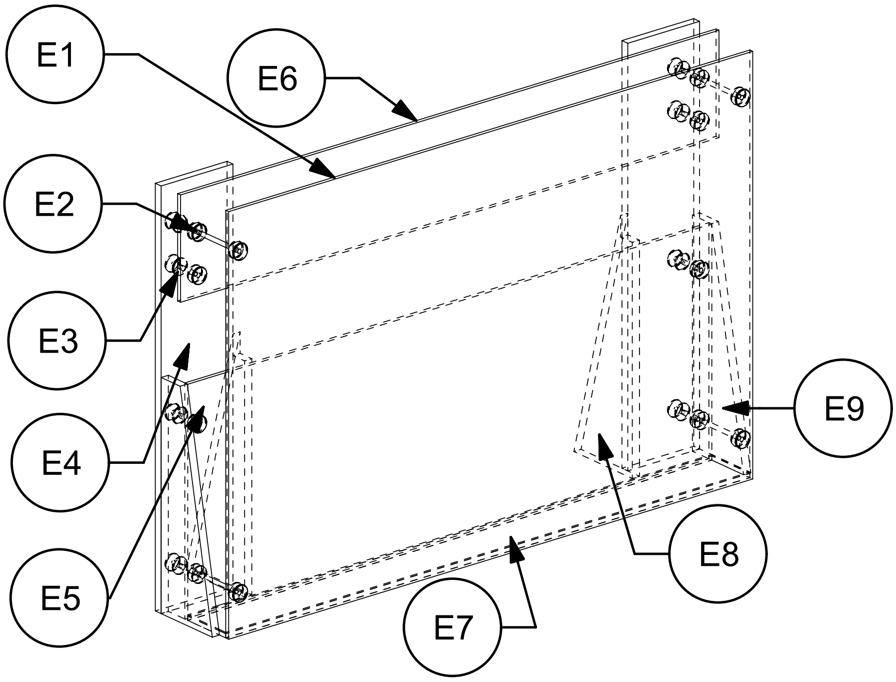

Figure 4.14: Overview of enclosure (E) with: front-panel (E1), double-spacer (E2), single-spacer (E3), main-leg (E4), rear-bottom panel (E5), rear-top panel (E6), enclosure floor (E7), rear-leg (E8), and front-leg (E9).

Spacers (E2, E3) keep the panels in place and keep the panels spaced at a certain distance. Clamping the panel with the spacers constrains each panel at four points. By adding soft foam between the spacers and the panel, the panel is allowed thermal expansion without deformation.

The floor material of the setup (E7) can be varied to allow for experimenting with different floor types.

Panel thickness. To compute the required thickness of the panels in the enclosure, a plate clamped at four sides is considered, shown in Figure 4.15. A force F_c is applied to the center of the plate, at center position p_c. The plate has a height of h_p, a width of w_p, and a thickness of s. The goal here is to compute the thickness of the panel using a maximum desired deflection for a given force. The deflection of the panel is computed according to [33]:

$$d_p = \frac{\beta F_c h_p^2}{Y s^3}, \tag{4.10}$$

in which d_p relates to the deformation of the panel depending on the ratio between w_p and h_p, through coefficient β, a force F_c, minor length h_p, Young's modulus Y and panel thickness s. The thickness of the panel is determined according to:

$$s = \left(\frac{\beta F_c h_p^2}{Y d_p}\right)^{\frac{1}{3}} = \left(\frac{0.0706 \cdot F_c \cdot 1^2}{3e9 \cdot 0.001}\right)^{\frac{1}{3}}. \tag{4.11}$$

Equation (4.11) shows that the thickness of the panel can be linked to the force applied to the center of the panel, resulting in a center deflection. The panel thickness is chosen such that a force of $F_c = 10\,\mathrm{N}$, results in a displacement of $d_p = 1\,\mathrm{mm}$. Requiring the panel to be at least $s = 6\,\mathrm{mm}$ thick.

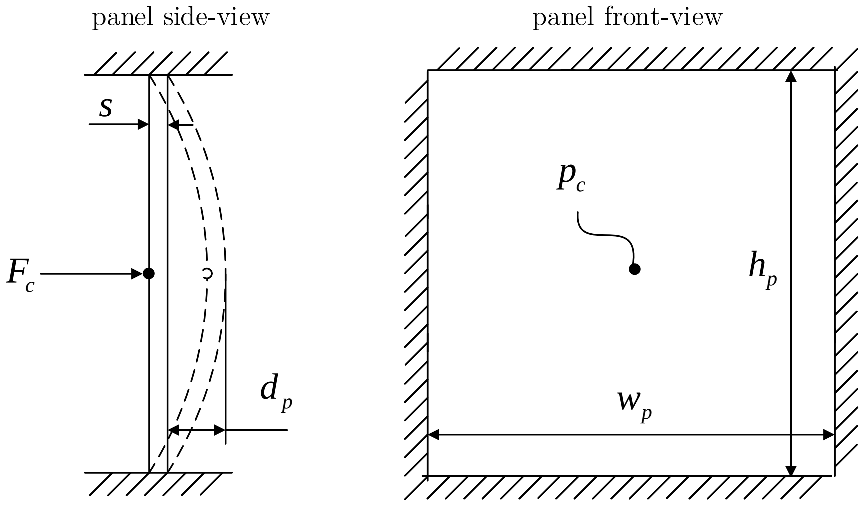

Figure 4.15: Model of a w_p by h_p plate, with thickness s, clamped at four sides, loaded at center p_c, with a load of F_c, leading to a deflection of d_p.

4.3 Discussion of design

This chapter translated the Cartesian planar manipulator into a design that meets the criteria presented in Chapter 2. Table 4.1 shows the properties and dimensions of the test-setup.

Although some parts of the design already have a significant amount of detail, the design is not ready for manufacturing. The detailed design should start with the selection of components in line with the suggested dimensions and properties. The x- and y-stage are designed after this selection. Using the properties of these stages allows the design of a supporting structure that can withstand a maximum acceleration of the x- and y-stage. Finally, the front- and rear-panels are added to the design with a suitable fixation.

Table 4.1: Overview of dimensions and properties of the designed system.

Parameter	**Value**	**Unit**	**Description**
Robot workspace width	1.06	m	Workspace width allowing bi-manual manipulation
Robot workspace height	0.4	m	Workspace height allowing bi-manual manipulation
Object workspace width	1.4	m	Workspace width of the object
Object workspace height	0.98	m	Workspace height of the object
Depth of workspace	0.13	m	Distance between front- and rear-plate
Footprint width	1.5	m	Total footprint width of the setup
Footprint height	1.0	m	Total footprint height of the setup
Footprint depth	0.37	m	Total footprint depth of the setup
Mass y-stage	4.8	kg	Moving mass of the y-stage
Mass x-stage	4.7	kg	Moving mass of the x-stage (y-stage excluded)
Mass motion system	21	kg	Total mass static and moving mass of the x- and y-stage
Mass setup	46	kg	Total mass of the setup
Ultimate force y-stage	120	N	Maximum force of actuator for the y-stage
Ultimate force x-stage	240	N	Maximum force of actuator for the x-stage
Max acceleration y-stage	25	m/s^2	Maximum acceleration y-stage using ultimate force and no object
Max acceleration x-stage	25	m/s^2	Maximum acceleration x-stage using ultimate force and no object
Max velocity y-stage	12	m/s	Maximum velocity of the y-stage
Max velocity x-stage	12	m/s	Maximum velocity of the x-stage

Chapter 5

Simulation-based validation of the design

Chapter 4 addressed the test-bed design. This chapter validates the design with simulations. The simulations must validate if the designed test-bed allows the execution of tasks involving throwing, catching, and grabbing objects. The design is considered successful if simulations show the proposed tasks in a realistic scenario—a scenario, based on realistic properties for mass, geometry, and actuation. The setup is evaluated using the model developed in Chapter 4 in conjunction with established control algorithms to demonstrate the scenarios addressed in Chapter 2.

5.1 Tools and framework

Selecting a tool for simulating a particular system depends on the designer's needs. Such needs focus on the application of that particular system, and the expected insights gained from simulating the system.

In this case, simulating the functioning of the test-bed must provide information on the ability to perform tasks involving impacts. This ability requires the tool to handle simultaneous non-smooth contact establishments. The tool must also allow the implementation of control-algorithms, have computer aided design (CAD) model import capabilities, and allow real-time simulation. Algoryx Momentum meets these different requirements [37]. The tool is equipped with a Python engine to allow simulating tasks comprising of varying motion trajectories, with trajectory changes based specific conditions that vary for each simulation.

The goal is to investigate the combination of geometry, actuators, and frictional properties, in the ability to demonstrate the desired tasks listed in Chapter 2.

5.1.1 Model setup

Setting up the simulation model involves: importing a CAD model into Dynamics for Spaceclaim, assigning physical properties, and adjusting the simulation settings. This process is performed according to the workflow in Figure 5.1, in addition, Appendix F describes the workflow in detail. Figure 5.2 shows the different rigid-body groups in different colors.

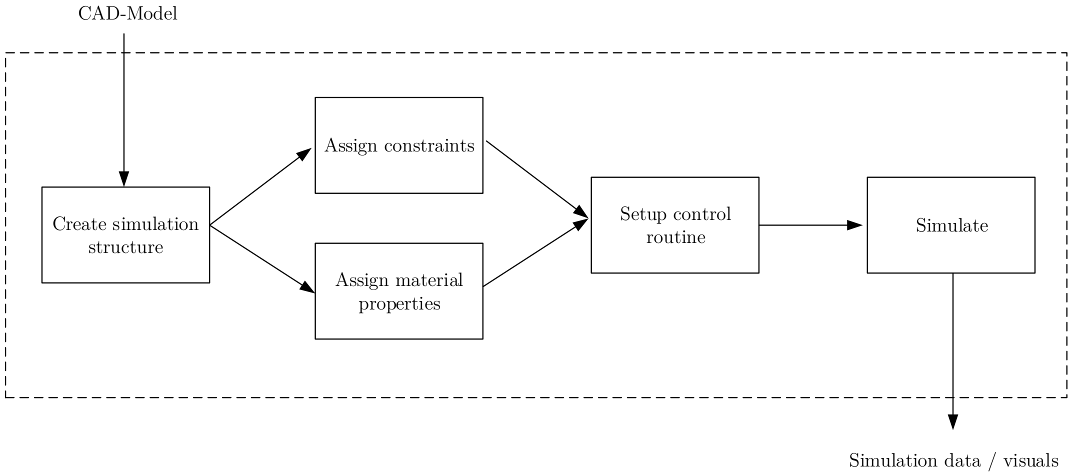

Figure 5.1: Workflow used for setting-up multi-body simulation in Algoryx Momentum.

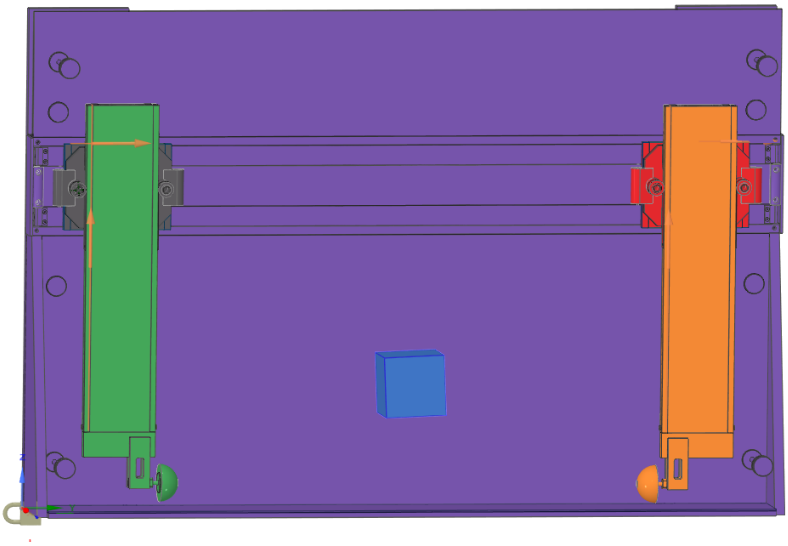

Figure 5.2: Multi-body model as prepared in Algoryx Momentum, showing five different rigid-bodies, of which most are grouped components.

5.2 Control of setup

Verifying the functioning of this setup in a simulation involves the development of different control routines. The following sections first discuss the developed routines, followed by their physical realizability, and ending with a discussion on the outcomes of the simulations.

5.2.1 Impact-aware manipulation

If the dynamics of a control-system vary as part of a task, a single reference trajectory is not necessarily functional. Reference spreading [7][8] adopts a reference trajectory for each part of the task. Each reference trajectory is expanded by forward- and backward integration of the dynamics of each component, overlapping the preceding and subsequent trajectories. Based on state input, exploiting non-smooth contacts, the active reference trajectory switches between these different parts, and the corresponding reference trajectory. The focus for this setup is to demonstrate that the tasks discussed in Chapter 2 are realistic. Therefore, this report does not introduce the reference spreading technique. Using the following approach for identification and actuation inspired by the technique:

Identification. By using the robot's velocity data, impacts are identified by detecting velocity jumps. If an expected impact occurs, contact is assumed. A detailed explanation is found in Section 5.2.2.

Actuation. Depending on the type of task, different steps can follow impact detection. If the aim is to create contact with both arms, both arms approach an object along a specified trajectory that intersects with the object. Only when both arms are in contact with the object, the robot continues its task with another trajectory. Consequently, if we detect only one impact, but expect two impacts, the initial trajectories remain the same.

5.2.2 Detection of impact

Reacting to an impact requires detecting the impact. Due to the instantaneous nature of the impact, detection happens after the impact has occurred. The time it takes to detect an impact depends on the source of measurement, and the equipment used to control the setup. Some sensors can provide information at high frequencies, for example, piezoelectric force transducers, other sensors provide information at a much lower frequency, for example, a camera.

Impacts in Algoryx Momentum. Modeling of contact is possible in different ways: by taking into account both stiffness and damping properties of the colliding bodies, as well as the contact stiffness and damping properties; by only considering the stiffness and damping properties of the colliding bodies, and modeling the contact with an inelastic algebraic relation to compute post-impact velocities; or by modeling rigid-bodies with an inelastic algebraic relation to model the contact [38]. In the case of a rigid object impacting a wall, following Newton, the coefficient of restitution determines the post-impact velocity with:

$$v_o = \gamma v_i, \tag{5.1}$$

in which: v_o, is the post-impact velocity, v_i, is the pre-impact velocity and γ, is the coefficient of restitution. Algoryx Momentum incorporates such a method. It allows for stable and real-time simulation and allows robust simulation even with impacts occurring [39].

Detection of impact in Algoryx Momentum. Velocity data is used to detect impacts based on rapid state changes. This process is explained using Figure 5.3.

Provided time- and velocity-data of the previous Z time-steps, (t_{-z}, v_{-z}), with $z = 1, ..., Z$. Defining polynomial of degree n with:

$$P(t) = \alpha_n t^n + \alpha_{n-1} t^{n-1} + \cdots + \alpha_2 t^2 + \alpha_1 t + \alpha_0, \tag{5.2}$$

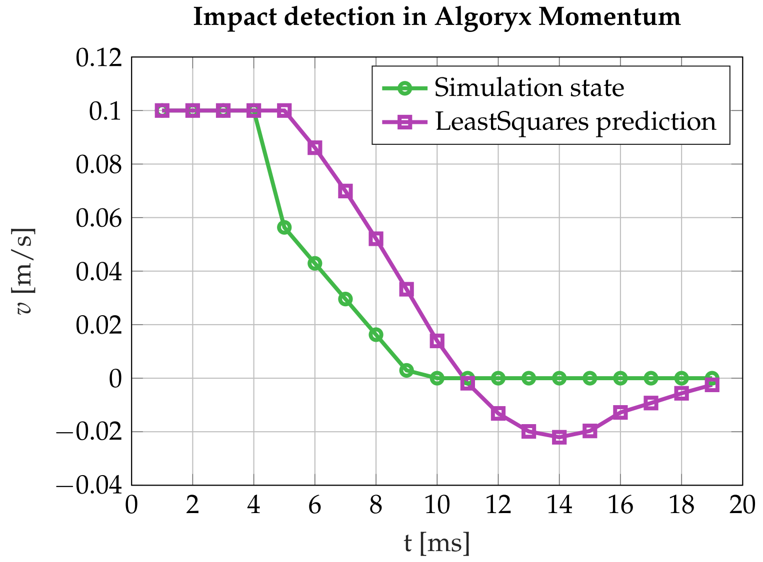

Figure 5.3: Detection of impact in software package Algoryx Momentum using a least-squares prediction, showing a simulated and a predicted velocity for a selection of time-steps.

and finding coefficients $\alpha_0, ..., \alpha_n$, by minimizing the squared residual error:

$$\min_{\alpha_n} E = \sum_{z=1}^{Z} \left(v_{-z} - (\alpha_0 + \alpha_1 t_{-z} + \cdots + \alpha_n t^n{}_{-z})\right)^2, \tag{5.3}$$

to predict the velocity for the current time-step:

$$v_0 = P(t_0). \tag{5.4}$$

The velocity prediction, v_0, is compared to the current value of the velocity. If the predicted velocity differs from the current velocity by a percentage higher than percentage R, an impact is assumed. The impact indicates an established contact.

$$v_{meas} = \begin{cases} > v_0(1+R), & \text{impact} \\ < v_0(1-R), & \text{impact} \\ \text{otherwise}, & \text{no impact} \end{cases} \tag{5.5}$$

The implementation of this routine in pseudocode is discussed in Appendix F.

5.2.3 Routines

The following sections describe the routines involved in simulating throwing and catching of objects, and grabbing and placing of objects.

Throw and catch. Consider the routine for throwing and catching an object in Figure 5.4. Note that for each arm, the reference for each motor is either velocity-based or force-based. The reference values for this task are displayed in Table 5.4.

The arms approach the object with a horizontal velocity of $v_{approach}$, (0). Detecting simultaneous impact as both arms establish contact with the object starts the throwing stage, (1). The arms

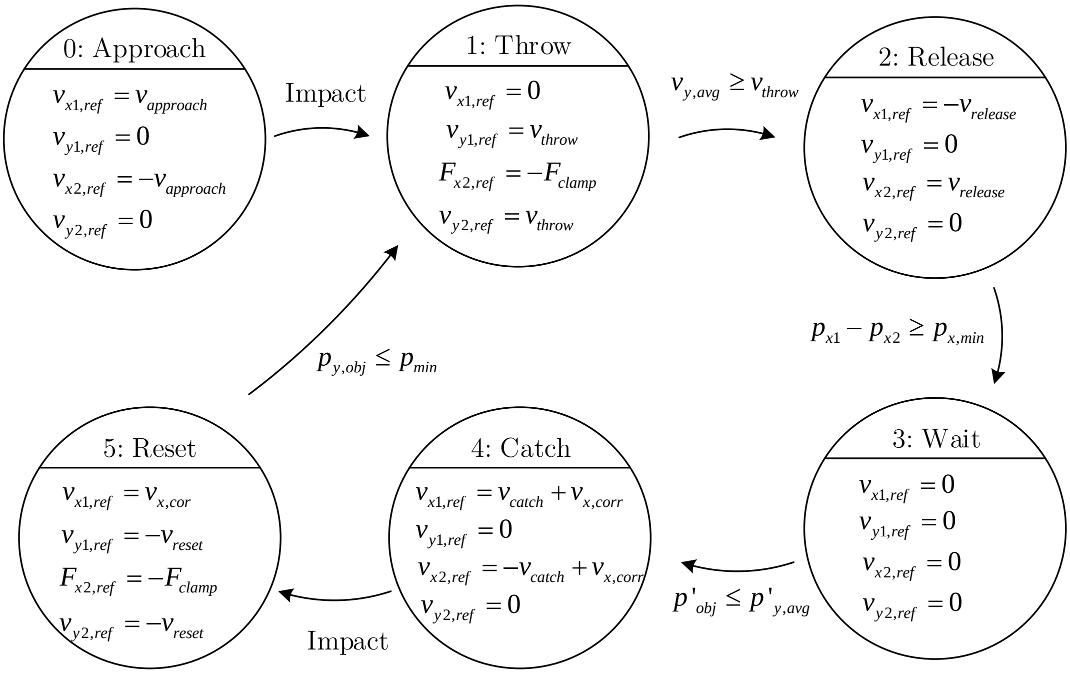

Figure 5.4: Routine for throwing and catching objects, with different sub-routines for which the parameter values and description are shown in Table 5.1, as implemented in Algoryx Momentum.

Table 5.1: Parameters used in routine of catching and throwing an object.

Parameter	Value	Unit	Description
$v_{approach}$	1	m/s	Horizontal approaching velocity
v_{throw}	3.2	m/s	Vertical throwing velocity
F_{clamp}	40	N	Horizontal clamping force
$v_{release}$	1	m/s	Horizontal release velocity
$p_{x,min}$	0.4	m	Minimum horizontal distance
v_{catch}	1	m/s	Horizontal catching velocity
v_{reset}	1	m/s	Vertical reset velocity

accelerate the object to a vertical velocity of v_{throw} while clamping the object with a clamping force of F_{clamp}. The clamping force prevents the object from slipping. As the arms reach a velocity, $v_{y,avg}$, higher than the throwing velocity, v_{throw}, the arms release the object, (2). The arms release the object by moving both end-effectors in opposite x-direction with $v_{release}$, while simultaneously reducing velocity in the y-direction to zero. The arms move apart to an inter distance of $p_{x,min}$, to stop and wait until the object returns, (3). With the object in reach, both arms move towards the object with a velocity of $v_{catch} + v_{x,corr}$, and catch the object, (4). The sub-routine determining whether an object is in reach, and how to determine the correction velocity, $v_{x,corr}$, is discussed in the following paragraph. The arms clamp the object with F_{clamp}, and return to the initial position, (5), with v_{reset} in the y-direction, and $v_{x,cor}$ in the x-direction. Once back in the initial position, the task repeats itself.

Grab and Place. Figure 5.5 explains the task of grabbing and placing. The routine uses both velocity- and force-based references. The parameter values are displayed in Table A.3.

The arms approach the object with a horizontal velocity of $v_{approach}$, and a vertical velocity of v_{lift}, (1). As the arms establish contact with the object, identified through simultaneous impact, the y-stage maintains a velocity reference of v_{lift}. At the same time, the x-stage accelerates to a velocity of $v_{transport}$ with a clamping force of F_{clamp}, (2). As the object reaches a height of $p_{y,min}$, vertical velocity is reduced to zero, while the x-stage maintains a velocity of $v_{transport}$, (3). Once the object surpasses $p_{x,min}$, the arms start to descend (4) with a velocity of $-v_{lift}$ while maintaining horizontal Momentum. The arms hit the ground, and release the object with a horizontal velocity of $v_{release}$, (5).

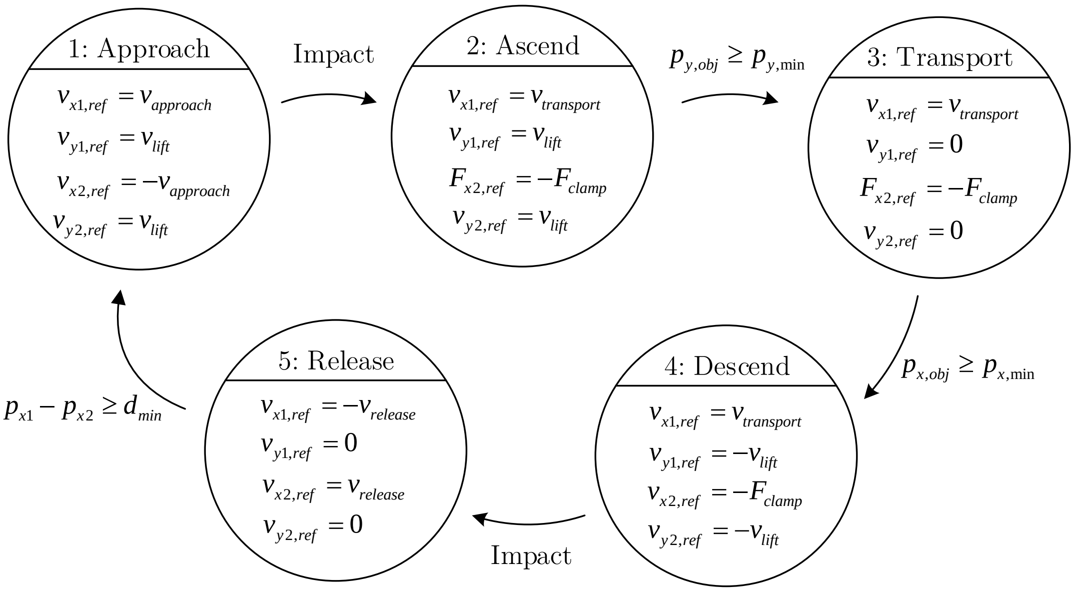

Figure 5.5: Routine for grabbing and placing of objects, with different sub-routines for which the parameter values and description are shown in Table A.3, as implemented in Algoryx Momentum.

Table 5.2: Parameters used in routine of grabbing and placing an object.

Parameter	Value	Unit	Description
$v_{approach}$	1	m/s	Horizontal approaching velocity
v_{lift}	1	m/s	Vertical ascending velocity
$v_{transport}$	1.5	m/s	horizontal transport velocity
F_{clamp}	40	N	Horizontal clamping force
$p_{y,min}$	0.3	m	Minimum height
$v_{release}$	0.5	m/s	Horizontal release velocity
$p_{x,min}$	0.65	m	Minimum covered horizontal distance
d_{min}	0.2	m	Minimum horizontal distance

5.3 Physical realization

Detection of impact requires information on either motion or force of the robot. Acquiring this information is possible through external sensors such as encoders, force sensors, or cameras. The current applied by the actuator could also provide crude information on applied forces by the robot. Choosing the proper source of information to detect impact should be based on accuracy, sampling frequency, and measurable quantity. Preferably, detection occurs as fast as possible.

The simulations that should validate the feasibility of the setup show that it is potentially possible to execute the foreseen tasks in a physical realization. Since there has been no discussion on sensors, and the simulation does use state information, the use of state information is motivated as to which sensor would provide this information. The simulation uses information on the position of the arms and object, and the force applied to the object.

Position of arms. The position of the arms determines where the end-effectors are concerning the object. A hall effect sensor could be a valid solution to measure the position of the arms. It offers an absolute accuracy of 100 µm [16], which is suitable for this application. An added advantage is that this hall-sensor does not require an extra ruler for position measurement as it measures the magnetic field of the magnet track.

Position of object. The robot has to know the position of the object. Measuring the position of the object is possible through the use of a camera [13]. The camera would be positioned in front of or behind the setup. Although the refresh rate of the object position due to visual object recognition might be limited, a rough position should already be suitable.

Force estimation. Since the robot is designed to use direct-drive motors, the current supplied to the motors provides an estimation of the force applied to the object. Although the bearings do cause friction, which does limit the accuracy of the measurement, the estimation should provide an estimate accurate enough for the use of the information. Estimation in the range of several Newton should be fine considering its use to track a clamping force reference.

5.4 Results of simulations

The following sections discuss the results of implementing the routines discussed in Section 5.2. The routines help to evaluate the functionality of the test-bed.

5.4.1 Simulation throwing and catching object

Figure 5.6 shows the task of throwing and catching objects. For six time-stamps, Figure 5.7 depicts the state of the system at that time-stamp. The motion profiles in Figure 5.6 shows the motion of the arms of the robot during a simulation. For both arms, the left graph depicts the state info of the x-stage, and the right graph depicts the state of the y-stage. The plots also show the position, velocity, and acceleration of the object.

In the simulations, the arms throw an object with a weight of 1 kg, to a height of 0.7 m. Selecting a constant-force spring providing 50 N of upward lift, allows the design to accelerate the object to a velocity of 3.2 m/s, but the stroke of the arm is to short to decelerate the arm before hitting the end-of-stroke. For this reason, it was not possible to achieve the required height of 0.8 m. For the

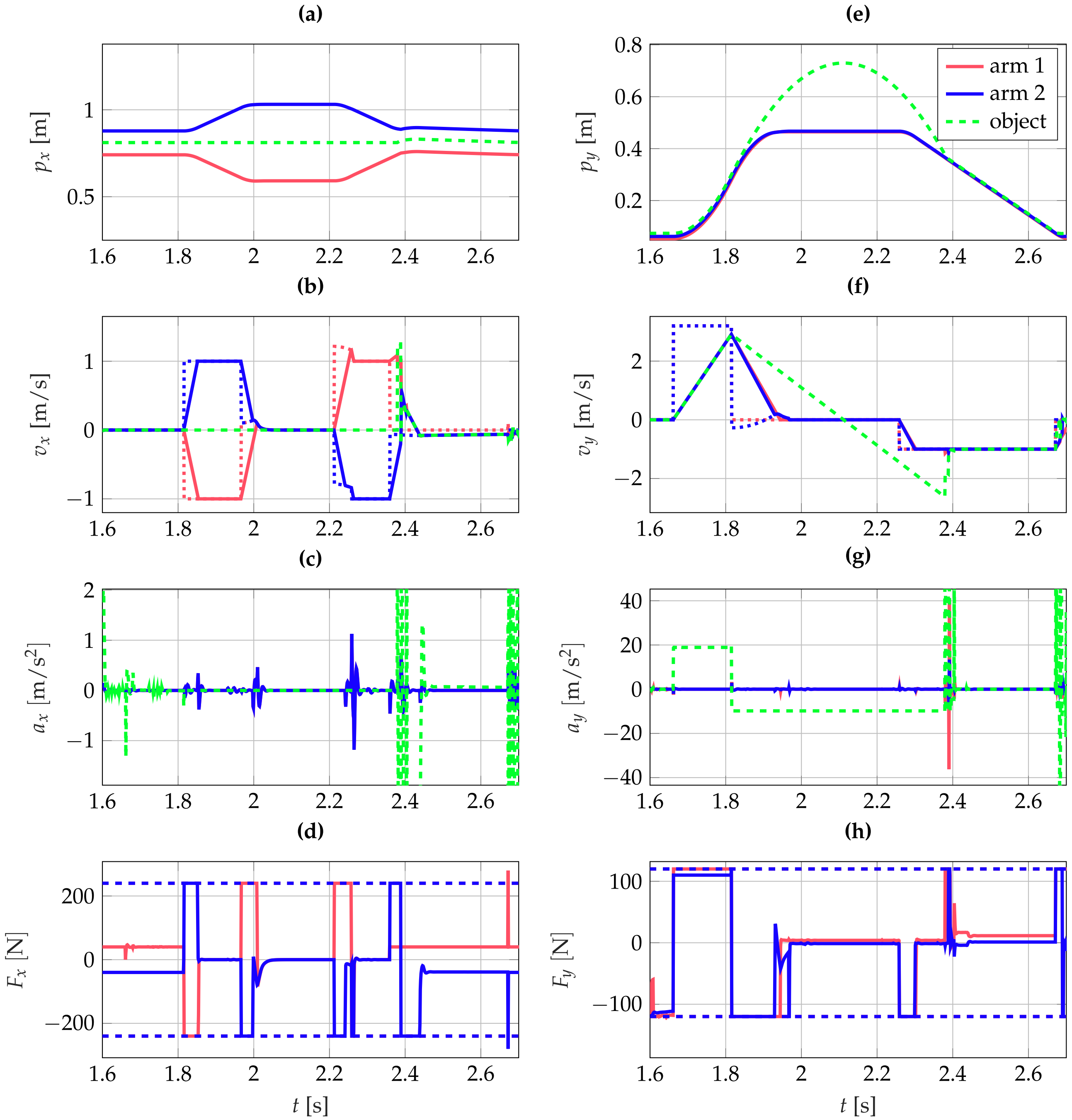

Figure 5.6: The trajectory for throwing and catching, as tracked during simulation, with: the state of the object, x- (left), and y-stage (right). Showing position, velocity, velocity reference (dotted), acceleration, force, and force limit (dotted).

realization of the setup, it may be better to increase the force available for the y-stage actuators to 160 N instead of 120 N as chosen in Appendix D. The x-stage provides a sufficient amount of force to prevent the object from slipping during acceleration and deceleration.

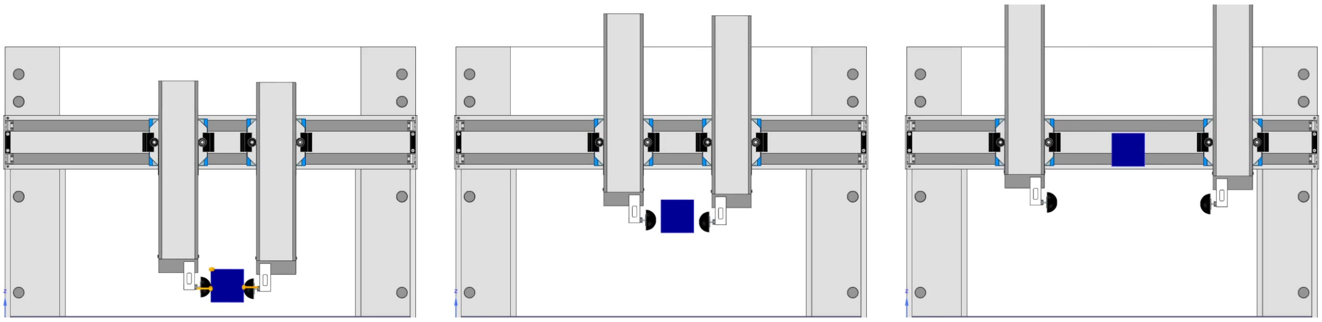

(a) $t = 1.7$s **(b)** $t = 1.85$s **(c)** $t = 2.1$s

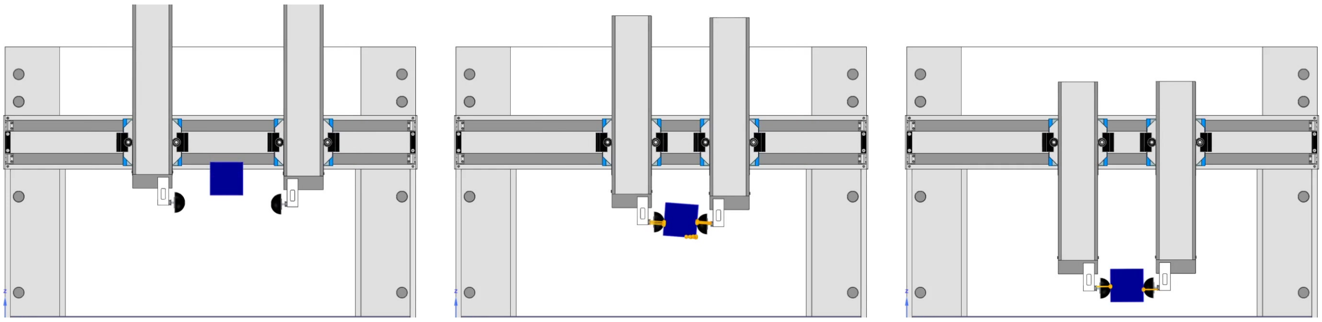

(d) $t = 2.3$s **(e)** $t = 2.4$s **(f)** $t = 2.6$s

Figure 5.7: Depicted state of the system for different time-steps in correspondence with Figure 5.6 demonstrating throwing and catching of an object.

5.4.2 Simulation grabbing and placing object

Figure 5.8 shows the motion trajectory for the task of grabbing and placing an object. Again, for six timestamps, the corresponding state of the system during simulation is depicted in Figure 5.8.

The simulations show that the arms effectively grab the object from its position, and the object abruptly accelerates adjusting to the horizontal velocity of the left arm. Once both arms are in contact, they transport the object to the other side of the enclosure, showing that the cooperation between the two arms, where one arm tracks a motion trajectory, and the other acts as impedance, is a viable control strategy. At last, the simulations show that the contact establishment of the second arm, during grabbing of the object, slows down the first arm to zero velocity. The full stop of the first arm in grabbing objects requires improvement by, for example, moving the second arm before impact has occurred rather than waiting for the impact to happen and then act on it.

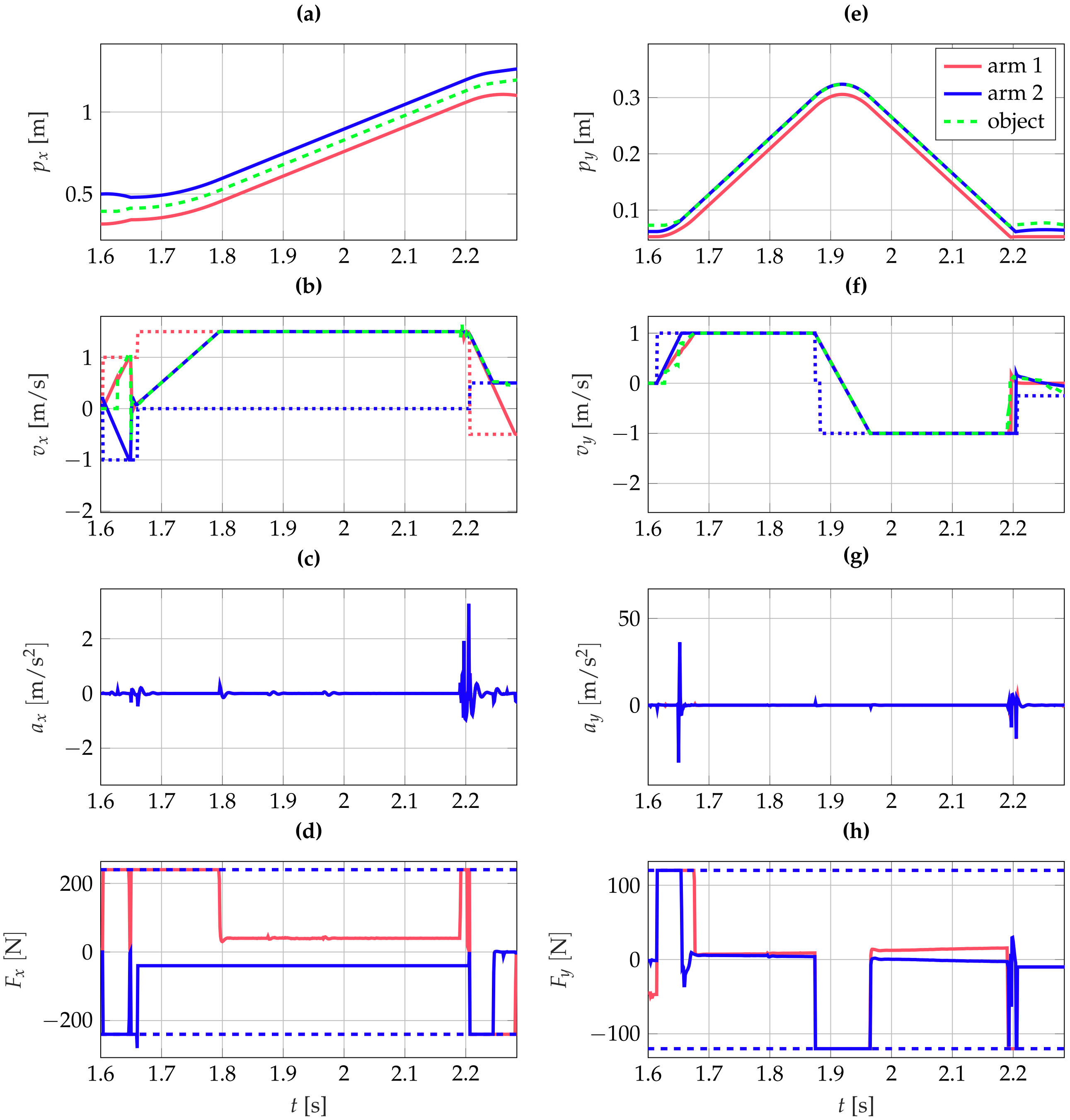

Figure 5.8: The trajectory for grabbing and placing, as tracked during simulation, with: the state of the object, x- (left), and y-stage (right). Showing position, velocity, velocity reference (dotted), acceleration, force, and force limit (dotted).

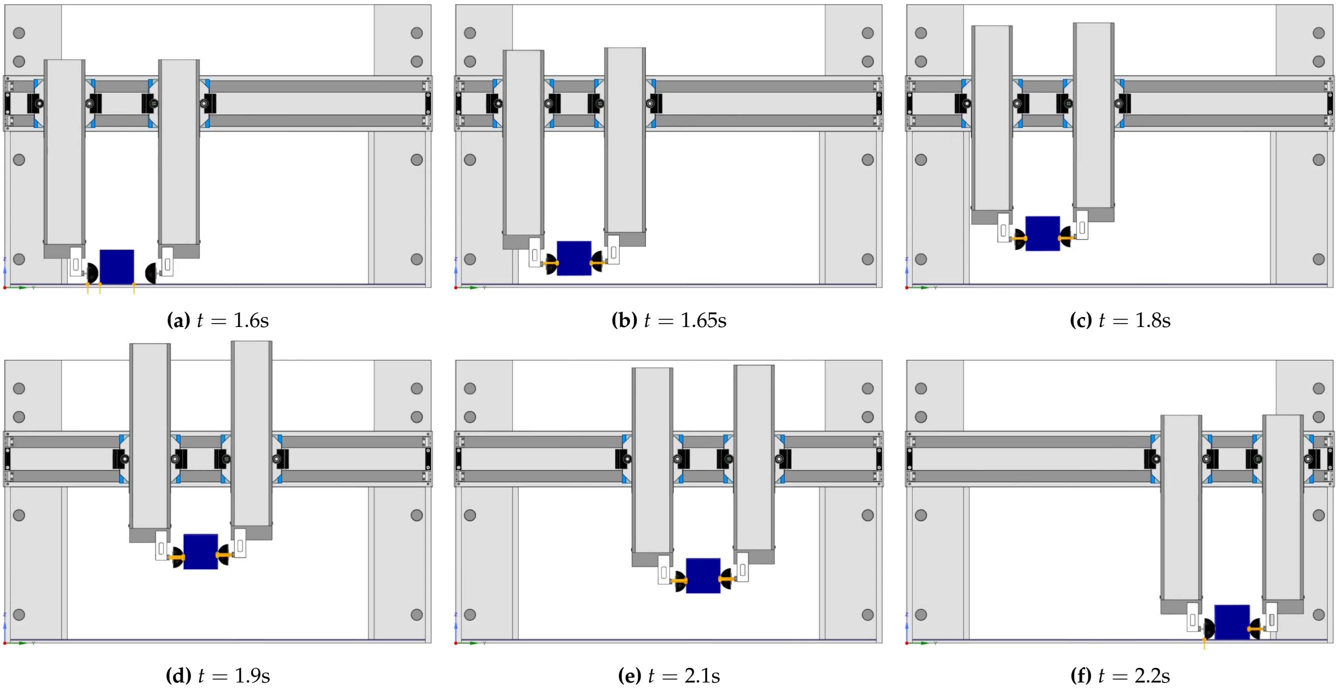

(a) $t = 1.6$s **(b)** $t = 1.65$s **(c)** $t = 1.8$s

(d) $t = 1.9$s **(e)** $t = 2.1$s **(f)** $t = 2.2$s

Figure 5.9: Depicted state of the system for different timesteps in correspondence with Figure 5.8 demonstrating grabbing and placing of an object.

5.5 Simulation outcomes

This chapter evaluated the functionality of the test-bed in the ability to perform the tasks, as discussed in Chapter 2. It shows that the setup has the functionality to throw, catch, and grab objects. However, it also showed some points for improvement:

- The actuators of the y-stage were not powerful enough to accelerate the arms, and slow them down, before hitting an end-stop. The advice is to increase the actuators-force, from a force of 120 N to a force of 160 N.
- In grabbing objects, the simulations show that both arms come to a standstill before moving the object to the destination location. This full stop of both arms is something that shows that the simple routines work, but are not necessarily efficient.
- The simulations show that the tasks are quite aggressive, executing long strokes in short time-frames, requiring evaluation of the design of the supporting frame on the ability to handle these movements. It is also debatable if the requirements may be too strict.

Chapter 6

Conclusion and recommendations

This dissertation aimed to develop a test-bed to evaluate impact-aware manipulation, a test-bed that allows throwing, catching, and grabbing of objects. The setup must be resilient to the effects of mechanical impacts occurring during the operation of the setup. Finally, the thesis aimed to validate the mechanical design of the setup through a multi-body simulation. Herein, validating the functionality of the setup through the use of simple control routines.

6.1 Conclusion

In this study, different concepts were considered for demonstrating impact-aware manipulation. The thesis first defined high-level requirements, which were followed by different tasks that would have to be performed with the setup. Translating the tasks into quantitive requirements allowed the search for a concept with the desired dimensions and capabilities.

The search for valid concepts that would meet these requirements has led to two main concepts. Both concepts involved planar manipulation. The two main concepts were a planar Cartesian manipulator and a planar revolute-joint based manipulator. Of these concepts, the Cartesian planar manipulator was determined to be the most viable concept as it allowed executing the defined tasks according to the requirements, using direct-drive actuators, with a comprehensive workspace for bi-manual manipulation. The planar revolute-joint based manipulator did not allow grabbing and placing of objects according to the defined requirements.

By first estimating peak-forces resulting from mechanical impacts, a finite force attributed to an impact load on the end-effector was used in a static force analysis to design for a worst-case scenario. The outcomes of the static force analysis formed a basis for the design of the motion-system. Impact resilience was achieved through compatibility between the selection of linear guides, and the introduction of a compliant mechanism as part of the end-effector. Herein, the end-effector was designed as the weakest component of the robot arms, preventing damage attributed to impacts. As a result, the concept was developed into an embodiment design shown in Figure 6.1.

Evaluating the functionality of the setup through multi-body simulation gained insight into the functionality of the setup. The simulations showed that the designed configuration allows effective object manipulation in combination with the suggested control routines. Yet, the simulations also showed that, for some cases, the selected actuators needed more thrust to meet the set requirements. The simulations also showed that for grabbing objects, the developed routines are valid, but not efficient, showing a full stop in the process of grabbing an object.

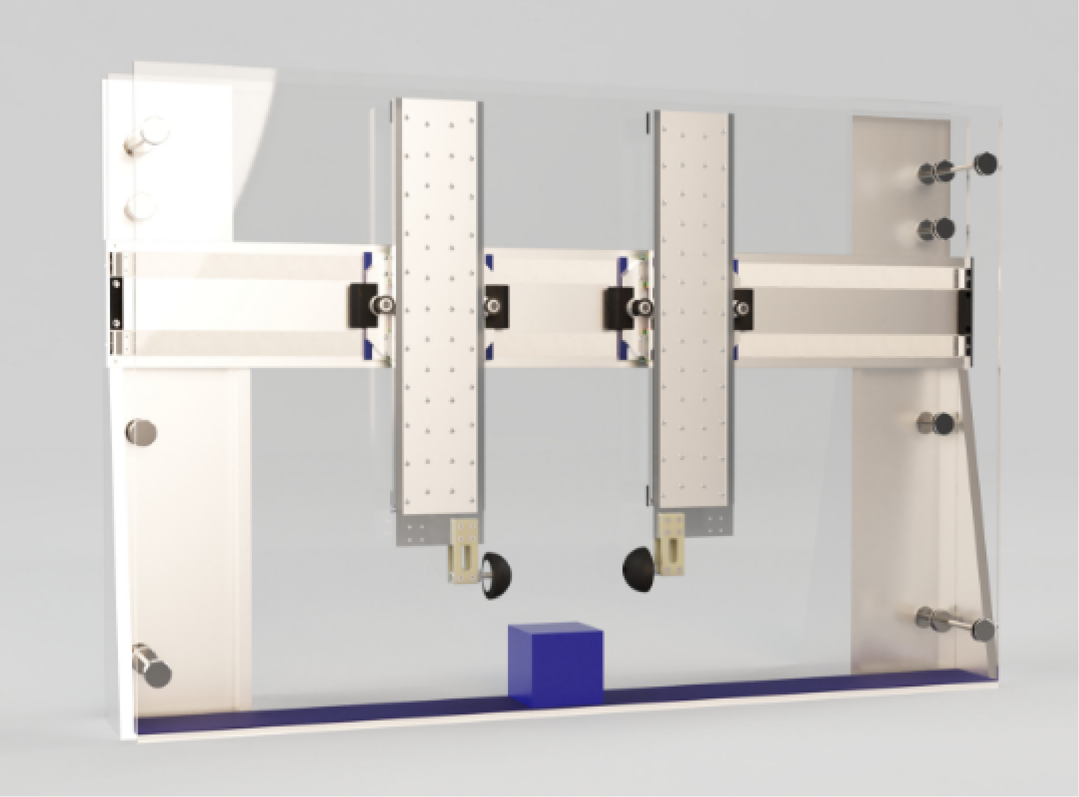

Figure 6.1: Photo-realistic render of the designed test-bed.

In the end, this thesis presents a setup that allows further development into a detailed design. Apart from the required actuator thrust, the design meets the set requirements.

6.2 Recommendations

This thesis presented a mechanical design for the test-bed. Although the design has a significant amount of detail and is composed considering manufacturability, it is not ready for realization. The realization of the setup suggests a re-evaluation of the design and the creation of a detailed mechanical design. This detailed design requires the definitive selection of actuators and bearings, according to the suggested routines in this report as these components have a significant influence on the mechanical design of the setup. Herein, suggesting to design the x- and y-stage first, determining the requirements on the enclosure and support structure.

In the development of the end-effector, several methods were considered to achieve compliance and damping. However, the final design of the end-effector only used simple mechanisms, although this simplicity may prove it reliable, it must be evaluated to confirm this. Further development of the end-effector would be possible using different techniques, as suggested in Section 4.1.3, to dampen impact-induced vibrations. These techniques could, for example, involve the use of granular matter, viscous air-damping, or the 3D printing of viscoelastic material. Further development could also concern the shape and dimensions of the end-effector.

The simulations of the functionality of the test-bed used the position of the object. To allow manipulation of the object, the realization of the setup requires the development of a vision system that could track the position of the object. The vision system would be placed behind or to the side of the setup.

As the simulations also effectively used force control in the manipulation of the object, the test-bed requires information on the force applied by the end-effectors. Registering force information through the correlation of forces with current supplied to the actuators provides a crude estimation. An improvement is the inclusion of a force sensor. Placing the force sensor near the end-effector or designing it as part of the structure of the robot. This sensor would improve the accuracy of force control during object manipulation.

Appendix A

Conceptualization

Table A.1 lists an overview of the considered design concepts. This appendix discusses concepts and variations which the main text does not discuss. Most considerations discussed in Chapter 3 apply to the to these concepts as well.

Table A.1: Overview of concepts for the test-setup for impact-aware robotic manipulation.

DOF	Actuation	Description
2D	Rotary	Two arms with both three rotary joints, elbow down.
		Two arms with both three rotary joints, elbow up.
	Cartesian	Two arms with both two prismatic joints.
		Two arms with both two prismatic joints + one rotary joint.
3D		Two arms with both three prismatic joints.

A.1 Considered concepts and variations

This section discusses the considered concepts and variations that Chapter 3 does not discuss. These concepts include a full DOF Cartesian concept and variations to the introduced revolute concept.

A.1.1 Three-dimensional Cartesian manipulator

Consider the concept of a three-dimensional Cartesian manipulator depicted in Figure A.1. The design uses linear motion actuators in a two-arm configuration. Each arm (C32+C34) is actuated in three directions with the x-axis (C33) of both arms spatially coinciding. In this way, both arms operate within one enclosure (C31).

By allowing three degrees-of-freedom per arm, the arms can bi-manually displace objects in a three-dimensional space. Similar to the Cartesian planar manipulator, it allows a limited amount of rotation of objects in any direction, by varying position of the arms independently of each other. Manipulating objects within a three-dimensional space allows a large viewing angle for demonstrations.

Executing a foreseen task, as listed in Chapter 2, as with the other concepts, could pose some limitations or challenges in the realization of this setup:

- Compared to the planar Cartesian manipulator, this design requires the x-stage to move an-

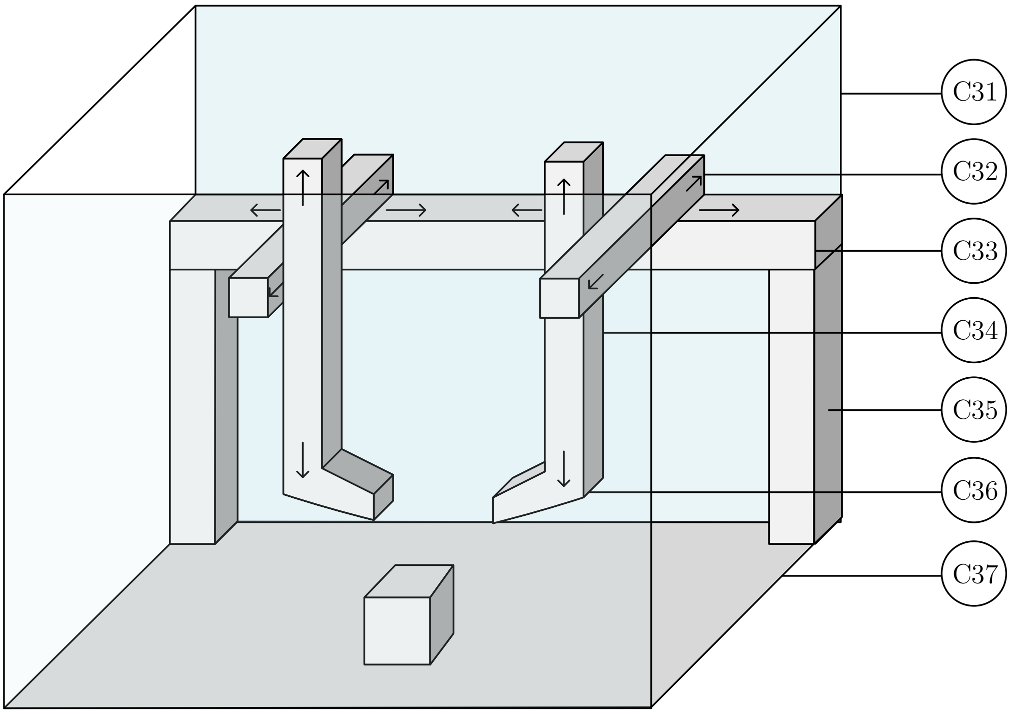

Figure A.1: Illustration of 3D Cartesian concept with: C31) enclosure, C32) depth-stage, C33) horizontal stage, C34) vertical stage, C35) support-structure, C36) end-effector, and C37) floor.

other set of actuators and bearings. The extra set of bearings and actuators would introduce a significant load and moment to be supported by the x-stage. Together with the loading of impacting nature, this structure would have to be in-practically rugged.

- The introduction of the third actuator per arm introduces an extra layer of complexity in terms of cable routing for actuators and sensors. The cables would have to route from the last arm segments to the static x-stage, also taking into account that the arms are moving, and the length of the segments thus changes.
- Developing this concept into a mechanically feasible design that is resilient to impacts, in combination with the required accelerations and velocities, requires a significantly higher amount of resources and costs than the other concepts.

A.1.2 Variations to concepts

This section discusses considered variations for both the Cartesian concepts, as well as the revolute concepts.

Cartesian concepts. The planar, as well as the three-dimensional Cartesian manipulator, allow rotation of the object to a certain degree, allowed by a specific design of the end-effectors. A rotary actuator just before the end-effector could allow for an improved ability to rotate objects, shown in Figure A.2a. Although it allows improved maneuverability of objects, implementing this actuator would imply an increase in cost, mass, and complexity.

Another variation to the planar Cartesian manipulator could be to use two vertical stages with both their horizontal stage, as shown in Figure A.2b. The concept positions the arms opposite to each other. In this way, the horizontal stage does not require any mechanism to be incorporated in the rear plane. A downside of this configuration is that the horizontal arms would have to be quite long to have a workspace similar to the planar Cartesian manipulator. As a result, the robot would have a full footprint width of >3 m to achieve the same workspace as the suggested concept achieves with a footprint <1.5 m, which would not be practical.

Revolute concepts. Figure A.3a depicts the variation of the revolute-joint based planar manipulator in terms of arm length, placement, and positioning. It shows an arm spacing of W, a setup height of H, an arm with three segments of length $L0$, $L1$, and $L3$, and an object of height and width d.

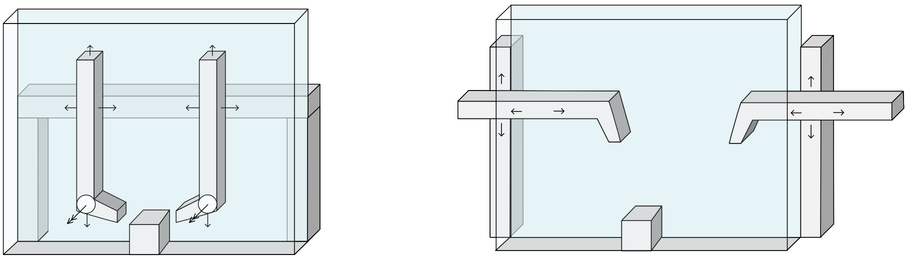

(a) (b)

Figure A.2: Variations to Cartesian planar manipulator with left (a), an additional rotary joint, and right (b), a different configuration.

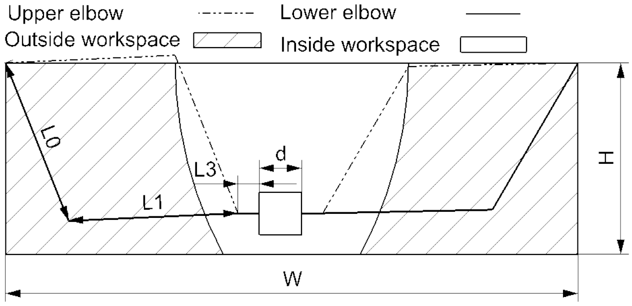

(a) Rotary two arm concept for planar robotic manipulator.

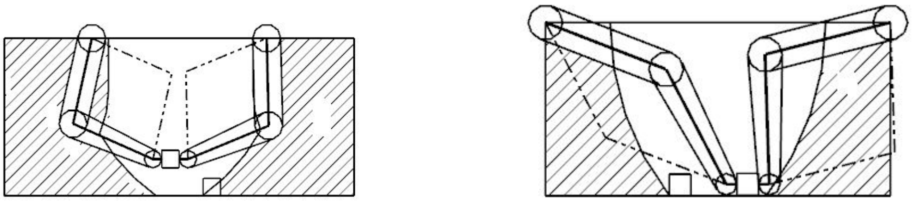

(b) Variant 1

(c) Variant 2

Figure A.3: Variations to the revolute-joint based planar manipulator with: (a), a schematic of concepts (b) and (c), (b), an elbow-down configuration, and (c), an elbow-up configuration.

Figure A.3b shows an elbow-down configuration. The workspace of the robot is around one-third of the total area available. This configuration uses the maximum space available in terms of the width of the footprint. The arm length is chosen accordingly to the width of the setup and the required room for the elbow-down configuration. The arm-length and the clearance around the arms determine the height of this configuration.

An elbow-up configuration is shown in Figure A.3c. The concept uses the maximum footprint in terms of width. A downside of such a configuration is that it would be impractical in throwing objects. It also requires longer arms with added weight and complexity due to more demanding requirements on stiffness and power to allow this.

Table A.2: Dimensions of revolute planar manipulator variations shown in Figure A.3.

Variant	1	2	
W [m]	1	1.6	Spacing of arms.
H [m]	0.9	0.8	Height of setup.
$L0$ [m]	0.5	0.6	Length of first arm.
$L1$ [m]	0.5	0.6	Length of second arm.
$L2$ [m]	0.05	0.05	Length of third arm.
d [m]	0.1	0.1	Width and height object.

A.2 Supporting calculations

This section discusses actuator power requirements by combining the concepts of Chapter 3, with the requirements of Chapter 2.

A.2.1 Cartesian planar manipulator concept

Figure A.4 depicts a kinematic model of the Cartesian 2D planar concept. It shows an object with mass m_{obj}, and an arm with mass m_y.

The required actuator force, $\vec{F}_{A_x}$ and $\vec{F}_{A_y}$, depends on the weight of the arm, the object, and the required accelerations for the tasks. These values are taken from Chapter 2, which requires a minimum horizontal acceleration of $a_{x,min}$ =17 m/s^2, and a minimum vertical acceleration of $a_{y,min}$ =20 m/s^2.

To achieve a vertical acceleration of the object, a force is required of:

$$\vec{F}_{A_y} = (m_{obj} + m_y)(a_{y,min} + g), \text{ and} \tag{A.1}$$

$$\vec{F}_{A_x} = \frac{\vec{F}_{A_y}}{\mu}, \tag{A.2}$$

in which μ is the friction coefficient between the end-effector and the object. To achieve a hori-

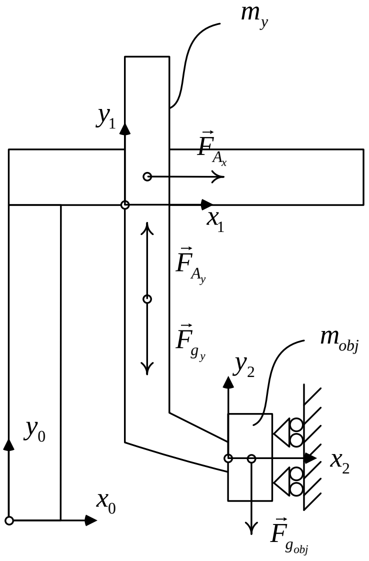

Figure A.4: The kinematic model used to compute requirements on actuators for the Cartesian planar manipulator concept.

zontal acceleration:

$$\vec{F}_{A_y} = (m_{obj} + m_y)(g), \text{ and} \tag{A.3}$$

$$\vec{F}_{A_x} = \frac{\vec{F}_{A_y}}{\mu} + (m_{obj} + m_y)(a_{x,min}). \tag{A.4}$$

In case of a simultaneous vertical, and horizontal, acceleration:

$$\vec{F}_{A_y} = (m_{obj} + m_y)(a_{y,min} + g), \text{ and} \tag{A.5}$$

$$\vec{F}_{A_x} = \frac{\vec{F}_{A_y}}{\mu} + (m_{obj} + m_y)(a_{x,min}). \tag{A.6}$$

For an indication of the required actuation force, the mass of the arm needs to be estimated.

Using catalogs for actuators and guides [40],[16], estimates the mass of the actuators and guides for the y-stage at 5 kg, and 5 kg for the x-stage. Although this only uses the mass of the arms, since these components make up most of the weight, it is assumed to be a valid estimation.

As a consequence, the estimated force required to accelerate these arms in the vertical direction is equal to approximately 0.17 kN, taking into account half the maximum object weight. The estimated force to accelerate the arms in the horizontal direction is equal to approximately 0.18 kN. When comparing these forces to the available actuators in [16], the required forces are well within the limits of the available actuators—making this a feasible concept from an actuation point of view.

A.2.2 Revolute planar manipulator concept

A kinematic model of the revolute 2D planar concept is shown in Figure A.5. The torque required for each actuator is, in contrast with the Cartesian concept, not only based on the required acceleration but also the required configuration during this acceleration.

The required actuator torque, $\vec{\tau}_1$, $\vec{\tau}_2$, and $\vec{\tau}_3$, depends on: the weight of the arm-segments, joints, and object, and the required accelerations for the tasks. These values are taken from Chapter 2, which means a minimum horizontal acceleration of $a_{x,min}$ =17 m/s^2, and a minimum vertical acceleration of $a_{y,min}$ =20 m/s^2.

Using joint space dynamics:

$$M(q)\ddot{q} + V(q,\dot{q}) + G(q) = \tau \tag{A.7}$$

in which $M(q)$ is the mass matrix, $V(q,\dot{q})$ represents the centrifugal and Coriolis forces, $G(q)$ represents the gravity force.

Given mass matrix $M(q)$:

$$M(q) = \begin{bmatrix} M_{11} & M_{12} & M_{13} \\ M_{12} & M_{22} & M_{23} \\ M_{13} & M_{23} & M_{33} \end{bmatrix}, \tag{A.8}$$

with:

$$
\begin{aligned}
M_{11} =& I_1 + I_2 + I_3 + \frac{1}{4} m_{l_0} {l_0}^2 + m_{j_1} {l_0}^2 + m_{l_1}(l_0^2 + \frac{1}{4} l_1^2 + l_0 l_1 c_2) + m_{j_2}(l_0^2 + l_1^2 + 2 l_0 l_1 c_2) \\
&+ m_{l_2}(l_0^2 + l_1^2 + \frac{1}{4} l_2^2 + 2 l_0 l_1 c_2 + l_0 l_2 c_{23} + l_1 l_2 c_3),
\end{aligned} \tag{A.9}
$$

$$
\begin{aligned}
M_{12} =& I_2 + I_3 + \frac{1}{2}(m_{l_1}(\frac{1}{2} l_1^2 + l_0 l_1 c_2) + m_{j_2}(2 l_1^2 + 2 l_0 l_1 c_2) \\
&+ m_{l_2}(2 l_1^2 + \frac{1}{2} l_2^2 + 2 l_0 l_1 c_2 + l_0 l_2 c_{23} + 2 l_1 l_2 c_3)),
\end{aligned} \tag{A.10}
$$

$$
M_{13} = I_3 + \frac{1}{2} m_{l_2}(\frac{1}{2} l_2^2 + l_0 l_2 c_{23} + l_1 l_2 c_3), \tag{A.11}
$$

$$
M_{22} = I_2 + I_3 + \frac{1}{4} m_{l_1} l_1^2 + m_{j_2} l_1^2 + m_{l_2}(l_1^2 + \frac{1}{4} l_2^2 + l_1 l_2 c_3), \tag{A.12}
$$

$$
M_{23} = I_3 + \frac{1}{2} m_{l_2}(\frac{1}{2} l_2^2 + l_1 l_2 c_3), \text{ and} \tag{A.13}
$$

$$
M_{33} = I_3 + \frac{1}{4} m_{l_2} l_2^2, \tag{A.14}
$$

in which I_1, I_2, and I_3 represent the inertia for each link estimated as a slender rod, m_{l_0}, m_{l_1} and m_{l_0} represent the mass of each link, l_0, l_1, and l_2 represent the length of each link.

Given the centrifugal and Coriolis matrix $V(q, \dot{q})$:

$$
V(q, \dot{q}) = \dot{M}\dot{q} - \frac{1}{2} \begin{bmatrix} \dot{q}^\top \frac{\partial M}{\partial q_1} \dot{q} \\ \dot{q}^\top \frac{\partial M}{\partial q_2} \dot{q} \\ \dot{q}^\top \frac{\partial M}{\partial q_3} \dot{q} \end{bmatrix} = \begin{bmatrix} V_{11} - \frac{1}{2} V_{21} \\ V_{12} - \frac{1}{2} V_{22} \\ V_{13} - \frac{1}{2} V_{23} \end{bmatrix}, \tag{A.15}
$$

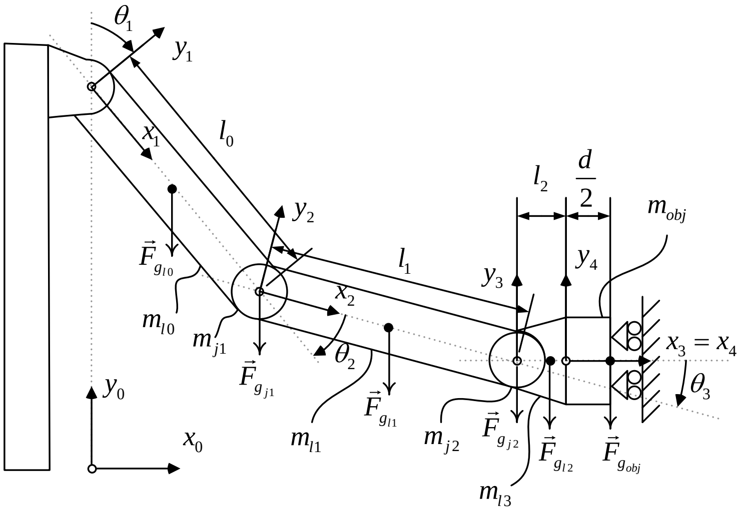

Figure A.5: The kinematic model used to compute requirements on actuators for revolute-joint based planar manipulator concept.

with:

$$\begin{aligned}
V_{11} =& -\left((m_{l_1}+2m_{j_2})l_0l_1s_2+m_{l_2}l_0(2l_1s_2+l_2s_{23})\right)\dot{q}_1\dot{q}_2-m_{l_2}l_2\left(l_0s_{23}+l_1s_3\right)\dot{q}_1\dot{q}_3 \\
&-\left(\frac{1}{2}(m_{l_1}+2m_{j_2})l_0l_1s_2+m_{l_2}l_0(2l_1s_2+l_2s_{23})\right)\dot{q}_2^2-m_{l_2}l_2\left(l_0s_{23}+l_1s_3\right)\dot{q}_2\dot{q}_3 \\
&-\frac{1}{2}m_{l_2}l_2\left(l_0s_{23}+l_1s_3\right)\dot{q}_3^2,
\end{aligned} \tag{A.16}$$

$$\begin{aligned}
V_{12} =& -\left(\frac{1}{2}(m_{l_1}+2m_{j_2})l_0l_1s_2+m_{l_2}l_0(2l_1s_2+l_2s_{23})\right)\dot{q}_1\dot{q}_2-\frac{1}{2}m_{l_2}l_2\left(l_0s_{23}+l_1s_3\right)\dot{q}_1\dot{q}_3 \\
&-m_{l_2}l_1l_2s_3\dot{q}_2\dot{q}_3-\frac{1}{2}m_{l_2}l_1l_2s_3\dot{q}_3^2,
\end{aligned} \tag{A.17}$$

$$V_{13} = -\frac{1}{2}m_{l_2}l_0l_2s_{23}\dot{q}_1\dot{q}_2-\frac{1}{2}m_{l_2}l_2\left(l_0s_{23}+l_1s_3\right)\dot{q}_1\dot{q}_3-\frac{1}{2}m_{l_2}l_1l_2s_3\dot{q}_2\dot{q}_3, \tag{A.18}$$

$$V_{21} =0, \tag{A.19}$$

$$\begin{aligned}
V_{22} =& -(m_{l_1}+2m_{j_2})l_0l_1s_2+m_{l_2}l_0(2l_1s_2+l_2s_{23})\dot{q}_1^2 \\
&-\left((m_{l_1}+2m_{j_2})l_0l_1s_2+m_{l_2}l_0(2l_1s_2+l_2s_{23})\right)\dot{q}_1\dot{q}_2-m_{l_2}l_0l_2s_{23}\dot{q}_1\dot{q}_3,
\end{aligned} \tag{A.20}$$

$$\begin{aligned}
V_{23} =& -m_{l_2}l_2\left(l_0s_{23}+l_1s_3\right)\dot{q}_1^2-m_{l_2}l_2\left(l_0s_{23}+2l_1s_3\right)\dot{q}_1\dot{q}_2-m_{l_2}l_2\left(l_0s_{23}+l_1s_3\right)\dot{q}_1\dot{q}_3 \\
&-m_{l_2}l_1l_2s_3\dot{q}_3^2-m_{l_2}l_1l_2s_3\dot{q}_2\dot{q}_3.
\end{aligned} \tag{A.21}$$

And given the mass matrix with:

$$\begin{aligned}
G_1 =&(c_1l_0+c_{12}l_1+c_{123}l_2)gm_o+(c_1l_0+c_{12}l_1+\frac{1}{2}c_{123}l_2)gm_{l_2} \\
&+(c_1l_0+c_{12}l_1)gm_{j_2}+(c_1l_0+\frac{1}{2}c_{12}l_1)gm_{l_1}+c_1l_0gm_{j_1}+\frac{1}{2}c_1l_1gm_{l_0} \\
&+(S_1l_0+S_{12}l_1+S_{123}l_2)\frac{gm_{obj}}{\mu}
\end{aligned} \tag{A.22}$$

$$\begin{aligned}
G_2 =&(c_{123}l_2+c_{12}l_1)gm_o+(\frac{1}{2}c_{123}l_2+c_{12}l_1)gm_{l_1} \\
&+c_12l_1gm_{j1}+\frac{1}{2}c_{12}l_1gm_{l0}+(s_{123}l_2+s_{12}l_1)\frac{gm_o}{\mu}, \text{ and}
\end{aligned} \tag{A.23}$$

$$G_3 =c_{123}l_2gm_o+\frac{1}{2}c_{123}l_2gm_{l_2}. \tag{A.24}$$

Estimation arm mass. The mass of an arm is estimated by using a square aluminum tube of: 0.1 m×0.1 m, with a thickness of 1.0×10^{-3} m, a length corresponding with Table A.2. Which leads to a mass of 0.5 kg for an arm of 0.5 m, and 0.6 kg for an arm of 0.6 m.

Table A.3 shows the required torque for two different configurations. The torque is computed by computing q, $\dot{q}$, and $\ddot{q}$ through the inverse kinematics of a vertical acceleration according to the requirements. The elbow-up configuration required too much torque to be feasible for a direct-drive approach [15]. The elbow-down configuration is feasible, but even when not taking into account the extra weight of bearings, the required torque is already significant.

Table A.3: Computations on required torque for revolute-joint based concept.

Parameter	1	2	Unit	Description
l_0	0.5	0.6	m	Length of first arm-segment
l_1	0.5	0.6	m	Length of second arm-segment
l_2	0.05	0.05	m	Length of third arm-segment
m_{l_0}	0.5	0.6	kg	Mass of first arm-segment
m_{l_1}	0.5	0.6	kg	Mass of second arm-segment
m_{l_2}	0.3	0.3	kg	Mass of third arm-segment
m_{j_1}	2.7	2.7	kg	Mass of second joint
m_{j_2}	0.8	0.8	kg	Mass of third joint
τ_1	87	105	Nm	Torque required first joint
$\tau_{mot,1}$	92	91.6	Nm	Torque available first joint
τ_2	28	30	Nm	Torque required second joint
$\tau_{mot,2}$	56	91.6	Nm	Torque available second joint
τ_3	0.19	0.5	Nm	Torque required third joint
$\tau_{mot,3}$	5.5	5.47	Nm	Torque available third joint
Feasible?	yes	no		

Appendix B

Static force transfer analysis

Using a static force analysis, the forces and moments present in the arms of the setup are computed conform to Figure B.1. The dimensions correspond to the layout of the guides, not the actual dimensions of the arms.

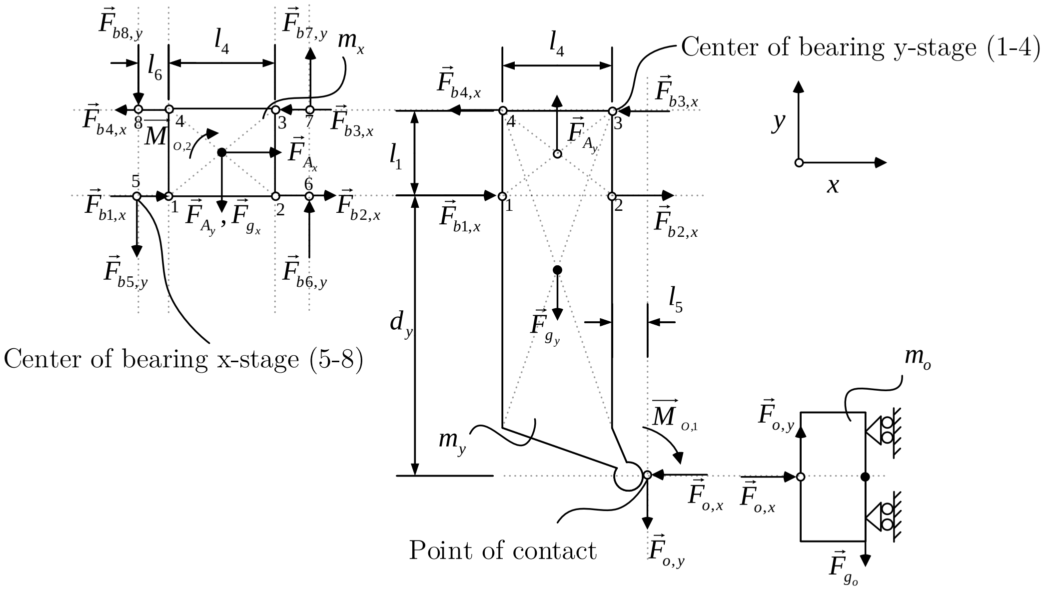

(a) (b) (c)

Figure B.1: Free-body diagram of (a) x-stage, (b) y-stage and (c) object.

B.1 Static force analysis

The x-, and y-stage are analyzed using a static force analysis in the following sections. The object is constrained from moving in the x-direction.

B.1.1 Object force analysis

According to Figure B.1:

$$F_{g_o} = -m_o g, \tag{B.1}$$

$$F_{o,y} = m_o(g + a_{o,y}), \text{ and} \tag{B.2}$$

$$F_{o,x} = \mu F_{o,y}, \tag{B.3}$$

where: mo is the object's mass, g is the gravitational acceleration, $a_{o,y}$ is the object's vertical acceleration, and μ is the friction coefficient between the object and the end-effector.

B.1.2 Y-stage static force analysis

The following equilibria must hold for the y-stage, where:

$$\sum \vec{F}_x = \vec{F}_{o,x} + \vec{F}_{b1,x} + \vec{F}_{b2,x} + \vec{F}_{b3,x} + \vec{F}_{b4,x} = \vec{0}, \tag{B.4}$$

$$\sum \vec{F}_y = \vec{F}_{o,y} + \vec{F}_{A_y} + \vec{F}_{g_y} = \vec{0}, \text{ with } \vec{F}_{g_y} = m_o\vec{g}, \text{ and} \tag{B.5}$$

$$\sum \vec{M}_{O,1} = d_y(\vec{F}_{b1,x} + \vec{F}_{b2,x}) + (d_y + l_1)(\vec{F}_{b3,x} + \vec{F}_{b4,x}) + \left(\frac{l_4}{2} + l_5\right)(\vec{F}_{A,y} + \vec{F}_{g_y}) = \vec{0}, \tag{B.6}$$

in which: d_y, l_1, l_4 and l_5 are dimensions as depicted in Figure B.1, $\vec{F}_{A_y}$ is the force generated by the motor, $\vec{F}_{bn,x}$ the force exerted on bearing $n = 1$ until 4, and m_o the mass of the y-stage. Rewriting (B.4), (B.5), and (B.6) leads to the following expressions:

$$\vec{F}_{A_y} = -\vec{F}_{o,y} - \vec{F}_{g_y}, \tag{B.7}$$

$$\vec{F}_{b3,x} = \vec{F}_{b4,x} = \frac{-d_y\vec{F}_{o,x} - \left(l_5 + \frac{l_4}{2}\right)\vec{F}_{o,y}}{2l_1}, \text{ and} \tag{B.8}$$

$$\vec{F}_{b1,x} = \vec{F}_{b2,x} = -\vec{F}_{b3,x} - \vec{F}_{o,x}/2. \tag{B.9}$$

B.1.3 x-stage static force analysis

The following equilibria must hold for the x-stage, where:

$$\sum \vec{F}_x = \vec{F}_{b1,x} + \vec{F}_{b2,x} + \vec{F}_{b3,x} + \vec{F}_{b4,x} + \vec{F}_{A_x} = \vec{0}, \tag{B.10}$$

$$\sum \vec{F}_y = \vec{F}_{b5,y} + \vec{F}_{b6,y} + \vec{F}_{b7,y} + \vec{F}_{b8,y} + \vec{F}_{A_y} + \vec{F}_{g_x} = \vec{0}, \text{ and} \tag{B.11}$$

$$\sum \vec{M}_{O,2} = \frac{l_1}{2}(\vec{F}_{b1,x} + \vec{F}_{b2,x} - \vec{F}_{b3,x} - \vec{F}_{b4,x}) + \left(\frac{l_4}{2} + l_6\right)(-\vec{F}_{b5,y} + \vec{F}_{b6,y} + \vec{F}_{b7,y} - \vec{F}_{b8,y}) = \vec{0}. \tag{B.12}$$

A combination of (B.8), (B.9), and (B.10) leads to:

$$\vec{F}_{A_x} = -2\vec{F}_{b1,x} - 2\vec{F}_{b3,x} = \vec{F}_{o,x}. \tag{B.13}$$

Following from (B.8), (B.9), (B.11), and (B.12):

$$\begin{aligned}\vec{F}_{b6,y} &= -\frac{l_1}{2l_4+4l_6}(\vec{F}_{b1,x}-\vec{F}_{b3,x}) - \frac{\vec{F}_{A_y}+\vec{F}_{g_x}}{4} \\ &= \frac{\vec{F}_{o,x}\left(d_y+\frac{l_1}{2}\right)+\vec{F}_{o,y}\left(l_5+\frac{l_4}{2}\right)}{2l_4+4l_6} - \frac{\vec{F}_{A_y}+\vec{F}_{g_x}}{4}.\end{aligned} \tag{B.14}$$

B.2 Force transfer ratio

The equations (B.8), (B.9), and (B.14) are used to determine a transfer ratio between the force applied to the end-effector and the force on the carriages. Table B.1 is used in the following computations.

Equation (B.8) and (B.9), in combination with Table B.1, lead to:

$$\vec{F}_{b3,x} = \vec{F}_{b4,x} \approx -2.1\vec{F}_{o,x} - 0.63\vec{F}_{o,y}, \text{ and} \tag{B.15}$$

$$\vec{F}_{b1,x} = \vec{F}_{b2,x} \approx -2.6\vec{F}_{o,x} - 0.63\vec{F}_{o,y}. \tag{B.16}$$

Which shows that peak forces applied to the end-effector in horizontal direction have a transmission ratio significantly higher than the transmission ratio for forces applied in vertical direction. Now, for the x-stage, using (B.7) and (B.14), in combination with Table B.1, the following holds:

$$\begin{aligned}\vec{F}_{b5,y} = \vec{F}_{b8,y} &\approx -1.8\vec{F}_{o,x} - 0.49\vec{F}_{o,y} - \frac{\vec{F}_{A_y}+\vec{F}_{g_x}}{4} \\ &\approx -1.8\vec{F}_{o,x} - 0.74\vec{F}_{o,y} - \frac{\vec{F}_{g_x}+\vec{F}_{g_y}}{4}, \text{ and}\end{aligned} \tag{B.17}$$

$$\begin{aligned}\vec{F}_{b6,y} = \vec{F}_{b7,y} &\approx -1.8\vec{F}_{o,x} - 0.49\vec{F}_{o,y} + \frac{\vec{F}_{A_y}+\vec{F}_{g_x}}{4} \\ &\approx -1.8\vec{F}_{o,x} - 0.24\vec{F}_{o,y} + \frac{\vec{F}_{g_x}+\vec{F}_{g_y}}{4}.\end{aligned} \tag{B.18}$$

Showing that the forces applied to the end-effector in horizontal direction are amplified, be it with a less significant amount as for the y-stage, and are important to take into account in designing the end-effector.

Table B.1: Parameters used in computations transmission ratios.

Parameter	Value	Unit	Description
l_1	0.13	m	vertical spacing bearings y-stage
l_4	0.11	m	horizontal spacing bearings y-stage
l_5	0.11	m	end-effector horizontal offset
l_6	0.03	m	horizontal spacing offset bearings x-stage
d_y	0.54	m	vertical arm end-effector
m_o	0.5	kg	mass of object
m_y	5	kg	mass of y-stage
m_x	5	kg	mass of x-stage

B.3 Load on bearings

By using the transmission ratios computed in Section B.2, the load on the guides can be computed. The following sections compute the total load on the guides, as well as the maximum and minimum loads.

B.3.1 Total load

The total load on a carriage is generated by a combination of the force applied by the actuators, the attraction between the coil-unit and magnet-track of the linear-motor, and externally induced forces. The externally induced forces are forces generated by impacts. The magnitude of the load on each of the carriages is a combination of the orthogonal force, F_b, and the motor attraction force, F_{MA}:

$$F_{tot} = F_b + F_{MA}, \tag{B.19}$$

with F_{tot} being the total equivalent load applied to the carriage, computed according to manufacturer specifications.

B.3.2 Minimum and maximum constant load

To allow analyzing the load characteristics during operation, the following two paragraphs derive both a maximum and minimum constant load.

Maximum constant load. The maximum constant load applied to the bearings is realized when both actuators deliver their full power. By rewriting (B.15) until (B.18), the following holds:

$$F_{b3,x} = F_{b4,x} \approx -2.1F_{A_x} - 0.63(F_{A_y} - F_{g_y}), \tag{B.20}$$

$$F_{b1,x} = F_{b2,x} \approx -2.6F_{A_x} - 0.63(F_{A_y} - F_{g_y}), \tag{B.21}$$

$$F_{b5,y} = F_{b8,y} \approx 1.8F_{A_x} + 0.49(F_{A_y} - F_{g_y}) + \frac{F_{A_y} + F_{g_x}}{4}, \text{ and} \tag{B.22}$$

$$F_{b6,y} = F_{b7,y} \approx 1.8F_{A_x} + 0.49(F_{A_y} - F_{g_y}) - \frac{F_{A_y} + F_{g_x}}{4}. \tag{B.23}$$

The maximum constant load on the bearings can now be computed with a combination of the maximum motor forces, and the motor attraction forces.

Minimum constant load. In the case that the actuators provide zero thrust, there still is a load acting on the bearings: the minimum constant load.

Overview of constant loads. An overview of the maximum actuator force and the motor attraction force, for each stage, is shown in Table B.2. Filling in these values in (B.20) to (B.23) leads to the minimum, and maximum, constant loads on the bearings, shown in Table B.2. It shows that the motor attraction force is responsible for the minimum constant load on the bearings. It also shows that the maximum constant load experienced by the guides is $P_{c_{b3},max} = P_{c_{b4},max} = 7.7 \times 10^2$ N. This maximum value must be used in selecting the guides for this setup.

Table B.2: Parameters used in computations constant loads.

Parameter	Value	Unit	Description
$F_{A_y,max}$	1.7×10^2	N	Maximum force applied by y-stage actuator
$F_{A_x,max}$	2.4×10^2	N	Maximum force applied by x-stage actuator
F_{MA_y}	3.0×10^2	N	Motor attraction force y-stage actuator
F_{MA_x}	5.0×10^2	N	Motor attraction force x-stage actuator

Table B.3: Constant loads given parameters in Table B.2.

Parameter	Value	Unit	Description
$P_{c_{b1},min}$ and $P_{c_{b2},min}$	1.1×10^2	N	Minimum constant load exerted on y-stage guides
$P_{c_{b3},min}$ and $P_{c_{b4},min}$	1.1×10^2	N	Minimum constant load exerted on y-stage guides
$P_{c_{b5},min}$ and $P_{c_{b8},min}$	1.5×10^2	N	Minimum constant load exerted on x-stage guides
$P_{c_{b6},min}$ and $P_{c_{b7},min}$	1.5×10^2	N	Minimum constant load exerted on x-stage guides
$P_{c_{b1},max}$ and $P_{c_{b2},max}$	6.5×10^2	N	Maximum constant load exerted on y-stage guides
$P_{c_{b3},max}$ and $P_{c_{b4},max}$	7.7×10^2	N	Maximum constant load exerted on y-stage guides
$P_{c_{b5},max}$ and $P_{c_{b8},max}$	6.7×10^2	N	Maximum constant load exerted on x-stage guides
$P_{c_{b6},max}$ and $P_{c_{b7},max}$	5.6×10^2	N	Maximum constant load exerted on x-stage guides

Appendix C

Linear motion guide selection

Options concerning linear guides are rolling contact guides, hydrodynamic sliding guides, fluidostatic sliding guides, and magnetic guides, [41]. Rolling contact guides are most practical for this setup as they are available in a wide range of standard sizes, are relatively inexpensive and low friction compared to the other types. Rolling contact guides could be ball-based, roller-based, or cam-based. Since ball and roller based guides offer a better load-bearing capability, these are considered for the setup.

C.1 Linear roller guideway

Consider an image of a linear guideway in Figure C.1 [40]. In this figure the different sub-components are named for reference in this appendix.

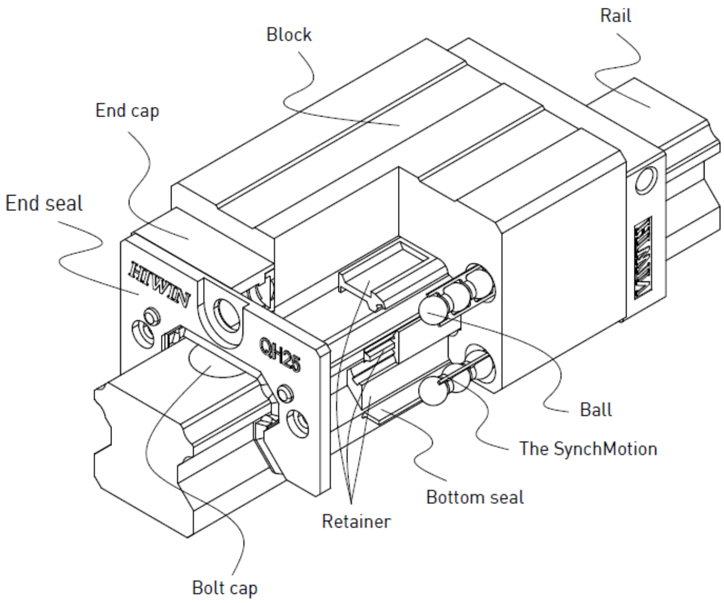

Figure C.1: Illustration of linear guide carriage showing various sub-components.

C.2 Characteristics

This section discusses the important characteristics of linear guides to help select the right type of guide. The following sections discuss the definition of the load-rating, the lifetime expectancy, the selection of preload, and the expected friction [40].

C.2.1 Load-rating

Aside from the evident specifications such as dimensions and mass, a linear guide has two defining ratings concerning the maximum allowable load: static load rating, C_{stat} and dynamic load rating, C_{dyn}. The static load rating determines the maximum permissible load on the guides before plastic deformation occurs. The dynamic load rating is a parameter in combination with the expected load, determines the expected lifetime of a bearing. The static load rating is, by definition, higher than the dynamic load rating.

Even if the expected lifetime might be over multiple years, if the static load-rating is exceeded, the actual lifetime of the guide might reduce to a couple of days. The peak-forces exerted on the arm should be below the static load rating. Staying below this static load-rating requires the computation of expected peak-forces and taking into-account lever ratios which might increase peak-loads. The peak-force can be reduced by introducing compliance at the places of impact. These places include the end-effector and the potential collision points between different parts of the arms.

C.2.2 Lifetime expectancy

The lifetime expectancy of a bearing depends on its load and usage. The expected lifetime is computed based the values shown in Table C.1.

time-based lifetime expectancy. If the setup is expected to be operated two hours a day, three days a week, thirty weeks a year, for five years, then a simple multiplication estimates a lifetime expectancy t_e of 900 h. For ease of calculation, t_e is taken to be 1×10^3 h=3.6×10^6 s.

The average expected velocity over these operating hours is set to $v_e = 1\,\mathrm{m/s}$, an overestimation for the size and use of this setup. Together with the lifetime expectancy, this would imply an expected distance over lifetime of:

$$L_e = t_e \cdot V_e = 3.6 \times 10^6\,\mathrm{s} \cdot 1\,\mathrm{m/s} = 3.6 \times 10^6\,\mathrm{m}. \tag{C.1}$$

Table C.1: Parameters used in computations life-time expectancy.

Parameter	Value	Unit	Description
t_e	1	h	Expected lifetime
v_e	1	m/s	Average velocity over expected lifetime
f_h	1	-	hardness factor
f_t	1	-	temperature factor
f_w	3.5	-	load factor

load-based lifetime expectancy. A manufacturer calculates the expected lifetime based on the the ratio between the expected and the dynamic load rating, and the use of either ball- or roller-bearings, [40]. This life-time is considered the load based expected distance over lifetime, L_l, for which:

$$L_{l,b} = \left(\frac{f_h \cdot f_t \cdot C}{f_w \cdot P}\right)^3 \cdot 50 \times 10^3, \tag{C.2}$$

in the case of ball-bearings. In the case of roller bearings:

$$L_{l,r} = \left(\frac{f_h \cdot f_t \cdot C}{f_w \cdot P}\right)^{\frac{10}{3}} \cdot 100 \times 10^3. \tag{C.3}$$

In which P is the actual applied load, f_h is the hardness-factor, f_h is the temperature-factor, and f_w is the load-factor.

The hardness factor relates to the hardness of the raceway. The hardness of a raceway can be classified in Rockwell Hardness (HRC). If a raceway has a hardness lower than the recommended hardness of 58-62 HRC, then a reduction in a lifetime is expected. Since this is considered a standard for steel raceways, the hardness factor is kept at one, meaning that the used raceways are expected to meet this standard.

The temperature factor relates to the degradation of linear guides in terms of performance at temperatures above 100 degrees Celsius. Temperatures above 100 degrees Celsius are not expected in this setup; thus, the temperature factor is kept at one.

The load factor relates to the load on a linear guide being variable and hard to predict, especially in the case of mechanical vibrations and impacts. For this reason, f_w is introduced, it is considered to be an empirical factor which, in the case of expected impacts and vibrations, is recommended to have a value in the range of 2.0 to 3.5. This factor is taken to be 3.5, to compute for a worst-case scenario. Note that the load for this setup is known, and thus, this must be considered as a safety factor.

Rewriting both equations to compute a minimum dynamic load rating, in the case of ball-bearings we have:

$$C_{min,b} = \left(\frac{L_e}{50 \times 10^3}\right)^{\frac{1}{3}} \cdot \frac{f_w}{f_h f_t} \cdot P_{max} = \left(\frac{L_e}{50 \times 10^3}\right)^{\frac{1}{3}} \cdot 3.5 P_{max}, \tag{C.4}$$

in the case of roller bearings we have:

$$C_{min,r} = \left(\frac{L_e}{100 \times 10^3}\right)^{\frac{3}{10}} \cdot \frac{f_w}{f_h f_t} \cdot P_{max} = \left(\frac{L_e}{100 \times 10^3}\right)^{\frac{3}{10}} \cdot 3.5 P_{max}. \tag{C.5}$$

In which the minimum dynamic load-rating for either ball-bearings, $C_{min,b}$, or roller-bearings, $C_{min,r}$, is computed based on the maximum expected constant load on the bearings, P_{max}.

Minimum dynamic load-rating. By using the loads computed in Appendix B, the maximum constant load on the bearings is shown in Table B.3 for both the y-stage, and the x-stage. It shows that the maximum constant load exerted on the guides is 6.7×10^2 N for the x-stage, and 7.7×10^2 N for the y-stage. Using these values for P_{max} in (C.4) and (C.5) leads to the minimum required dynamic load rating in the case of ball-bearings:

$$C_{min,b} = 11 \times 10^3 \,\text{N}, \tag{C.6}$$

and in the case of roller bearings:

$$C_{min,r} = 7.9 \times 10^3 \,\text{N}. \tag{C.7}$$

By comparing these dynamic load requirements with the datasheet shown in Figure C.2, the minimum dynamic load rating for this setup is not a choice limiting requirement. The choice for the correct guides must thus be based on the static load-rating rather than the dynamic load-rating.

C.2.3 Preload

In selecting bearings, a designer has to opt for a specific preload. Preload is commonly realized by placing larger rolling elements than the clearance between raceway and carriage allows. The rolling elements are deformed and exert a load on the carriage and raceway, based on their stiffness and deformation. The preload, defined as a percentage of the dynamic load capacity, C, as specified in the datasheet, generally ranges from $0C$ to $0.12C$.

Preload is introduced to improve stiffness and positioning precision, at the cost of a reduction in lifetime expectancy, and an increase in rolling friction. In the to-be designed setup there is no real need for high positioning accuracy such as required for, for example, CNC milling machines. Thus, a light preload of $0.02C$ is selected, leading to:

$$C_{min,b} = 11 \times 10^3\,\mathrm{N} + 0.02C, \text{ and} \tag{C.8}$$

$$C_{min,r} = 7.9 \times 10^3\,\mathrm{N} + 0.02C. \tag{C.9}$$

As an example, a preload of $0.02C$, for a guide with a dynamic load capacity of $20 \times 10^3\,\mathrm{N}$, would mean an additional load of $0.4 \times 10^3\,\mathrm{N}$, and thus an increase of the dynamic load-rating of $5.8 \times 10^3\,\mathrm{N}$ based on (C.4) for a ball-bearing.

C.2.4 Friction

Although it is challenging to predict friction experienced during operation accurately, it is possible to acquire an order of magnitude. According to the manufacturer, in the case of a load less than $0.1C_0$, friction is mainly experienced due to grease viscosity and friction between rolling elements. Using the minimum static load rating shown in Figure C.2, $0.1C_0$ would imply a load of $\approx 2 \times 10^3\,\mathrm{N}$. Thus, for this setup, friction is mainly experienced due to grease viscosity and friction between rolling elements.

The expected friction, F_W, is calculated through:

$$F_W = \mu P + S, \tag{C.10}$$

in which μ is the friction coefficient, P is the applied load, and S is the friction resistance, the resistance mainly due to seals of the carriages.

Maximum expected friction. If a friction coefficient of $\mu = 0.004$ is used, using (C.10) in combination with the loads shown in Table B.3, taking into account the additional load due to preload, leads to a maximum friction of:

$$F_{W,y} = \mu P_{c_{tot},max} + S = 0.004 \cdot (2 \cdot 6.9 \times 10^2 + 2 \cdot 8.1 \times 10^2) + 4.8\,\mathrm{N} = 17\,\mathrm{N} \tag{C.11}$$

$$F_{W,x} = \mu P_{c_{tot},max} + S = 0.004 \cdot (2 \cdot 7.1 \times 10^2 + 2 \cdot 6.0 \times 10^2) + 4.8\,\mathrm{N} = 15\,\mathrm{N} \tag{C.12}$$

Note that S is taken to be $4.8\,\mathrm{N}$, the total expected maximum seal resistance based on manufacturer specifications for the smallest guide shown in Figure C.2.

Minimum expected friction. Again, if a friction coefficient of $\mu = 0.004$ is used, using (C.10) in combination with the loads shown in Table B.3, leads to a minimum friction of:

$$F_{W,y} = \mu P_{c_{tot},max} + S = 0.004 \cdot (4 \cdot 1.1 \times 10^2) + 4.8\,\mathrm{N} = 7.8\,\mathrm{N} \tag{C.13}$$

$$F_{W,y} = \mu P_{c_{tot},max} + S = 0.004 \cdot (4 \cdot 1.5 \times 10^2) + 4.8\,\mathrm{N} = 7.2\,\mathrm{N} \tag{C.14}$$

The total friction thus ranges from 7 to 17 N.

C.3 Selection using datasheet

The specifications sheet for a type of linear guide which is suitable for this setup is shown in Figure C.2. The following sections discuss the selection and the implications of selecting a specific type of guide.

C.3.1 selection

The selection of the proper linear guide is based on the dynamic load-rating, the weight, and the dimensions. The datasheet in Figure C.2 shows an increasing dynamic load-rating for increasing ball-bearing size. The determined minimum dynamic load-rating for this setup, based on load and preload, is C_{min} =16.8×10^3 N, which is below the lowest dynamic load-rating in Figure C.2. Note that although the requirements on the dynamic-load rating are lower for roller bearings, these bearings come with increased weight for the minimum bearing size.

Increasing the size of the linear bearing increases the dynamic- and static load rating. It increases the lifetime of these guides at the cost of the block- and rail-weight.

Based on the required dynamic load-rating, the weight and capacity of roller- versus ball-bearings, and the available bearings shown in Figure C.2, the guides chosen for this setup are of model QHH15CA.

C.3.2 Maximum peak-force

The choice to use the QHH15CA implies a static load-rating of 20×10^3 N. The static load-rating must not be exceeded, exceeding it damages the guides. With use of (B.16), the maximum transmission ratio between the end-effector and the guides is 2.6. Such a transmission ratio, in combination with the static load-rating of 20×10^3 N implies that the peak-force applied to the end-effector must be limited to a force of $F = 20e3/2.6$ =7.7×10^3 N.

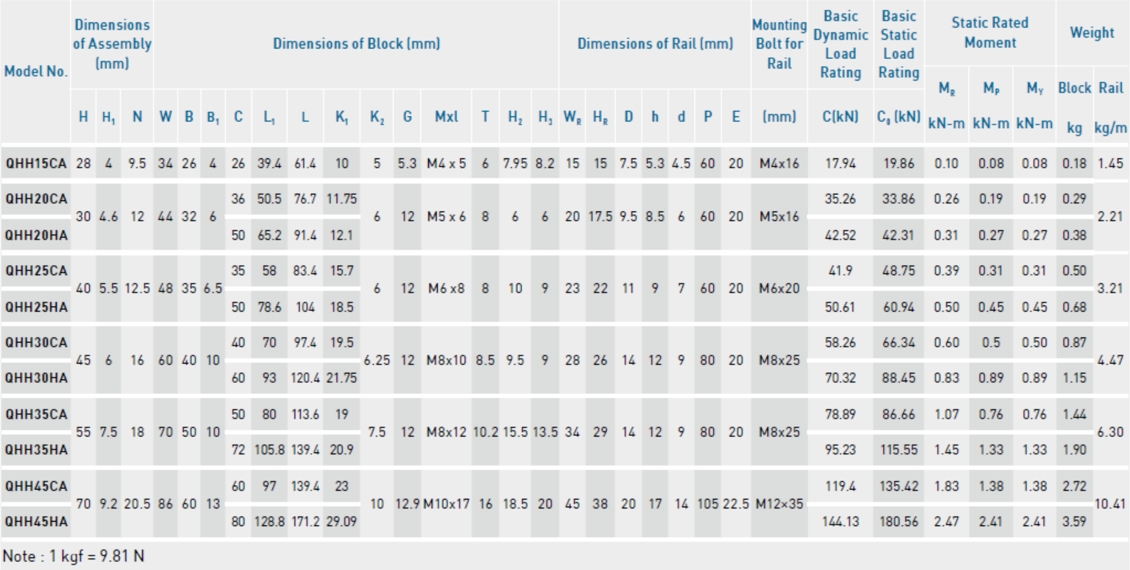

Model No.	Dimensions of Assembly (mm)			Dimensions of Block (mm)													Dimensions of Rail (mm)							Mounting Bolt for Rail	Basic Dynamic Load Rating	Basic Static Load Rating	Static Rated Moment			Weight	
																											M_R	M_P	M_Y	Block	Rail
	H	H_1	N	W	B	B_1	C	L_1	L	K_1	K_2	G	Mxl	T	H_2	H_3	W_R	H_R	D	h	d	P	E	(mm)	C(kN)	C_0 (kN)	kN-m	kN-m	kN-m	kg	kg/m
QHH15CA	28	4	9.5	34	26	4	26	39.4	61.4	10	5	5.3	M4 x 5	6	7.95	8.2	15	15	7.5	5.3	4.5	60	20	M4x16	17.94	19.86	0.10	0.08	0.08	0.18	1.45
QHH20CA	30	4.6	12	44	32	6	36	50.5	76.7	11.75	6	12	M5 x 6	8	6	6	20	17.5	9.5	8.5	6	60	20	M5x16	35.26	33.86	0.26	0.19	0.19	0.29	2.21
QHH20HA							50	65.2	91.4	12.1															42.52	42.31	0.31	0.27	0.27	0.38	
QHH25CA	40	5.5	12.5	48	35	6.5	35	58	83.4	15.7	6	12	M6 x8	8	10	9	23	22	11	9	7	60	20	M6x20	41.9	48.75	0.39	0.31	0.31	0.50	3.21
QHH25HA							50	78.6	104	18.5															50.61	60.94	0.50	0.45	0.45	0.68	
QHH30CA	45	6	16	60	40	10	40	70	97.4	19.5	6.25	12	M8x10	8.5	9.5	9	28	26	14	12	9	80	20	M8x25	58.26	66.34	0.60	0.5	0.50	0.87	4.47
QHH30HA							60	93	120.4	21.75															70.32	88.45	0.83	0.89	0.89	1.15	
QHH35CA	55	7.5	18	70	50	10	50	80	113.6	19	7.5	12	M8x12	10.2	15.5	13.5	34	29	14	12	9	80	20	M8x25	78.89	86.66	1.07	0.76	0.76	1.44	6.30
QHH35HA							72	105.8	139.4	20.9															95.23	115.55	1.45	1.33	1.33	1.90	
QHH45CA	70	9.2	20.5	86	60	13	60	97	139.4	23	10	12.9	M10x17	16	18.5	20	45	38	20	17	14	105	22.5	M12×35	119.4	135.42	1.83	1.38	1.38	2.72	10.41
QHH45HA							80	128.8	171.2	29.09															144.13	180.56	2.47	2.41	2.41	3.59	

Note : 1 kgf = 9.81 N

Figure C.2: Datasheet of linear guide from a catalog of Hiwin, showing different sizes of guides with their corresponding characteristics.

Appendix D

Actuator selection

Part of designing a robot involves the selection of actuators. The choice for a specific type of actuator depends on the application and the desired properties. Naturally, a rotary concept requires rotary actuators, and a Cartesian concept requires linear actuators. Both types of actuators offer a range of different, but also similar configurations. For the sake of simplicity and based on controllability, only electric actuators are considered.

D.1 Iron-core motor

Even for linear motors, there exist numerous options. Since Prodrive Technologies is willing to provide linear motors for this test-setup, the motors used are iron core linear motors. These are permanent-magnet based motors that, by supplying power to copper spools with an iron core, provide a Lorentz force proportional to the supplied current. An illustration of this motor is depicted in Figure D.1:

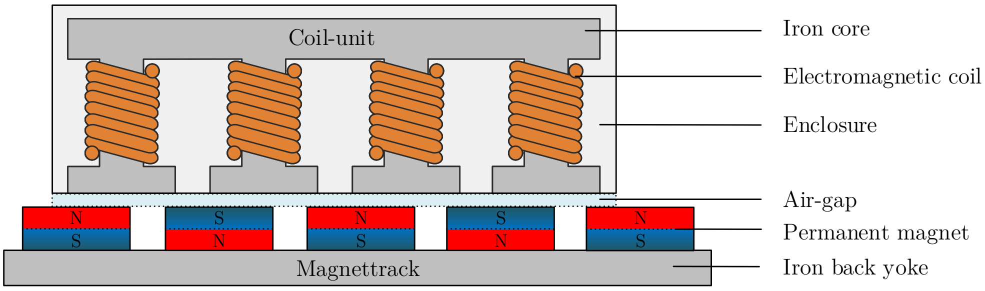

Figure D.1: Illustration of iron-core linear motor from a catalog of Tecnotion, showing different motor configuration for smallest available width of magnet-track.

D.2 Characteristics of iron-core linear motors

A linear motor exerts a force proportional to the amount of current running through the spools. This proportion is based on a Lorentz force, $F = I \times B$. Here F is the force applied by the motor, I stands for the current supplied to the motor, and B concerns the magnetic field generated by the permanent magnets.

Most manufacturers list a continuous and a maximum or ultimate force that the motor can supply. The motor can generate the continuous force for extended periods, provided the mounting structure of the robot can dissipate the generated heat. Up to this range, the relation between current and force is roughly linear as the effects of magnetic saturation of the ferromagnetic materials are limited, [42]. Generating higher forces up to the maximum force starts to cause saturation effects distorting this linear relation.

An important factor in performance or efficiency for linear iron-core motors is the air-gap between the coil-unit and the magnet track [43]. The performance of the motor is best when this air-gap is kept as low as possible in the order of a tenth of a millimeter. This poses a challenge in designing a robot that incorporates this type of motor, a minimum air-gap in combination with impacts. For this reason, it might be an option to sacrifice efficiency for an increase in air-gap and tolerance. Note that, in principle, this minimum air-gap requirement would also hold for rotary motors.

D.3 Selection criteria

The actuator is selected based on the weight of the arm and the required accelerations. Since the required force is directly proportional to the displaced mass and required acceleration, selecting the right actuator should not be a problem. Every Newton the actuator can deliver is paid by an increase in weight and an increased tole on the bearings. For this reason, the actuator is chosen according to what is minimally required.

As already stated, the specifications of a linear motor offer a maximum and a continuous motor force. The maximum required accelerations by the robot define the maximum motor force. In most other cases, the continuous force is sufficient.

D.4 Data-sheet selection

A number of different options is shown in Figure D.2. For the x-stage, the TM6 is chosen, providing an ultimate force of 240 N, and for the y-stage, the TM3 is chosen, providing an ultimate force of 120 N. Note that during the creation of a detailed design of the setup, this should be reevaluated.

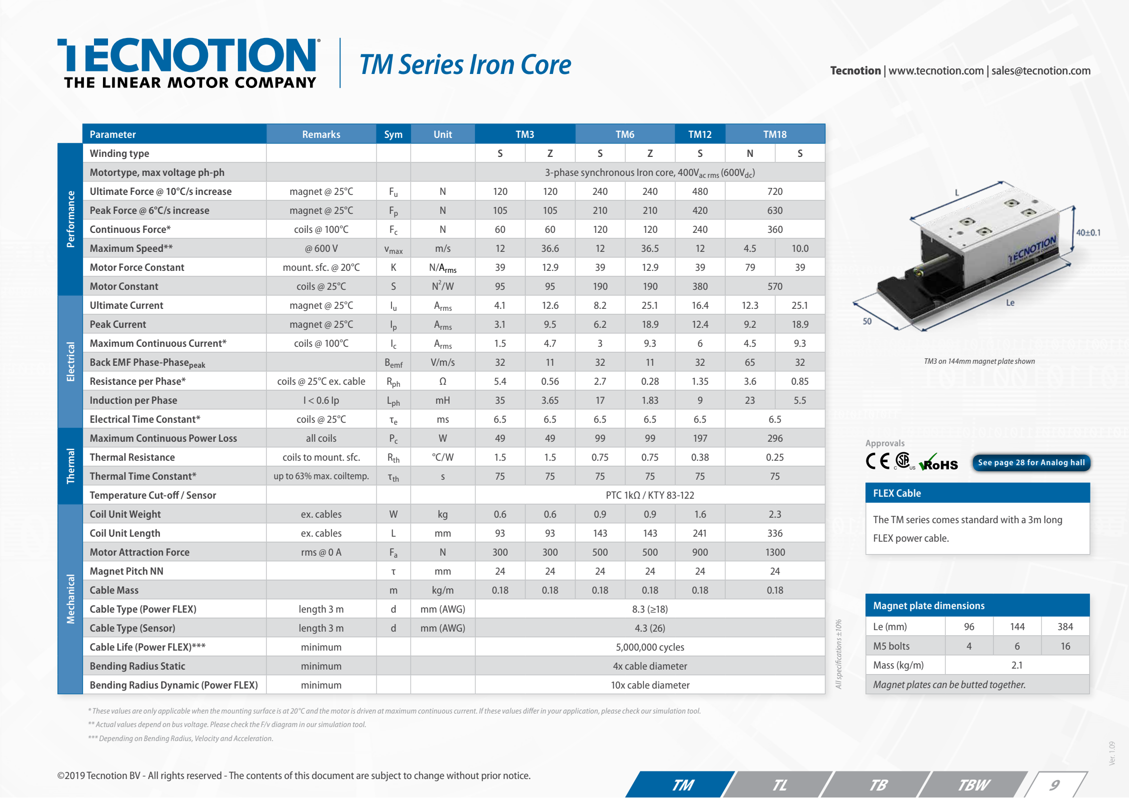

TM Series Iron Core

Tecnotion | www.tecnotion.com | sales@tecnotion.com

	Parameter	Remarks	Sym	Unit	TM3		TM6		TM12	TM18	
Performance	**Winding type**				S	Z	S	Z	S	N	S
	Motortype, max voltage ph-ph				3-phase synchronous Iron core, 400$V_{ac\ rms}$ (600V_{dc})						
	Ultimate Force @ 10°C/s increase	magnet @ 25°C	F_u	N	120	120	240	240	480	720	
	Peak Force @ 6°C/s increase	magnet @ 25°C	F_p	N	105	105	210	210	420	630	
	Continuous Force*	coils @ 100°C	F_c	N	60	60	120	120	240	360	
	Maximum Speed**	@ 600 V	v_{max}	m/s	12	36.6	12	36.5	12	4.5	10.0
	Motor Force Constant	mount. sfc. @ 20°C	K	N/A_{rms}	39	12.9	39	12.9	39	79	39
	Motor Constant	coils @ 25°C	S	N^2/W	95	95	190	190	380	570	
Electrical	**Ultimate Current**	magnet @ 25°C	I_u	A_{rms}	4.1	12.6	8.2	25.1	16.4	12.3	25.1
	Peak Current	magnet @ 25°C	I_p	A_{rms}	3.1	9.5	6.2	18.9	12.4	9.2	18.9
	Maximum Continuous Current*	coils @ 100°C	I_c	A_{rms}	1.5	4.7	3	9.3	6	4.5	9.3
	Back EMF Phase-Phase$_{peak}$		B_{emf}	V/m/s	32	11	32	11	32	65	32
	Resistance per Phase*	coils @ 25°C ex. cable	R_{ph}	Ω	5.4	0.56	2.7	0.28	1.35	3.6	0.85
	Induction per Phase	I < 0.6 Ip	L_{ph}	mH	35	3.65	17	1.83	9	23	5.5
	Electrical Time Constant*	coils @ 25°C	τ_e	ms	6.5	6.5	6.5	6.5	6.5	6.5	
Thermal	**Maximum Continuous Power Loss**	all coils	P_c	W	49	49	99	99	197	296	
	Thermal Resistance	coils to mount. sfc.	R_{th}	°C/W	1.5	1.5	0.75	0.75	0.38	0.25	
	Thermal Time Constant*	up to 63% max. coiltemp.	τ_{th}	s	75	75	75	75	75	75	
	Temperature Cut-off / Sensor				PTC 1kΩ / KTY 83-122						
Mechanical	**Coil Unit Weight**	ex. cables	W	kg	0.6	0.6	0.9	0.9	1.6	2.3	
	Coil Unit Length	ex. cables	L	mm	93	93	143	143	241	336	
	Motor Attraction Force	rms @ 0 A	F_a	N	300	300	500	500	900	1300	
	Magnet Pitch NN		τ	mm	24	24	24	24	24	24	
	Cable Mass		m	kg/m	0.18	0.18	0.18	0.18	0.18	0.18	
	Cable Type (Power FLEX)	length 3 m	d	mm (AWG)	8.3 (≥18)						
	Cable Type (Sensor)	length 3 m	d	mm (AWG)	4.3 (26)						
	Cable Life (Power FLEX)***	minimum			5,000,000 cycles						
	Bending Radius Static	minimum			4x cable diameter						
	Bending Radius Dynamic (Power FLEX)	minimum			10x cable diameter						

All specifications ±10%

* These values are only applicable when the mounting surface is at 20°C and the motor is driven at maximum continuous current. If these values differ in your application, please check our simulation tool.

** Actual values depend on bus voltage. Please check the F/v diagram in our simulation tool.

*** Depending on Bending Radius, Velocity and Acceleration.

TM3 on 144mm magnet plate shown

Approvals

FLEX Cable

The TM series comes standard with a 3m long FLEX power cable.

Magnet plate dimensions			
Le (mm)	96	144	384
M5 bolts	4	6	16
Mass (kg/m)	2.1		
Magnet plates can be butted together.			

Ver. 1.09

Figure D.2: Datasheet for iron-core motor as

Appendix E

Finite Element Method model analysis

E.1 FEM analysis of end-effector

With the use of a Finite Element Method (FEM) model, the end-effector is analyzed to confirm the stiffness. The routine used to analyze the end-effector is shown in Figure E.1.

Constraints. The end-effector is constrained at four positions, which coincide with the mounting holes of the end-effector to the robot arms. The constrained points are shown in blue in Figure E.1. These points are fully constrained, locking all degrees of freedom.

Load. The mounting holes of the tip to the bracket are subjected to different displacements, ranging from 1 to 10mm.

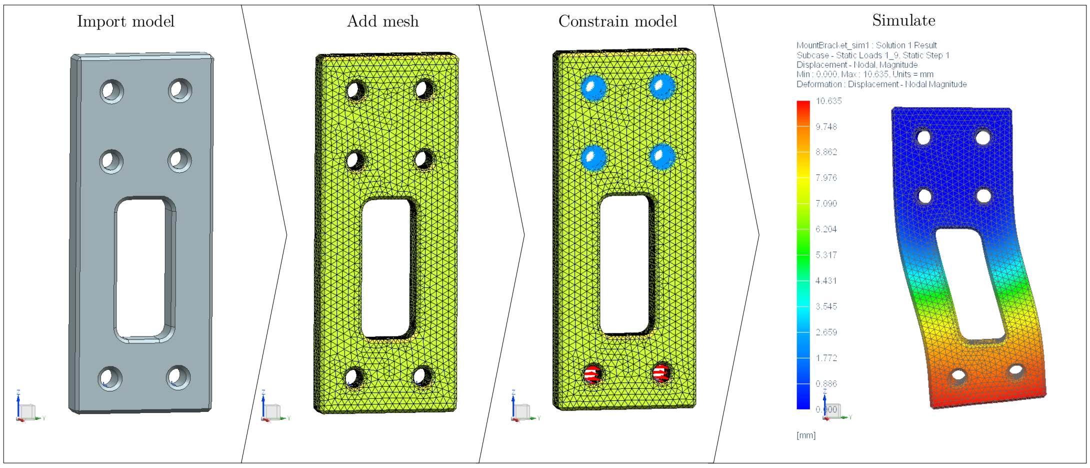

Figure E.1: Routine used to analyze end-effector using FEM model in the software package Siemens NX with NX Nastran solver.

Results. The analysis shows that a displacement of 1 mm causes a reaction force of 0.7 kN, a displacement of 10 mm causes a reaction force of 7.0 kN. This shows that the end-effector has an estimated stiffness of 0.7 N/mm, and that this is the case over the relevant range of deformation. This is a stiffness which is 0.2 N/mm higher than the required stiffness. Meaning it is too stiff. However, in combination with a rubber tip, this is acceptable.

Appendix F

Rigid multi-body simulations in Algoryx Momentum

This appendix describes routines which are not discussed in the main text. The appendix starts with a section on model setup, and is followed by a discussion on different routines and implementations.

F.1 Model setup

In this section the workflow to generate the multi-body model is discussed.

F.1.1 Creating model structure

Once the CAD files are imported into Discovery, the parts are grouped based on their position and role in the model.

F.1.2 Assigning constraints

To start, the model is imported into ANSYS Discovery Spaceclaim, brief Spaceclaim. Inside the Algoryx Momentum environment of Spaceclaim, all components are grouped together based on the type of body. A component or assembly is either non-moving and fixed to earth or is moving and fixed to another body by means of a joint-constraint. Since this is a Cartesian design, only prismatic joints are used. The model in combination with the constraints is shown in Figure F.1. Note that component-groups that are directly linked through constraints are not able to collide. Any intersection between these bodies is not prevented by means of a reaction force.

F.1.2.1 Assigning material-properties

Either before or after including the constraints in this model, physical properties must be added to the simulation. Two kind of material properties are available for adjustment. Individual properties and combined material properties in the form of material pairs. In terms of individual material properties, all parts are linked to a density of a material. This allows for a simulation

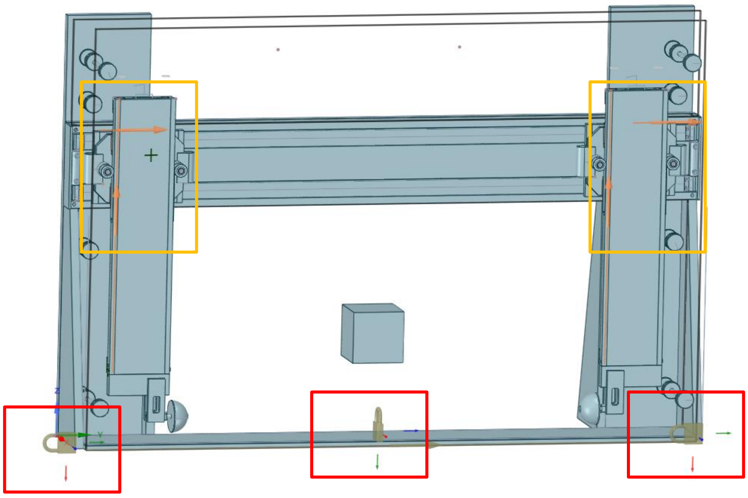

Figure F.1: Image of the model in Algoryx Momentum showing constraints applied to the structure and the rigid-bodies.

with inertial properties based on physical attributes of materials.

In terms of material pairs, the following options can be entered:

- Restitution coefficient
- Friction coefficient
- Young's modulus
- Elastic domain

The influence of these different settings is discussed per parameter:

Restitution coefficient The coefficient of restitution represents a fractional relation between the velocity of a moving body before, and after impact. The default coefficient of restitution is 0.2. This setting was kept constant during the simulations.

Friction coefficient The friction coefficient determines the friction applied based on a normal force. The standard value for this parameter is 0.15. This property is changed based on the used materials. The properties used for this setting will be taken from [11].

Young's modulus The Young's modulus determines reaction force between two materials when interacting.

Elastic domain Setting the elastic domain might limit the elastic domain calculated by the software.

Once all parameters are set, actuators and joints are added to the model. Actuators are added to the model and limitations on force capabilities of the actuators is set.

F.2 Python implementation

Now all parameters are set, the model is controlled using routines implemented in python. The implemented routines are explained with the use of pseudo code.

The following routine is used to detect impact during simulations. The routine makes use of the function Numpy, [44]. The routine is used for identification of impacts based on state information of the arms of the robot. The routine is used in all routines that require the identification of contact through impacts.

Algorithm 1 Impact detection

```
procedure IMPACT DETECTION
    $x_{new} \leftarrow$ new value of state
    $x_{new} \leftarrow$ new value of time
    $n_{deg} \leftarrow$ degree of polynomial
    $n_{buf} \leftarrow$ length of polynomial training-set
    $B \leftarrow$ max deviation from prediction
    $i \leftarrow 0$
    $\text{buffer}_x[n_{buf}] \leftarrow 0$
    $\text{buffer}_t[n_{buf}] \leftarrow 0$
start:
    $\text{buffer}_x[i] \leftarrow x_{new}$
    $\text{buffer}_t[i] \leftarrow t_{new}$
    $i \leftarrow i + 1$
    if $i = n_{deg}$ then
        $i \leftarrow 0$
        goto main
    else
        goto start
main:
    $\text{buffer}_x[i] \leftarrow x_{new}$
    $\text{buffer}_t[i] \leftarrow t_{new}$
    $i \leftarrow i + 1$
    if $i = n_{deg}$ then
        $i \leftarrow 0$
    $A = \text{np.polyfit}(\text{buffer}_t[n_{buf}], \text{buffer}_x[n_{buf}], n_{deg})$
    $P = \text{np.poly1D}(A)$
    if $x_{new} > P(t_{new})(1 + B)$ or $x_{new} < P(t_{new})(1 - B)$ then return impact true
    else return impact false
    goto main.
```

F.3 Catching of objects

An object is caught by correctly timing the moment on which the object passes the end-effector to intercept the object. Figure F.2 is used to explain how this timing is achieved.

The position of the end-effector is denoted by p_{ee}. The position of the center of the object is denoted by p_{obj}. As the object is falling, the projected position is described by:

$$p'_{obj} = p_{obj} - v_{obj}t_f - \frac{1}{2}gt_f^2, \tag{F.1}$$

where p_{obj} and v_{obj} are taken as the current position and velocity, projecting the position p'_{obj} after time t_f. The projected position of the end-effector is described by:

$$p'_{ee} = p_{ee} + \frac{1}{2}a_{ee}t_a^2, \tag{F.2}$$

where p'_{ee} is the projected position after time t_a, with initial position p_{ee} and acceleration a_{ee}.

Once the projected position of the object is at a position where:

$$p'_{obj,y} \leq \frac{p'_{ee,y1} + p'_{ee,y2}}{2} \text{ for } t_a = t_f, \tag{F.3}$$

both end-effectors accelerate toward the object with acceleration $a_{x,max}$. Here, t_f is computed based on $p_{ee,y} = p'_{obj,y}$. In the case that accelerating at $a_{x,max}$ for a time of t_a results in a velocity higher than the max velocity of $v_{x,max}$, and in case the end-effector is already moving, the projected position of the end-effector becomes:

$$p'_{ee,x} = p_{ee,x} + v_{ee,x}t_a + v_{x,max}t_c + \frac{1}{2}a_{ee}t_a^2, \tag{F.4}$$

where t_c is the projected time moving at $v_{x,max}$. In this case, t_f in Equation F.3 becomes $t_f + t_c$.

In the case that one end-effector is closer to the object than the other, the velocity towards the object is corrected by means of an additional velocity component as shown in Equation F.5:

$$v_{x,corr} = \frac{(p_{obj,x} - p_{ee1,x}) - (p_{ee2,x} - p_{obj,x})}{2}, \tag{F.5}$$

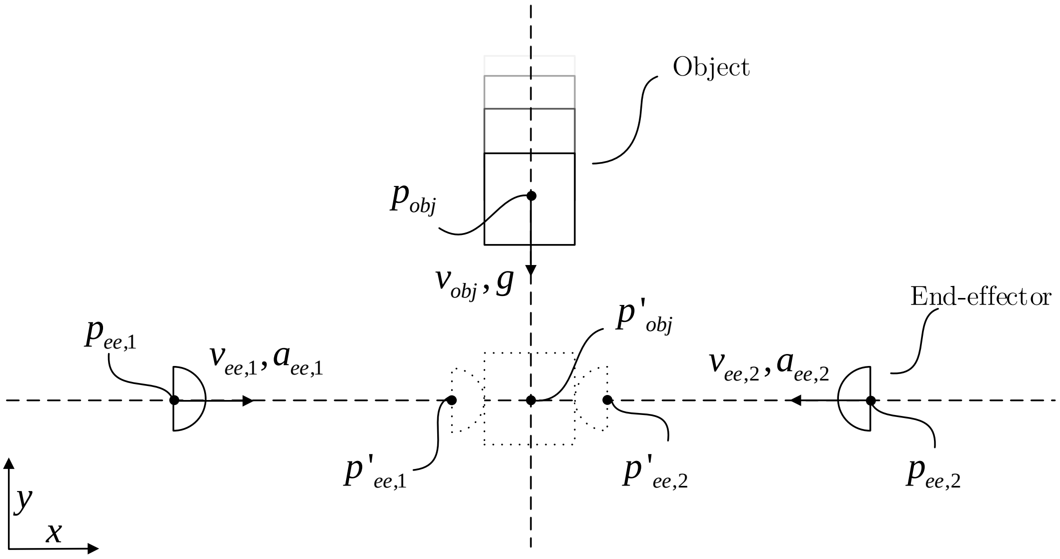

Figure F.2: Illustration of a falling object, with the current and projected position of both end-effectors and the object, used to catch a falling object.

which is added to the reference velocity of both arms.

Bibliography

[1] Wolfgang Echelmeyer, Alice Kirchheim, and Eckhard Wellbrock. Robotics-logistics: Challenges for automation of logistic processes. *Proceedings of the IEEE International Conference on Automation and Logistics, ICAL 2008*, (September):2099–2103, 2008. 2

[2] Bhanoday Reddy Vemula. *Evaluation of Robot Structures For Applications That Require High Performance, Safety And Low Energy Consumption*. Number 223. 2015. 2

[3] John T. Feddema. Kinematically optimal robot placement for minimum time coordinated motion. *Proceedings - IEEE International Conference on Robotics and Automation*, 4(April):3395–3400, 1996. 2

[4] Antonio Tornambè. Modeling and control of impact in mechanical systems: Theory and experimental results. *IEEE Transactions on Automatic Control*, 44(2):294–309, 1999. 2

[5] Koichi Nishiwaki, Atsushi Konno, Koichi Nagashima, Masayuki Inaba, and Hirochika Inoue. Humanoid Saika that catches a thrown ball. *Robot and Human Communication - Proceedings of the IEEE International Workshop*, pages 94–99, 1997. 2

[6] Berthold Bäuml, Thomas Wimböck, and Gerd Hirzinger. Kinematically optimal catching a flying ball with a hand-arm-system. *IEEE/RSJ 2010 International Conference on Intelligent Robots and Systems, IROS 2010 - Conference Proceedings*, (November 2010):2592–2599, 2010. 2

[7] Alessandro Saccon, Nathan Van De Wouw, and Henk Nijmeijer. Sensitivity analysis of hybrid systems with state jumps with application to trajectory tracking. *Proceedings of the IEEE Conference on Decision and Control*, 2015-Febru(February):3065–3070, 2014. 2, 39

[8] Mark Rijnen, Alessandro Saccon, and Henk Nijmeijer. On optimal trajectory tracking for mechanical systems with unilateral constraints. *Proceedings of the IEEE Conference on Decision and Control*, 54rd IEEE(Cdc):2561–2566, 2015. 2, 39

[9] Mark Rijnen, Alessandro Saccon, and Henk Nijmeijer. Reference Spreading: Tracking Performance for Impact Trajectories of a 1DoF Setup. *IEEE Transactions on Control Systems Technology*, 28(3):1124–1131, 2020. 3

[10] Bonkovic M. Grujic, T. Measurement and Analysis of Human Hand Kinematics. *Scandinavian Journal of Haematology*, 6(S6):8–13, 2009. 5, 9

[11] William D. Callister and David G. Rethwisch. *Materials science and engineering: An introduction*, volume 14. Wiley, 10th edition, 2018. 5, 78

[12] Christian Smith, Yiannis Karayiannidis, Lazaros Nalpantidis, Xavi Gratal, Peng Qi, Dimos V Dimarogonas, and Danica Kragic. Dual arm manipulation—A survey. *Robotics and Autonomous Systems*, 60:1340–1353, 2012. 13

[13] Nima Fazeli, Samuel Zapolsky, Evan Drumwright, and Alberto Rodriguez. Fundamental Limitations in Performance and Interpretability of Common Planar Rigid-Body Contact Models. pages 1–16, 2017. 14, 44

[14] Jianlin Zheng and Wei Yang. Failure Analysis of a Flexspline of Harmonic Gear Drive in STC Industrial Robot: Microstructure and Stress Distribution. *IOP Conference Series: Materials Science and Engineering*, 452(4), 2018. 14

[15] Tecnotion. Torque motor manual, 2018. 15, 17, 59

[16] Tecnotion. Iron-Core & Ironless Linear Motor Series, 2019. 15, 44, 57

[17] Houman Dallali, Petar Kormushev, Nikos G. Tsagarakis, and Darwin G. Caldwell. Can active impedance protect robots from landing impact? *IEEE-RAS International Conference on Humanoid Robots*, 2015-Febru:1022–1027, 2015. 24

[18] Jie Chen, Zhongchao Liang, Yanhe Zhu, Chong Liu, Lei Zhang, Lina Hao, and Jie Zhao. Towards the Exploitation of Physical Compliance in Segmented and Electrically Actuated Robotic Legs: A Review Focused on Elastic Mechanisms. *Sensors (Basel, Switzerland)*, 19(24), 2019. 24

[19] Wooseok Choi, Chengxu Zhou, Gustavo A. Medrano-Cerda, Darwin G. Caldwell, and Nikos G. Tsagarakis. A new foot sole design for humanoids robots based on viscous air damping mechanism. *IEEE International Conference on Intelligent Robots and Systems*, 2015-Decem(June 2016):4498–4503, 2015. 24

[20] Wooseok Choi, Gustavo A. Medrano-Cerda, Darwin G. Caldwell, and Nikos G. Tsagarakis. Design of a variable compliant humanoid foot with a new toe mechanism. *Proceedings - IEEE International Conference on Robotics and Automation*, 2016-June:642–647, 2016. 24

[21] Huaxin Liu, Qiang Huang, Weimin Zhang, Xuechao Chen, Zhangguo Yu, Libo Meng, Lei Bao, Aiguo Ming, Yan Huang, Kenji Hashimoto, and Atsuo Takanishi. Cat-inspired mechanical design of self-adaptive toes for a legged robot. *IEEE International Conference on Intelligent Robots and Systems*, 2016-Novem:2425–2430, 2016. 24

[22] Simon Hauser, Peter Eckert, Alexandre Tuleu, and Auke Ijspeert. Friction and damping of a compliant foot based on granular jamming for legged robots. *Proceedings of the IEEE RAS and EMBS International Conference on Biomedical Robotics and Biomechatronics*, 2016-July:1160–1165, 2016. 24

[23] Simon Hauser, Matthew Robertson, Auke Ijspeert, and Jamie Paik. JammJoint: A Variable Stiffness Device Based on Granular Jamming for Wearable Joint Support. *IEEE Robotics and Automation Letters*, 2(2):849–855, 2017. 24

[24] Kazuo Hirai, Masato Hirose, Yuji Haikawa, and Toru Takenaka. Hirai 1998 Development of a honda humanoid robot.pdf. pages 1321–1326, 1998. 24

[25] Robert MacCurdy, Jeffrey Lipton, Shuguang Li, and Daniela Rus. Printable programmable viscoelastic materials for robots. *IEEE International Conference on Intelligent Robots and Systems*, 2016-Novem:2628–2635, 2016. 24

[26] Rong Wang, Jianzhong Shang, Xin Li, Zirong Luo, and Wei Wu. Vibration and damping characteristics of 3D printed Kagome lattice with viscoelastic material filling. *Scientific Reports*, 8(1):1–13, 2018. 24

[27] Ethan Schumann, Nils Smit-Anseeuw, Petr Zaytsev, Rodney Gleason, K. Alex Shorter, and C. David Remy. Effects of foot stiffness and damping on walking robot performance. *Proceedings - IEEE International Conference on Robotics and Automation*, 2019-May:3698–3704, 2019. 24, 34

[28] R.H.O. Frictional properties of rubber. *Journal of the Franklin Institute*, 233(5):486–487, 1942. 24

[29] Ion Boldea and Syed A. Nasar. Linear electric actuators and generators. *IEEE Transactions on Energy Conversion*, 14(3):712–717, 1999. 26

[30] F.C. Campbell. *Manufacturing processes for Advanced Composites*. Elsevier, 2004. 29

[31] A. A. D. Brown. *Mechanical Springs*. Oxford University Press, 1981. 30

[32] Vulcan Springs. Design Guide for constant force springs. 30

[33] Warren Clarence Young and Richard Gordon Budynas. *Roark's formulas for stress and strain*, volume 7. 2002. 33, 35

[34] John Ryan C. Dizon, Alejandro H. Espera, Qiyi Chen, and Rigoberto C. Advincula. Mechanical characterization of 3D-printed polymers. *Additive Manufacturing*, 20(January 2018):44–67, 2018. 33

[35] Rudulf Kingslake and R. Barry Johnson. *Lens Design Fundamentals*. Elsevier, second edition, 2010. 34

[36] Steve Lampman. *Characterization and Failure analysis of tools of plastics*, volume 162. ASM International, 2004. 34

[37] Algoryx Simulation AB, Algoryx Momentum, 2020. 38

[38] Bernard Brogliato. *Nonsmooth Impact Mechanics*. Springer, 1996. 40

[39] Claude Lacoursiere. *Ghosts and machines: regularized variational methods for interactive simulations of multibodies with dry frictional contacts*. 2007. 40

[40] Hiwin Technologies Corp. Linear Guideway, 2018. 57, 66, 67, 68

[41] Bosh Rexroth. *Linear Motion Technology Handbook*. 2017. 66

[42] Slawomir Tumanski. *Handbook of magnetic measurements*. Number May. 2016. 73

[43] M Donat. Investigation of the influence of air gap thickness and eccentricity on the noise of the rotating electrical machine. 7:123–136, 2013. 73

[44] Oliphant Travis. Numpy user manual. Technical report, 2007. 79

Technische Universiteit
Eindhoven
University of Technology

Declaration concerning the TU/e Code of Scientific Conduct for the Master's/PDEng/PhD thesis

I have read the TU/e Code of Scientific Conduct[i].

I hereby declare that my Master's /PDEng/PhD-thesis has been carried out in accordance with the rules of the TU/e Code of Scientific Conduct

Date

5 - 05 - 2020

Name

R.H.G.W de Wildt

Signature

---

[i] See: http://www.tue.nl/en/university/about-the-university/integrity/scientific-integrity/
The Netherlands Code of Conduct for Academic Practice of the VSNU can be found here also.
More information about scientific integrity is published on the websites of TU/e and VSNU